UNIVERSIDADE DE SANTIAGO
DE COMPOSTELA

Área de Óptica, Departamento de Física Aplicada, Facultade de Física

Unidad Asociada de Óptica y Microóptica GRIN al
Instituto de Ciencia de Materiales de Aragón, Zaragoza (ICMA-CSIC)

Planar waveguides obtained on commercial glass substrates by sol-gel and laser irradiation methods

Francisco Rey García
Santiago, Outubro 2011

Dona María Teresa Flores Arias, Profesora Titular de Universidade da Area de Óptica da Facultade de Física e da Unidade Asociada de Óptica e Microóptica GRIN do Departamento de Física Aplicada da Universidade de Santiago de Compostela e Don Xermán Francisco De La Fuente Leis, Profesor de Investigación do Instituto de Ciencia de Materiales de Aragón (ICMA-CSIC).

INFORMAN

que a presente memoria, titulada "Planar waveguides obtained on commercial glass substrates by sol-gel and laser irradiation methods" foi realizada por **D. Francisco Rey García** baixo a súa dirección e constitúe a Tese que amosa para optar ó Grado de Doutor en Fotónica e Tecnoloxías do Láser.

Santiago de Compostela, de Outubro de 2011

Vº. Bº. Directora da tese

María Teresa Flores Arias

Vº. Bº. Director da tese

Xermán F. De La Fuente Leis

O doctorando

Francisco Rey García

This work has been funded by the Ministerio de Ciencia e Innovación (MICINN) under the projects TEC2006-10469, CEN 2007-2014, SURFALUX SOL-00030930 and MAT2010-18519; by DGA (Group of Excellence in Laser Materials Processing and Characterization); by Gobierno de Aragón/FEDER (Group T87, Laboratorio de Aplicaciones del Láser) and by Xunta de Galicia/FEDER through the project INCITE08PXIB206013PR. The author acknowledges the Ministerio de Ciencia e Innovación for the FPI fellowship.

Summary

The aim of this thesis is the fabrication and characterization of photonic structures for potential applications in fields related to spatial optics, particulary, as planar waveguides. The motivation for the work proposed was to study poorly explored methods and inexpensive substrates that allow fabrication of waveguides in a scalable fashion. These devices are of great interest for a large number of applications in communications, integrated optics and in other fields of technology. During the past few years, many authors have explored diverse fabrication methods in order to obtain photonic structures, although, in many instances, they have developed products which would either be expensive (special, non commercial glasses), or used expensive experimental set-ups (which would make an industrial scale-up inviable). The methods and substrates saught after in this thesis include high repeatability, high precision control and inexpensive materials.

A planar waveguide allows light guiding through its volume without significant changes on its properties, thus opening the door to many high technology applications which include the communications, sensors, lasers and optics industrial sectors, among many others. Moreover, a number of new devices may be developed based on optical interconnects to implement distribution systems in parallel or cross-optical signals. The possibility of fabricating planar waveguides using inexpensive and simple technology opens a very interesting field of science.

Three different techniques are studied in this work for the fabrication of planar optical waveguides. Sol-Gel method, Laser Zone Melting and Laser Ablation Backwriting of Metal Targets are developed and the corresponding samples obtained are characterized through different methods. Each method

supposes the obtantion of sample with determined characteristics; for this motive a wide range of characterization techniques are used, depending of the specimen studied. The characterization of the laser ablation method consisted basically in the study of the processes involved in the formation of the waveguides. The methods used are described in Chapters 1 and 2; the results obtained are presented in the Chapter 3.

The chemical and microstructural studies are carryingout by Transmission Electron Microscopy (TEM), Scanning Electron Microscopy (SEM), Confocal Microscopy, UV/Vis Spectroscopy, X-Ray Diffraction and IR/Raman Spectroscopy. The optical characterization of samples was developed; employing different techniques to measure refractive index, thickness and losses. Moreover, the electrical conductivity of the metalic samples obtained through the laser ablation is measured. All this techniques are described in the Chapter 2.

The Sol-Gel method is based in the obtention of thin films (since 135 nm to $2,15\ \mu m$, measured by Ellipsometry) from a solution of metal alkoxide precursors, coating commercial glass substrates by the dip-coating technique. This technique allows the best control of the composition, thickness and refractive index. Different systems based in mixtures of SiO_2, TiO_2, ZrO_2 and CeO_2 are tested obtaining a range of indices between 1.45 and 2.04 (values obtained by Ellipsometry). This kinds of samples present moderate guiding losses; obtaining values between 0.85 and 1.5 dB/cm for the attenuation coefficient.

The Laser Zone Melting technology is applied to sintering a mixture of glassy powders onto commercial glass substrates, obtaining a guiding layer with thickness ca. 10 μm as minimum. The sintering process is developed employing a CO_2 laser provided with a oven roller train. The coatings obtained are based in lead borosilicates mixtures; and provide, the basic composition, a refractive index ca. 1.58 (Refracted Near-Field Technique, λ=633 nm). The losses measured result higher than the obtained by the Sol-Gel technique, resulting in a value of losses of 3.04 dB/cm for a ytterbium-doped lead borosilicate sample.

The study of the Laser Ablation Backwriting of Metal Targets technique supposes a continuation of the work developed by other researchers of the group. The aim of the present thesis is to study the processes involved in the formation of metalic channel waveguides onto commercial glass substrates via Laser Backwriting. Samples of aluminum, silver and brass are obtained and

characterized. The results achieved suppose the consideration of this kind of photonic materials as diffusive elements when we talk about the guiding of the light.

The final step of this work supposes the comparison of the results and the presentation of the conclusions (Chapter 4). The main conclusion is the possibility to obtain planar optical waveguides by cheaper and easier alternatives to the typical methods presented in the literature, those, generally require vacuum conditions and special reactives and instruments. Moreover it was succesfully checked the possibility to obtain guding elements onto commercial glass substrates. These efforts suppose an advantage for the industrial scaling of these processes.

CONTENTS

Chapter 1

INTRODUCTION

The aim of this thesis is the fabrication and characterization of photonic structures for potential applications in fields related to spatial optics, particulary, as planar waveguides. The motivation for the work proposed was to study poorly explored methods and inexpensive substrates that allow fabrication of waveguides in a scalable fashion. These devices are of great interest for a large number of applications in communications, integrated optics and in other fields of technology. During the past few years, many authors have explored diverse fabrication methods in order to obtain photonic structures, although, in many instances, they have developed products which would either be expensive (special, non commercial glasses), or used expensive experimental setups (which would make an industrial scale-up inviable). The methods and substrates saught after in this thesis include high repeatability, high precision control and inexpensive materials.

A planar waveguide allows light guiding through its volume without significant changes on its properties, thus opening the door to many high technology applications which include the communications, sensors, lasers and optics industrial sectors, among many others. Moreover, a number of new devices may be developed based on optical interconnects to implement distribution systems in parallel or cross-optical signals [1-5]. Thus, using on-axis and off-axis image formation, it is possible to interconnect, steadily and with great precision, elements of bidimensional arrays integrated over the surface of a gradient index (GRIN) substrate that acts as a guiding structure [5-7]. Therefore, the possibility of fabricating planar waveguides using inexpensive and simple technology opens a very interesting field of science and may help induce realisation of its potential for a wide range of applications.

1.1 Homogeneous planar structures

A planar waveguide is formed by a set of surfaces that separate transparent dielectric media of different refractive index; we can consider this structure like a rectangular optical fiber. For the effective confinement of the light, the guiding medium will be surrounded by one or two materials whit a lower refractive

index value. For a homogeneous (step-index) waveguide, the guiding medium has a constant refractive index, and the guiding of light results from its multiple total internal reflections at the separation zone surfaces. This guiding medium is known as the "core". The guiding can be visualized describing zig-zag ray paths. Thus, the waveguide is a structure that confines and transports light. The confinement is performed in the transverse direction and spreads in the longitudinal direction. Figure 1.1 shows the geometry of a planar waveguide. The guiding medium (n_1) is located between a cover or coating of refractive index n_2, and a substrate, with refractive index n_3 (Fig. 1.1) [8].

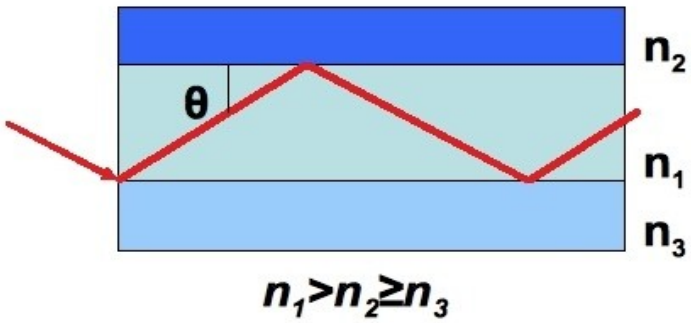

Figure 1.1: Planar waveguide structure and relation between the different refractive indices. The core (n_1) has a higher refractive index than the cover (n_2) and the substrate (n_3).

In this thesis, we present three different technologies for the fabrication of asymmetric planar waveguides, consisting of a glass substrate covered by a planar layer deposit. Air plays the role of the third layer [8-10] (Fig. 1.2).

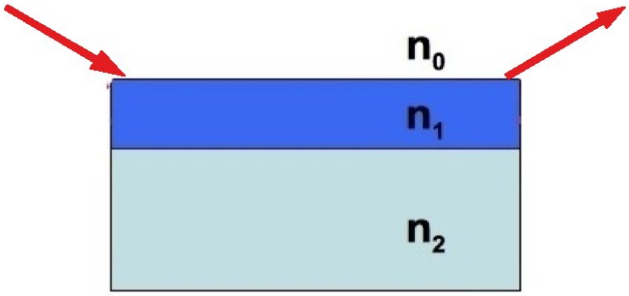

Figure 1.2: Displacement direction of the beam into a planar waveguide. The core (n_1) has a higher refractive index than the substrate (n_2) and air (n_0), which acts like a cover.

1.2 Background

The coating of materials to improve or modify previous properties entails a wide field of study, developed for the last several decades. In particular, the preparation of planar waveguiding elements has provoked great interest in research due to its potential applications in photonics. Traditionally, these types of devices were fabricated using methods such as ion-exchange [11], chemical vapour deposition (CVD) [12-14] and physical vapour deposition (PVD) [15]. Methods for the fabrication of integrated optical devices based on ion implantation [16-17], lithography or photolithography [18-20], direct laser writing [21-25], or even ultra-fast laser pulse irradiation [26-27], have however, been developed more recently. These involve the use of complex equipment (vacuum systems or expensive lasers are needed) or synthesis conditions and source materials which result in a high processing cost. All these techniques are used to obtain planar waveguiding elements on glass substrates of different composition. The main principle of all these techniques is the control of the local change of the refractive index of a transparent sustrate [28-30]. In all above-mentioned work the substrate is doped; the resultant index change generated within the substrate as a consequence of doping enables light guiding through it.

The inherent complexity associated to the above preparative methods, led us to search for more economical and simple fabrication alternatives. Physically and chemically compatible coatings have thus been developed to accordingly modify soda-lime commercial glass substrates. Following these principles, the methods or technologies described below have been selected for the present work.

1.2.1 Sol-Gel method

An alternative method to obtain planar waveguides is based on Sol-Gel technology and permits to obtain coatings with controlled thickness and refractive index. This technology has been widely applied in different fields of materials science, from purely inorganic materials to organic and biological systems allowing the development of biosensors [31], bulk insulators [32],

superconductors [33], fuel cells [34], ceramic composites [35], and other materials, under a wide range of compositions. Planar waveguides fabricated with this method have been the subject of a good number of studies reported in the literature [36-44]. Sol-Gel is suitable to produce both, thin and thick films, by making use of either single or multideposition processes; thus the functionality and applicability of the Sol-Gel method was explored and developed (Fig. 1.3); assisted by an inmersion technique, to obtain planar waveguiding structures [45-46].

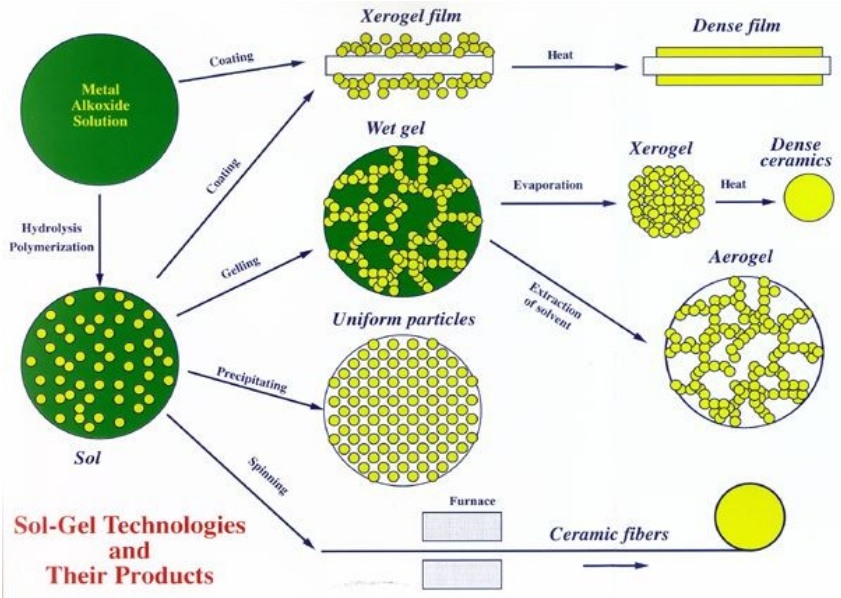

Figure 1.3: Scheme of Sol-gel technology and the posible products obtained through the different synthesis conditions employed.

With the Sol-Gel technique we can obtain coatings with higher refractive indices that those obtained by the traditional substrate surface modification techniques (such as ion-exchange, for example). The microstructure of Sol-Gel derived coatings, thus, their optical properties, is affected by different parameters involved in their synthesis. These include starting materials, solvent, and thermal processing conditions, among others [47-49]. The optimization and control of all these parameters should allow the production of efficient Sol-Gel derived planar waveguides. This technique allows a greater control of chemical

composition and, therefore, the possibility to prepare coating structures with very different refractive indices [50]. Moreover, this method allows the development of complex planar coatings, i.e. the development of multilayer systems. As an additional advantage, related to industrial processes and environmental factors, the energy cost of the process is significantly lower than the traditional methods, since it allows working at relatively low temperatures approaching 450 ºC, or even as low as 150 ºC in the case of highly hybrid sols.

From the previous brief literature review, it may be inferred that the Sol-Gel method has been demonstrated convenient to control chemical composition, thus the refractive index and film thickness by single and multideposition techniques. Reduced costs and large area coatings are additional advantages of Sol-Gel processes, as compared with other techniques developed for the preparation of planar waveguides; in particular, those requiring the use of vacuum chambers. Deposition techniques such as dipping, spraying and spinning allow coating a wide variety of substrates and complex geometries via Sol-Gel. In addition, Sol-Gel techniques allow incorporating organic molecules for obtaining hybrid coatings, which have attracted considerable interest for the fabrication of sensors based on waveguides, as was presented by Jerónimo et al. [51].

The Sol-Gel synthesis consists mostly of hydrolysis and polymerization of organic and inorganic precursors, in order to obtain spatial networks covalently attached (Fig. 1.3). It is a two-step process [47-49]:

a) Hydrolysis step; in which precursors, usually alkoxides, are hydrolised, e.g. tetraethyl-orthosilicate (TEOS) form Si-OH. Among the various parameters that affect the rate of hydrolysis, pH and H_2O/alkoxide ratio are the most important and influence the type of catalyst and/or complex agents to be employed. This step can be performed by acid (our case) or basic catalysis;

$$(EtO)_3\text{-Si-O-Et} + H_2O/H+ \rightarrow (EtO)_3\text{-Si-OH} + EtOH \qquad [1.1]$$

b) Condensation step; where the hydrolyzed species are associated forming covalently linked networks, e.g. building bridges -Si-O-Si- .

$$(EtO)_3\text{-Si-OH} + Si(OH)_4 \rightarrow \text{-Si-O-Si-} \qquad [1.2]$$

Depending on the type of precursors employed, we can talk about different kinds of sols [52]:

- Inorganic sols; where the precursors are purely inorganic compounds;
- Hybrid sols; where we have a mixture of hybrid and inorganic precursors.

Sol-Gel technology has been applied for the last several years to prepare waveguides from inorganic and/or hybrid sols, developing a wide range of compostions [36-42, 53-55]. This research followed, basically, studies of P. Innocenzi [56] and S. Pellice [57]. P. Innocenzi et al developed different organic and inorganic sols based on the silica-titania system, and characterised their optical and microstructural properties [56]. S. Pellice et al developed highly hybrid synthesis starting from cyclic and unsatured organic compounds. In addition, studies of the dependence that the refractive index and thickness have with the composition, heat treatment, concentration, aging, etc. were made for optimizing the waveguides obtained by this technique.

Moreover, it is well-known that a minimum thickness value of the coating/layer is needed to make waveguiding of the light through coatings possible [10]. Theoretical calculations, extrapolating from what is known for optical fibers (see eqs. 1.3-1.5) suggest that the required thickness values must be twice the wavelength of light [8-10]. The solution when coatings are too thin is to fabricate the coating as a multilayered and/or hybrid structure. The number of propagation modes (N) travelling through the waveguide depends on the thickness (a), the characteristics of the coupling surface (S) and the beam parameters (wavelength, λ, numerical aperture, NA, and diameter of the spot, Ω) can be controlled by this multilayer process.

$$(\pi * a^2)/4 = \Delta S \qquad [1.3]$$

$$(2NA^2)/\pi \approx \Delta \Omega \qquad [1.4]$$

$$N = (\Delta S \Delta \Omega)/\lambda^2 \qquad [1.5]$$

1.2.2 Laser Zone Melting

As an interesting and facile alternative for the fabrication of planar waveguides, with respect to the traditional methods or Sol-Gel technology, the use of glass mixtures in the form of frits was studied. Since all of the above methods are considered expensive from an industrial processing point of view, either because of need for expensive starting materials, or for complex preparative procedures, the use of common industrial ceramic technology was considered here to explore the preparation of optical waveguides on common soda-lime glass substrates. In particular, the use of ceramic frit technology would be an advantage from the industrial standpoint. In this case, waveguides are prepared by surface coupling two glass layers which exhibit different refractive indices. The use of inorganic oxides as raw materials and its subsequent thermal treatment at high temperature allows obtaining glass coatings on the original substrates [58-60].

A mixture of inorganic oxides is deposited onto the substrate via screen printing. Several steps may be distinguished in the glass coatings production by frit deposition. First, the raw materials used must have an homogeneous and constant composition, and the absence of refractory particles. These may cause core degasification problems or contamination with metallic oxides which may induce a deviation in the characteristics required for the frit. The subsequent melting process provides the final homogeinization of the mixture and insolubilization of the resultant product, usually at high temperatures (1300-1500ºC). The result is turned out as starting materials widely used in the ceramic and glass industries, known as frits. The fusion of the raw materials is not produced simultaneously, due to the different melting points of the mineral components. Those which have lower melting points (such as borates and carbonates) yield an amorphous phase, which accelerates dissolution of the feldspar components and, gradually, the other compounds present in the original mixture [60].

Lead borosilicates have recently gained attention by many researchers for their application in optics, particulary for the fabrication of waveguides [61], and in electrochemistry, for their use in the development of solid-state fuel cells. In addition, glass powders are widely used as dielectric layers and fillers in various types of displays and ceramic capacitors [61-62]. Moreover, lead borosilicate glasses are also of technological interest because of their wide glass formation regions, low melting temperatures and high index of refraction. The bibliography searched allowed to suggest a mineral known as 'alamosite', with composition $PbSiO_3$ [63]. Developing this composition for amorphous coatings and having in view previous studies reviewed [61, 64-65], we developed formulations of lead borosilicates. The structure of ceramic frits employed is described through a network formed, mainly, by zig-zag chains of SiO_4 tetrahedra, with perpendicular helix chains of $[PbO_4]$ tetrahedra and $[PbO_3]$ pyramids. The introduction of boron involves the replacement of the units previously described by $[BO_3]$ triangles. This regular structure suggested its implementation as a light guiding element on a transparent substrate [66-67]. In order to use frit technology and take advantage of the high refractive indices available with many glass formulations existent in the Industry, it is also necessary to make use of an appropiate thermal treatment method that allows melting of the frit without causing damage to the glass substrate, a difficult task indeed. Thus, glassy powders of $PbO\text{-}B_2O_3\text{-}SiO_2$ were prepared using the traditional methods of melting inorganic oxides (Mixed oxide melting with high temperature furnaces) for their application onto commercial glass substrates. The objective was to obtain guiding elements onto optically inert buffers, with local refractive index changes, allowing guiding of light [68].

Recent advancements published in the literature [69-87] have demonstrated the advantages of the Laser Zone Melting (LZM) method to process thermal shock sensitive materials, particulary with preheated substrates. Although Larrea and Mora had initially demonstrated the high degree of microstructural control provided by LZM [70-74]. Important improvements were later published, based on the use of preheating [75-79] and novel optical beam maneuvering and sample translation devices [80-82]. Thus, the sintering process of inorganic oxides coated commercial glass substrates was made employing a CO_2 laser combined with a roller furnace. This technology allows sintering of inorganic

mixtures at low temperatures and in shorter times, compared to traditional melting methods, as well as the potential application of the technique at an industrial scale [69-87].

The application of the laser beam on the white surface causes high temperature gradients in relativelly small controlled areas, promoting local melting of the materials at the vicinity of the treated area [70-71, 88]. The use of the CO_2 laser offers several advantages over the methods based on traditional melting, particulary:

a) materials can grow quickly due to high thermal gradients generated at the solid-liquid interface;

b) a large area can be treated by the laser scanning along the surface of the sample.

1.2.3 Laser Ablation Backwriting of Metal Targets

In the last technique presented, we study the chemical processes involved in Laser Ablation Backwriting (LAB) of metal targets. This as a continuation of the research developed earlier by our group [29-30]. Two theses were previously presented; in Ruth Lahoz thesis [89] laser ablation backwriting of metals is thoroughly described, explaining the complex processes involved, the parameters that influence these processes and presenting one application to design electric circuits onto glass substrates through laser ablation of metal targets. The other thesis, developed by Antonio Castelo [90], established the fundamental principles for fabricating phase gratings and planar waveguides onto glass substrates by the same LAB method.

The advantages of planar glass waveguides and their preparation via laser ablation backwritting of metal targets have been extensively discussed in the recent literature [29-30]. In addition, laser ablation backwritting has also been applied to the successful fabrication of optical phase diffraction gratings [91]

and may be considered as a convenient method for the preparation of other optical devices.

An important aspect to consider in laser ablation backwriting of metals, deposited onto glass substrates, relates to the nature of the metal species evolving from the target during the ablation process. Although nanosecond (ns) laser irradiation has been commonly used initially for metal ablation [29-30, 91-92 and references therein], the most recent literature reports on work performed on metals with ultrashort pulsed lasers, within the picosecond (ps) [93-94] and femtosecond (fs) [26, 95-97] regimes. Ref [93] provides an excellent overview of laser ablation phenomena and processes carried out within the ns, ps and fs regimes. More particular characteristics of ultrashort pulse laser ablation of metals, within the ps regime, are reviewed for metal ablation efficiency in [94]. Chakravarty et al presented a comparison of ps and fs metal ablation in the context of nanoparticle size control as a function of pulse length [95].

Davies et al published pioneering work concerning the use of fs lasers to induce local changes within various glass substrates, using near IR irradiation [26]. They demonstrated that a focused fs laser beam could write transparent lines inside soda lime and other glasses with a 0.01-0.035 refractive index increase. They also confirmed formation of several types of structural defects and suggested that multiphonon absorption processes were behind this index change.

Qiu and coworkers have more recently described the interaction between fs laser pulses and glass substrates with the aim of controlling microstructure toward the development of applications in micro-optics [96-97].

The laser backwritting mehtod consists on the laser ablation of metal targets to achieve changes in the refractive index of glass substrates (Fig. 1.5). In this process, the passage of metallic particles is produced from the target to the substrate, achieving a change in the refractive index at the irradiated region. This procedure results in a number of advantages over other techniques: it is a one step process, not needing the use of external elements such as resins or masks, the experimental setup is simple and the process is very fast. Furthermore, it is

possible to obtain elements of different characteristics in a simple way, varying only the laser parameters, in a work area up to 120x120mm^2. The laser used is provided with a beam stearing system (galvanometer system) which allows moving the beam as desired in the XY plane, that supposes one advantage with respect to the previously work developed in Refs. 29-30.

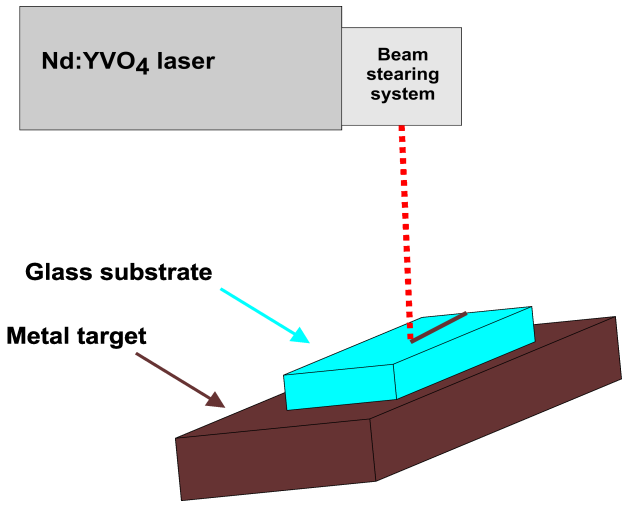

Figure 1.5: Experimental configurational for the Laser Backwriting process; the beam of a Nd:YVO4 laser is focused onto a metal target. The plasma plume originated evaporates metal species from the target, to deposit them into the glass substrate above it. The optical beam stearing mirror based system (galvanometer system) allows scanning with precision along the XY axis.

1.3 Glasses

Until today, different kinds of non-commercial glasses were used as substrates in the production of planar waveguides [11-27]. The most widely employed techniques involve the use of complex equipment and high economical cost, both by the technical complexity as the synthesis conditions, being neccesary the use of vacuum equipment or meta-stable reagents in many cases [98-99].

Recently researchers have focused their attention on glasses based on oxides of heavy metals (TeO_2, GeO_2, Bi_2O_3, PbO, etc.) as promising materials for photonic devices [100-102]. But the obtention of these materials supposed the availability of the necessary bulk starting materials or minerals, especial reactives or the use, in the most of cases, of special atmospheres or high melting temperatures.

Thus, in this study we researched economical and simple alternatives to employ as substrates and optically active coatings; always maintaining the necessary condition of chemical compatibility between guiding layer and substrate [98].

Sol-gel technology allows us to obtain layers of different composition and, in addition, there are several studies where this technique is applied to a wide variety of substrates [31-44, 103-104]. Always researching economical alternatives, the perfect suitability of this method was tested to obtain planar step-index waveguides onto commercial glass substrates.

The application of inorganic oxides to achieve changes in the substrate properties is in continuous development. The industrial production of such materials is well known and different manufacturing methods were described, analyzing the economical and technical characteristics of each one. The reliability and compatibility of these coatings onto borosilicate glass buffers has been demonstrated [105]. One step forward, in this research these coatings were applied onto commercial glass substrates and sintered by laser zone melting, getting optimal results in chemical and physical compatibility between materials while modification of the substrate was kept to a minimum.

Commercial glasses used as substrates correspond to the typical commercial compositon based on soda-lima silicates; offering chemical and physical compatibility with the guiding materials and providing, simultaneously, lower refractive indices. Soda-lima silicate glasses are mainly formed by silica, sodium and calcium. Silica is part of the raw material, sodium lowers the melting point and calcium confers chemical stability. Without calcium, the glass would be soluble in water and hardly be useless. These glasses melt easily and, moreover,

are very cheap, that means the final waveguide will be low-cost. The windows of buildings, from the largest to smallest are made of this glass. The chemical resistance of soda-calcium glass has been improved in recent years with the increase in the proportion of silica, due to its low chemical reactivity. It also increases its behavior against thermal shock, which in commercial glass stands at around 60 degrees. Under such gradient glass may shatter dangerously [106-108].

Borosilicate glasses were also employed, in this case, for the fabrication of waveguides by laser ablation of metal targets. Microscope slides were employed as substrates in laser ablation processes and in sol-gel coatings; in this case to facilitate the study of different film properties. This kinds of glasses were first discovered in 1912 and, after silica, its largest component is boron oxide. It is virtually inert, harder to melt and work. It offers a high resistance to thermal shock, but not as much as pure silica glass, which has a lower coefficient of thermal expansion. It is employed in the manufacture of kitchen utensils for furnace and laboratory supplies, because it is very resistant to heat and sudden changes in temperature [106-108].

Chapter 2

Experimental procedure

2.1 Fabrication methods.
- 2.1.1 Sol-Gel method
- 2.1.2 Laser Zone Melting
- 2.1.3 Laser Ablation Backwriting of Metal Targets

2.2 Characterization techniques.
- 2.2.1 Chemical and Microstructural characterization.
  - 2.2.1.1 IR/Raman Spectroscopy
  - 2.2.1.2 X-Ray Diffraction/Fluorescence
    - 2.2.1.2.1 X-Ray Fluorescence
  - 2.2.1.3 UV/Vis Spectroscopy
  - 2.2.1.4 Confocal Microscopy
  - 2.2.1.5 Scanning Electron Microscopy
  - 2.2.1.6 Transmission Electron Microscopy
- 2.2.2 Physical characterization
  - 2.2.2.1 Transport properties
    - 2.2.2.1.1 Electrical Conductivity
  - 2.2.2.2 Optical properties
    - 2.2.2.2.1 Refractive Index
      - 2.2.2.2.1.1 Refracted Near-Field Technique
      - 2.2.2.2.1.2 Variable Angle Ellipsometry
      - 2.2.2.2.1.3 Dark M-line Spectroscopy (The Mode Theory)
    - 2.2.2.2.2 Loss measurements
      - 2.2.2.2.2.1 Direct Coupling Method
      - 2.2.2.2.2.2 Direct Butt-coupling Method
      - 2.2.2.2.2.3 Double prism Method
      - 2.2.2.2.2.4 Method based on Scattered Light

2.1 Fabrication methods

This thesis explores the use of alternative, inexpensive methods to fabricate planar waveguides with the aim of demonstrating convenient and efficient processing methods suitable for industrial scale up. In addition, these may pave the way to acces a vast number of chemical compositions in comparison to the methods commonly used nowadays, as has been already outlined in chapter 1.

2.1.1 Sol-Gel method

In order to obtain good control in coating thickness and also over the refractive index with a relatively simple method, Sol-Gel technology was used, in combination with dip-coating, to obtain planar waveguides [45-46]. This work essentially followed, studies published by P. Innocenzi [56], for organic and inorganic sols, and by S. Pellice [57], for hybrid systems, in order to obtain waveguide layers with different refractive indices over optically inert substrates. In addition, studies were undertaken to compare the effects exerted by compostion, concentration, aging of the sol, heat treatment, etc., on the coating's refractive index and critical thickness in order to optimize the preparation of planar step-index waveguides by this technique.

Table I summarizes different compositions prepared by Sol-Gel, as well as the range of corresponding refractive indices obtained. Different compositions based on SiO_2, ZrO_2, TiO_2 e CeO_2 were prepared achieving refractive index values ranging between 1.45 and 2.10; following a Sol-Gel method and inorganic and hybrid (organic-inorganic) sols, previously described in the literature [56-57, 109-110]. This fact enables us to obtain a wide range of refractive indices that can be used for performing multilayer structures. Compositions that incorporate colloidal particles were also prepared; which, in principle, will cause light scattering, and thereby achieve colour phenomena on treated substrates.

Table I: Systems and compositions studied with their corresponding refractive indices (λ=632.8 nm).

System	*Acronym*	*Composition*	*Refractive index (n)*
SiO_2-TiO_2	Si-Ti	90:10 – 50:50	1.45 to 1.73
ZrO_2-CeO_2	Zr-Ce	90:10 & 70:30	1.98 & 1.99
SiO_2-$ZrO_{2\ colloidal}$	Si-ZrC	75:25	1.53
SiO_2-$ZrO_{2\ colloidal}$-$ZrO_{2\ alkoxide}$	Si-Zr	65:25:10	1.59
SiO_2-CeO_2	Si-Ce	95:5	1.47

Once a sol is obtained, we proceed to deposit the guiding layer over an optically inert substrate, in this case by the inmersion technique called "Dip-Coating". This process is based on dipping the substrate in a reservoir of liquid (solvent) that contains the material to be deposited (solute) by extraction at a constant rate. The thickness depends on the speed of extraction, which is governed by the tensions created between the liquid surface and the sample, or in other words, the solution viscosity and the degree of solvent evaporation (Fig. 2.1). The adhesion between layer and substrate depends on the characteristics of sol and substrate, so the final state of thin film bath depends on factors such as the surface of the substrate, the inmersion time, the speed of extraction, the number of inmersion cycles, concentration, temperature and humidity environment. To perform this technique the semiautomatic apparatus ilustrated in Figure 2.2 was developed. The Figure represents the substrate placed and displaced by a micrometer resolution optical displacement platform controlled by conventional PC software. The sintering step takes place through a programmed heat treatment in an electric furnace.

In order to satisfy the thickness restriction explained in section 1.2.1 of this Thesis, Sol-Gel multilayers were prepared to obtain a coating above the minimum thickness required for light guiding.

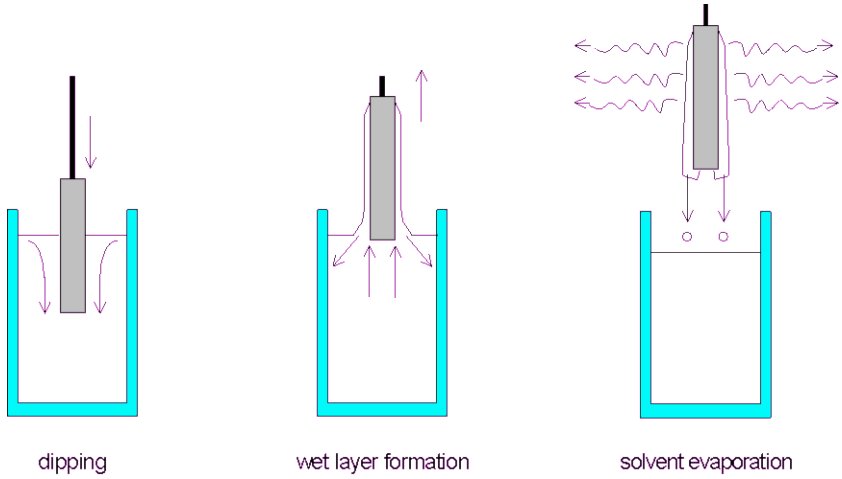

Figure 2.1: Scheme of the Dip-Coating technique used to prepare single and multilayer coatings via Sol-Gel. The substrate is dipped in the sol (left) and retracted at constant speed (center), to yield an uniform thickness film, which is subsequently heat treated (right).

Figure 2.2: Dip-Coating instrument composed of a micrometer optical platform aligned in the vertical position and controlled by a PC with conventional software.

a) Process 1: SiO_2-TiO_2 system (Si-Ti sol)

We prepared SiO_2-TiO_2 sols varying the molar ratio of each compound and using methyltriethoxysilane [MTES: $CH_3Si(OCH_2CH_3)_3$, 98%, ABCR] and tetraisopropyltitanate [TPT: $Ti(OCH(CH_3)_2)_4$, 97%, ABCR] as precursors for silica and titania, respectively, in acid environment. The synthesis was conducted in two stages; initially MTES is pre-hydrolysized with ethanol [EtOH: CH_3CH_2OH, Ethanol absolute PA-ACS-ISO, Panreac] as solvent, in the presence of HCl (0.1N). This mixture is stirred for one hour. Titanium alkoxide was complexed adding glacial acetic acid [AcOH: CH_3COOH, Acetic acid glacial PA-ACS-ISO, Panreac] as a complex agent, followed by stirring for one hour. Both solutions were then mixed and water was added dropwise until hydrolisis was completed. The mixture was maintained under stirring for one hour, yielding a yellow sol. The ratios used were: MTES/(H^+)=1; the H_2O/(total alkoxides) ratio was varied depending on the SiO_2:TiO_2 relation employed. Table II summarizes the SiO_2-TiO_2 and H_2O/alkoxides molar ratios as well as the total concentration (C_T) used.

Table II: Compositions, molar ratios and total concentration used for the preparation of the sols corresponding to Sol-Gel process 1.

MTES:TISP	***H_2O/Alkoxides***	***C_T (g/L)***
90:10	2	100
80:20	2	100
70:30	1.5	100
60:40	1.5	80
50:50	1.5	80

The described compositions were employed to prepare films onto glass substrates by dip-coating. These were sintered at 450 ºC for 30 minutes in a muffle furnace using a heating and cooling ramp of 10 ºC/min.

With the objective of increasing the film thickness, samples with compositions 70:30 and 50:50 were prepared in a multilayer structure. These multilayers were prepared as follows: successive immersions of the substrate in one of the above compositions were performed with an intermediate heat

treatment of 450 ºC for 15 minutes; between each inmersion. After these successive immersions, a final heat treatment at 450 ºC for one hour was performed.

Previous work published by Gonçalves et al [111] and Almeida et al. [112], where rare earths were employed as dopants, suggested the opportunity to dope with rare earths one of the compositions prepared above. In particular, doping was carried out with erbium, which presents an the pssibility of producing active waveguides [113], to verify that this doping process is achievable and sols as well as thin layers can be obtained with relative ease. Thus, the composition 70:30 was subjected to a rare earth doping treatment by dissolving erbium nitrate once the sol was obtained. The final sol had an Er^{3+} proportion of 5 mol% and it is denoted hereafter as SiTi-Er.

b) Process 2: ZrO_2-CeO_2 system (Zr-Ce sol)

With the aim to prepare films with higher refractive indices, we prepared sols based on zirconium oxide, whose refractive index is about 2. In addition, Ce oxide was also introduced in the expected glass network product. Zirconium tetraisopropoxide [TPOZ: $Zr(OCH(CH_3)_2)_4$, 23-28% free alcohol, ABCR] and Cerium nitrate [$Ce(NO_3)_3 \cdot 6H_2O$, 99%, Merck] were used as precursors for zirconia and for ceria, respectively. The corresponding sols were prepared by dissolving TPOZ in EtOH, adding, dropwise AcOH as a complex agent. The solution of hydrated Cerium nitrate was stirred for one hour and then added dropwise. The ratios used were different depending on the composition prepared, 70Zr/30Ce or 90Zr/10Ce (Table III). These sols must be kept in amber bottles, to avoid their degradation by exposure to sunlight, due to the presence of Ce. A final one day aging stepis neccesary before their future use. The ZrCe sols are stable during one week, following the above synthesis process.

Table III: Compositions, molar ratios and refractive indices determined for the preparation of the sols in the sol-gel 2 process.

Molar composition	***Refractive index (n)***	***H_2O/(Zr+Ce)***	***AcH/(Zr+Ce)***
90Zr:10Ce	1.9764	1	1
70Zr:30Ce	1.9906	1.8	2

Coatings were prepared by dip-coating and heat treatment at 450 ºC for 30 minutes.

As in the previous system, multilayer structures were prepared with the 70Zr:30Ce composition at an extraction rate of 24.5 cm/min and the subsequent intermediate heat treatments at 450 ºC for 15 minutes.

c) Process 3: SiO_2-$ZrO_{2\ colloidal}$ system (Si-ZrC sol)

Another interesting Sol-Gel process is the synthesis of a network from alkoxides and alquylalkoxides and the introduction of colloidal particles in order to increase the thickness of the layers.

The SiO_2-$ZrO_{2\ colloidal}$ sols with composition 75:25 were prepared using TEOS and MTES as precursors for silica and a colloidal suspension known as Nyacol [Nyacol Zr100/20, 20% in water, Nyacol] for zirconia; concentrated HCl is used as a catalyst. Silicon alkoxides were thus mixed with the colloidal suspension, and vigourous stirring was necessary in order to achieve optimum mixing. After several minutes of vigorous stirring, concentrated hydrochloric acid was added while stirring was maintained until a double change in appearance was produced, from transparent to milky, and viceversa. At this point, the mixture was abruptly cooled introducing it into an ice bath to prevent further progress of hydrolysis and condensation.

Coatings were prepared by dip-coating with this sol after its heat treatment at 450 ºC for 30 minutes.

d) Process 4: SiO_2-ZrO_2 system (Si-Zr sol)

In order to increase the refractive index of films from the previous system, part of SiO_2 was replaced by zircona in the form of alkoxide (TPOZ). Thus, we started from a SiO_2:$ZrO_{2\ alkoxide}$:$ZrO_{2\ colloidal}$ molar composition of 65:10:25. The introduction of colloidal particles supposes a change with respect to this type of compositions using the classical solgel synthesis. First, the silicon alkoxides mixture was maintained under constant stirring for one hour. Simultaneously,

TPOZ was placed for one hour in another flask, mixed with acetylacetone [acac: $CH_3COCH_2COCH_3$, 2,4-Pentanedione PA, Panreac], and added dropwise to avoid precipitation and form the stable zirconium complex. Initially, the solution had a milky tone that changed to a brownish transparent colour in minutes. To this solution, which was maintained under vigorous stirring, the zirconia colloidal solution was added, causing a milky hue appearance. Vigoruosly stirring for one hour before the final addition of HCl. As in the previous case, there was an inversion of colour and a pronounced increase in temperature. The sol was then cooled in an ice bath to prevent further progress of hydrolysis and condensation reactions from taking place. The sol was aged under constant stirring for a week before its use. This sol is stable at room temperature until for weeks after its synthesis.

The thin films were prepared as in the previous cases, using the dip-coating process and a heat treatment at 450 ºC for 30 minutes.

e) Process 5: TEOS-MPS-EDGMA system (Si-Ce sol)

The preparation of highly hybrid coatings was finally carried out as follows. In a 250 mL beaker, the required volume of tetraethyl-orthosilicate [TEOS: $Si(OCH_2CH_3)_4$, 99%, Merck], 3-metacryloxypropyltrimethoxysiloxane [MPS: $H_2C=C(CH_3)CO_2(CH_2)_3Si(OCH_3)_3$, 98%, Aldrich] and colloidal silica [Ludox AS-40, 40wt%, Aldrich] were placed; under vigorous stirring. After four minutes, the beaker was introduced in an ice bath to maintain the reaction temperature at around 5 ºC. The solution is turbid due to the inmiscibility of colloidal silica with alkoxides; for this reason, it is crucial to perform this step under vigorous stirring. Ethylenglycol-dimethacrylate [EGDMA: $CH_2=C(CH_3)COOCH_2CH_2OCOC(CH_3)=CH_2$, 98%, Aldrich], glycidilmethacrylate [GMA: $CH_2=C(CH_3)COOCH_2(C_2H_2O)$, 97%, Aldrich] and nitric acid were subsequently added. There was a double change in appearance, since the solution turned initially opaque white and finally it went back to transparent. After twelve minutes, 2,2'-azobis(isobutyronitrile) [AIBN: $(CH_3)_2(CN)CN=NC(CN)(CH_3)_2$, 98%, Merck], which is the initiator of the organic polymerization step, was added. Finally, Cerium nitrate was added to achieve a molar ratio of 95SiO2:5Ce. The Si-Ce sol is stable for one week after

its storage in amber bottles at 4 ºC, without appreciable degradation of its properties.

Coatings were prepared at different extraction rates with this sol. They were then sintered at 150 ºC for one hour. Higher temperatures may not be used because of the presence of large amounts of organic compounds.

f) Sandwich-type structures

A pair of Sandwich-type structures were prepared following the methodology described to obtain multilayers. These structures allow the introduction of two light beams in a single sample, one layer immediately over the substrate and another one in the third layer or outer layer. The second layer has a lower refractive index and acts as a cover equivalent to a sheath in a fiber waveguide structure, to induce beam confinement.

Tables IV and V summarize the Sandwich-type structures prepared using an extraction speed below the critical thickness of each composition. Heat-treatments were carried out at 450 ºC for 15 minutes in each case.

Table IV: Structure Sandwich-type 1.

Layer	***Composition***
1st (internal)	ZrCe (70:30)
2nd (cover)	SiTi (70:30)
3rd (external)	ZrCe (70:30)

Table V: Structure Sandwich-type 2.

Layer	***Composition***
1st (internal)	ZrCe (70:30)
2nd (cover)	SiTi (70:30)
3rd (external)	SiTi (50:50)

2.1.2 Laser Zone Melting

As a convenient alternative for fabricating planar waveguides, with respect to traditional methods or Sol-Gel, the use of glass mixtures in the forms of frits was studied. Powders mixtures within the system PbO-B_2O_3-SiO_2 were prepared using the traditional melting method of inorganic oxides (Mixed oxides melting) in order to apply the resutlant homogeneous glasses as coatings on commercial glass substrates. The purpose was to obtain inexpensive, scalable guiding elements onto optically inert substrates, based on their higher refractive index [68].

Mixtures were prepared from reagent grade commercial powders of PbO, SiO_2 e B_2O_3 (percentages by weight 76.24, 19.70 e 4.06 %, respectively); corresponding to the compositions desired. Later, a selected composition was doped with commercial powders of Yb_2O_3, Eu_2O_3 (5% mol) e Bi_2O_3 (2% mol), among others, to vary the optical and chemical frit properties, such as transparency, surface wetting/adherence or its refractive index. These reagents were mixed and homogenized in a planetary mill (PM100, Retsch). Once uniform grain size was achieved, the mixture was suspensed in isopropylic alcohol and deposited onto window glass substrates using the Doctor Blade technique (Fig 2.3). The thickness of the final frit coating depends highly on the concentration of the suspension.

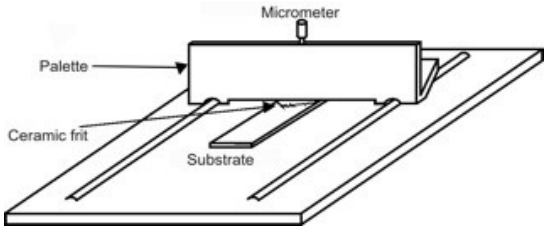

Figure 2.3: Deposition instrument for the inorganic oxides mixture, commonly known as the “Dr. Blade” technique.

The glass substrates were also subjected to mechanical and laser ablation treatments in order to obtain channels with different geometries for subsequent filling with the selected frits. Figure 2.4 illustrates schematically the deposition of frits into these channels. The adhesion of the frit coatings onto the substrate, as simple flat layers or in complex froms (curves and broken lines), was achieved with a heat treatment performed at 690 ºC in a muffle furnace. The high temperature soaking time depends on the concentration of the suspension and on the subsequent deposit. The minimum time needed is 4 hours, even for low concentration suspensions.

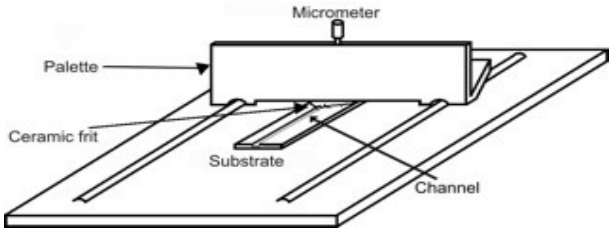

Figure 2.4: Frit deposition scheme on channel engraved substrates.

Carrying out this technique one step forward, the sintering process of ceramic frit-coated commercial glass substrates was achieved employing a patented apparatus consiting of a CO_2 laser generator with a power of 350W, excited by radio-frequency and combined with a roller kiln (Fig. 2.5) [80-82]. The adhesion of the frit coating to the substrate is obtained by CO_2 laser irradia of the substrate surface, which is maintained at sufficiently high temperatures by inside the roller kiln. This technology allows sintering of metal oxide mixtures at low external temperatures and with a substantial energy savings, and is suitable to be applied at an industrial scale [69-87].

The CO_2 laser was one of the first lasers to be developed (invented by Kumar Patel of Bell Labs in 1964), and it is still today one of the most employed in industry. The CO_2 lasers are continuous or pulsed high power gas lasers, which produces a beam of mid-infrared light with a main band of output wavelengths between 9.4 and 10.6 micrometers; because most materials absorb efficiently at these wavelengths, such lasers are widely employed in cutting and

other surface treatment applications of materials as varied as paper, cardboard, plastics, glass, quartz, ceramic, meat, tissues, stone or metal [88].

Figure 2.5: Image of the CO_2 laser system (EasyLaser) coupled to a roller kiln (Nannetti), used in the present work and patented by Estepa and de la Fuente [81].

In most CO_2 lasers, pumping is realised by gas discharge, a laser of this type uses a gas mixture of CO_2:N_2:He. The CO_2 molecules are the active laser medium, the N_2 serves as a mechanism of energy transfer and the protons of He raise the population inversion by "de-population" of low-power states. The population inversion in a CO_2 is established between the vibrational and rotational energy states. The impact of electrons excites the vibrational mode of nitrogen molecules, the transfer of the collision energy between nitrogen and carbon dioxide molecules causes the vibrational excitation of the carbon dioxide,

quite effectively to bring the necessary population inversion for laser operation. The nitrogen molecules are in a low excited state and its transition to higher states takes place by collision with cold helium atoms. The resultant hot helium atoms must be cooled to avoid one population inversion in CO_2 molecules [88].

An isopropyl alcohol inorganic oxide suspension was deposited via the Dr. Blade technique (Fig. 2.3) onto planar commercial, soda lime glass substrates. Sintering was carried out by introducing samples in a roller kiln (heated to 600 ºC and a sample traverse speed of 1.5 m/h) and, by focusing the beam of one CO_2 laser generator operating at 350W on the surface of these substrates (Fig. 2.6). The laser is equipped with a galvanometer system Scanlab®, with its interphase card RTC3PC.

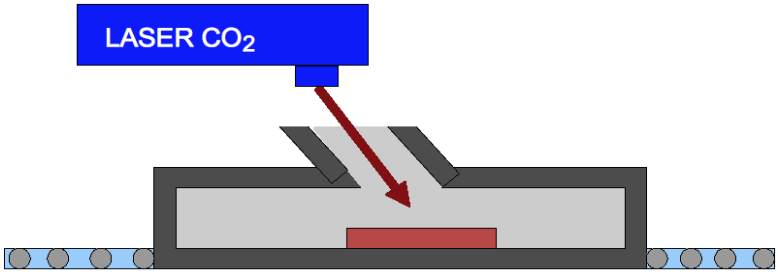

Figure 2.6: Scheme of the patented Laser Zone Melting apparatus used for the present work [80-81].

2.1.3 Laser Ablation Backwriting of Metal Targets

A Powerline E model (Rofin), 20W Nd:YVO_4 solid-state laser was employed for this study and is shown in the photopgraph of Figure 2.7. It is a widely used industrial apparatus with applications in micromachining, marking or surface treatment of a large variety of metals and polymers, and to a lesser extent in ceramics, glass and other materials. The rare earth element, Nd, is the active dopant, substituting for a small percentage of Y atoms in the Zircon type structure of the host, YVO_4. This laser doped medium is optically excited by a laser diode stack, emitting laser light at a wavelength of 1064 nm. The laser cavity is fitted with a Q-switch, which allow the laser to emit in cw or in pulsed

mode. In latter mode, the energy stored in the cavity is outputted within ns, so that pulses of intense irradiance are reachable which, upon efficient focusing, induce melting, evaporation and ablation of the material exposed. The insure minimal thermal excitation within the target material, although in this pulse width regime, thermal effects are always present to a significant extent. The diode excitation produces a higher overall efficiency due to a good match between the spectral emission and absorption band of Nd in the vanadate host. This results in a minimum thermal load for the laser crystal rod, leading to better beam quality by lowering thermal lensing effects, and allowing an increase in power and pulse frequency without sacrificing laser spot uniformity [88].

Commercial software allows to define the desired emission, irradiation and beam steering conditions, i.e., laser emission power, pulse frequency and width, as well as beam scanning parameters may be fixed under a wide range of values to adapt to materials properties and process requirements.

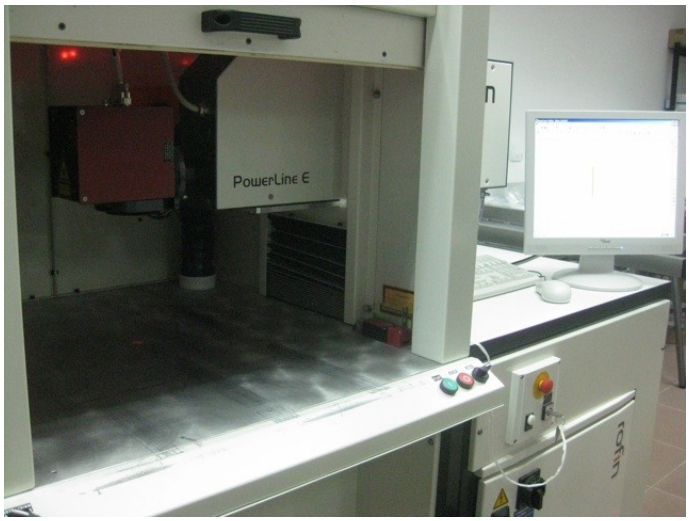

Figure 2.7: Powerline E model 20W Nd:YVO4 laser manufactured by Rofin®. The galvanometer head is enclosed within the red box on the left side of the photograph, placed at the resonator output and within a safety enclosure.

Tables VI and VII include characteristic laser emission parameters which depend on the laser diode pump currents and Q-switch oscillation frequencies, as originally provided by the manufacturer.

Table VI: Pulse widths vs different frequencies of the 20W Nd:YVO_4 laser; for a current of 27 A.

Frequencies (kHz)	5	10	20	30	50
Pulse width (nseg)	40	60	100	120	170

Table VII: Average Nd:YVO_4 laser output power (W) for different laser diode pump input currents and pulse repetition rates.

Current (A)	**Power (W)**		
	Frequency		
	CW	**10 kHz**	**50 kHz**
20	1.55	1.35	1.60
21	2.20	1.75	2.05
22	2.55	2.00	2.35
23	3.20	2.55	3.15
24	3.90	3.00	3.70
25	4.90	3.80	4.75
26	5.65	4.35	5.55
27	6.85	5.20	6.65
28	8.35	5.85	7.55
29	9.70	7.15	9.25
30	10.95	7.80	10.55
31	12.75	9.45	12.45
32	14.60	10.10	13.80
33	15.65	11.55	15.70

The laser head is fitted with a galvanometer system which allows the movement of the beam with nanometer accuracy, following the pattern designed in commercial CAD-type or similar programmes. The system sofware allows to vary, in addition to the output parameters listed above (Tables VI-VII), the beam scanning rate and geometry, giving acces to very complex geometrical patterns

and to an excellent control of pulse overlap and line spacing. The laser galvanometer head may be fitted with a diversity of flat-field lens. Two types of lenses with focal lengths of 100 mm and 160 mm, which respectively result in focal spots of ca. 11 and 19 µm, have been used throughout this work. The use of flat field lens guarantees a constant beam waist over a 24.5º solid angle.

In the Laser Ablation Backwriting (LAB) method followed here, the nanosecond pulsed laser is focused onto the surface of a metal target placed on the backside of a glass substrate. Since the glass is transparent to nIR radiation, the laser pulses travel through the substrate before impinging on the metal surface. The tightly focused laser beam induces evaporation and plasma formation on the surface of the metal target forming. A plasma plume of excited species is clearly visible during processing. The expected effect from such an energetic process is the inclusion of metal species on the substrate, without negative consecuences for the surface (Fig. 2.8). These inclusions, together with the associated stress and other electromagnetic phenomena induced in the glass matrix and at the atomic structural level expected to generate the desired change of refractive index on the original glass substrate [29-30].

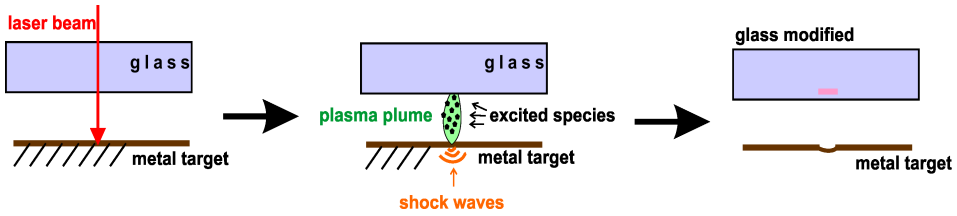

Figure 2.8: Scheme of the Laser Ablation Backwritting (LAB) process. The beam of the laser is focused onto the metal target, where it induces formation of a plasma plume containing excited species given off from the irradiated surface. These acelerated particles and excited species hit the glass surface and get incorporated into it. The irradiated area becomes modified physically and/or chemically, depending on the target used and on the laser emission parameters.

This method was first developed by R. Lahoz and A. Orera Utrilla [89, 114]. This thesis continues the work previously realised at the UA de Microóptica y Óptica GRIN of the USC-ICMA to demonstrate the feability of using LAB to affect the refractive index of glass substrates [29-30]. In the present work

specific objective was to perform further physico-chemical analysis and characterisation of the optical properties of the waveguides thus obtained, using additional metal targets such as aluminium and Ag in combination with commercial soda lime glass substrates. In general, techniques used to deposit films or to induce formation of waveguides in glass substrates, mainly with Ag, have utilized ion-exchange [115], ion implantation [116], photolithography [117] or CVD [118] methods in most cases. In this thesis the application of this technology was focused on the study of the chemical processes involved. This study attempts to contribute to understanding of the mechanism responsible for the modification of the refractive index at the substrate ablated with metal targets of Al, 63Cu37Zn brass alloy and Ag.

Waveguides were produced by the LAB procedure outlined above (Fig. 1.5). Commercial soda lime glass and microscope slides were employed as substrates. Al (Aluminium metalic foil, 99.0%, Goodfellow), 63Cu37Zn brass (Cu63Zn37 metalic foil, Goodfellow) and Ag (Silver plates, 95.0%, Agalex) 1 to 3 mm thick metal foils or plates were used as targets to deposit lines of ablated material on the glass surface. The laser parameters used for each target are summarized in Table VIII.

Table VIII: Laser conditions applied for each metal target used for modifying commercial glass substrates by the Laser Backwriting (LAB) process.

Metal	Power average (W)	Frequency (kHz)	Mark Speed (mm/seg)	Irradiance (W/cm^2)
Aluminum (Al)	5.03	50	500	$5.03x10^9$
Brass (Cu/Zn)	6.22	10	500	$1.10x10^{10}$
Silver (Ag)	6.56	20	50	$4.14x10^9$

After laser exposure, the samples are cleaned to remove contaminant debris from the substarte's surface, appearing from metal oxidation processes and evaporation of nonmetal surface contaminants, in order to determine the refractive indices and loss measurements, as well as to perform other physico-chemical analyses [29-30]. This is carried out washing the samples in acid baths for one hour; in the case of Ag an HCl 0.1M solution is used, while agua regia is employed for the other samples.

In order to check for the influence that oxygen (in air) may have on the LAB process, a vacuum was implemented to perform LAB under controlled, oxygen exclusion conditions. This allows comparison of the atmosphere effects in two different environments when the same laser processing parameters are applied. A cylindrical vacuum chamber of 306x400 mm^2 manufactured by Trinos and equipped with a pumping system composed of a primary pump (Pfeiffer model DUO 5M) and a turbomolecular pump (Pfeiffer model HiPace300/TC110) was introduced into the laser enclosure. The laser beam passes through a quartz window and is focused on the metal target situated inside the vacuum chamber. The glass substrate is placed over the metal target. The LAB process is employed as described above, although in this case the atmosphere is vacuum with pressures close to 9.8 x 10^{-7} mbar) and the laser lens employed has a focal length of 160 mm, in order to account for the larger distance to the target inside the vacuum chamber. The experimental parameters are the same as those used in air. Metallic coatings with dimensions 50x4 mm^2 were thus deposited onto commercial glass substrates by in vacuo. It was observed that, as the laser ablated the metal target, an increase in pressure was registered. When the ablation process ended, the pressure went back to the original value before LAB. The laser conditions employed for each metal, as well as the starting and maximum pressure, were registered and are collected in Tables IX- XI.

Since it was of interest to measure the conductivity of these metallic coatings as prepared in vacuo, they were not cleanned with acid.

Table IX: Laser parameters varied in the ablation of aluminium and the initial (P_0) and maximum ($P_{máx}$) pressure values when the treatment was realised under high vacuum conditions.

Condition	Power average (W)	Frequency (kHz)	Speed (mm/s)	Width line (µm)	Irradiance (W/cm^2)	P_o (mbar)	$P_{máx}$ (mbar)
1	5.59	20	100	30	$3.09x10^9$	$7.4x10^{-7}$	$1.0x10^{-6}$
2	6.56	20	100	40	$4.14x10^9$	$7.4x10^{-7}$	$1.1x10^{-6}$
3	6.56	20	100	30	$4.14x10^9$	$7.2x10^{-7}$	$1.1x10^{-6}$
4	5.59	20	150	40	$3.09x10^9$	$7.2x10^{-7}$	$1.3x10^{-6}$
5	5.59	20	150	30	$3.09x10^9$	$7.2x10^{-7}$	$1.2x10^{-6}$
6	6.56	20	150	50	$4.14x10^9$	$7.2x10^{-7}$	$1.3x10^{-6}$
7	6.56	20	150	40	$4.14x10^9$	$7.2x10^{-7}$	$1.3x10^{-6}$
8	7.54	20	150	50	$5.13x10^9$	$7.2x10^{-7}$	$1.5x10^{-6}$
9	7.54	20	150	30	$5.13x10^9$	$7.2x10^{-7}$	$1.2x10^{-6}$
10	7.54	20	250	50	$4.14x10^9$	$7.2x10^{-7}$	$1.8x10^{-6}$

Table X: Laser parameters varied in the ablation of silver and the initial (P_0) and maximum ($P_{máx}$) pressure values when the treatment was realised under high vacuum conditions. The work frequency was 10 kHz.

Condition	Power average (W)	Speed (mm/s)	Width line (µm)	Superposition (%)	Irradiance (W/cm^2)	P_o (mbar)	$P_{máx}$ (mbar)
1	3.98	50	60	0	$5.03x10^9$	$8.4x10^{-7}$	$1.0x10^{-6}$
2	3.98	50	50	0	$5.03x10^9$	$8.4x10^{-7}$	$1.0x10^{-6}$
3	3.98	50	30	0	$5.03x10^9$	$8.4x10^{-7}$	$9.9x10^{-7}$
4	4.67	50	60	0	$6.88x10^9$	$8.4x10^{-7}$	$1.0x10^{-6}$
5	4.67	50	30	0	$6.88x10^9$	$8.4x10^{-7}$	$9.9x10^{-7}$
6	4.67	50	100	90	$6.88x10^9$	$8.4x10^{-7}$	$9.5x10^{-7}$
7	5.46	50	100	90	$8.78x10^9$	$8.4x10^{-7}$	$9.7x10^{-7}$
8	5.46	100	100	90	$8.78x10^9$	$8.5x10^{-7}$	$1.0x10^{-6}$
9	4.67	100	30	0	$6.88x10^9$	$8.5x10^{-7}$	$1.2x10^{-6}$
10	3.98	100	30	0	$5.03x10^9$	$8.5x10^{-7}$	$1.4x10^{-6}$

Table XI:Laser parameters varied in the ablation of brass and the initial (P_0) and maximum ($P_{máx}$) pressure values when the treatment was realised under high vacuum conditions.

Condition	Power average (W)	Frequency (kHz)	Speed (mm/s)	Width line (µm)	Irradiance (W/cm^2)	P_o (mbar)	$P_{máx}$ (mbar)
1	6.56	20	250	40	$4.14x10^{9}$	$9.6x10^{-7}$	$4.2x10^{-6}$
2	6.56	20	250	30	$4.14x10^{9}$	$9.7x10^{-7}$	$3.1x10^{-6}$
3	6.56	20	500	40	$4.14x10^{9}$	$9.7x10^{-7}$	$7.4x10^{-6}$
4	6.15	15	250	40	$5.58x10^{9}$	$9.9x10^{-7}$	$5.0x10^{-6}$
5	6.15	15	250	30	$5.58x10^{9}$	$9.9x10^{-7}$	$4.0x10^{-6}$
6	6.15	15	500	40	$5.58x10^{9}$	$9.9x10^{-7}$	$9.9x10^{-6}$
7	6.15	15	500	30	$5.58x10^{9}$	$9.9x10^{-7}$	$7.6x10^{-6}$
8	7.54	20	250	40	$5.13x10^{9}$	$9.8x10^{-7}$	$6.0x10^{-6}$
9	7.54	20	250	30	$5.13x10^{9}$	$9.9x10^{-7}$	$4.9x10^{-6}$
10	7.54	20	250	20	$5.13x10^{9}$	$9.9x10^{-7}$	$3.8x10^{-6}$
11	7.10	15	250	40	$6.98x10^{9}$	$9.9x10^{-7}$	$6.0x10^{-6}$
12	7.10	15	250	30	$6.98x10^{9}$	$9.9x10^{-7}$	$4.7x10^{-6}$
13	6.22	10	250	40	$1.10x10^{10}$	$1.0x10^{-6}$	$6.2x10^{-6}$
14	6.22	10	250	30	$1.10x10^{10}$	$9.9x10^{-7}$	$5.2x10^{-6}$
15	6.56	20	100	40	$4.14x10^{9}$	$8.6x10^{-7}$	$3.7x10^{-6}$
16	6.56	20	100	30	$4.14x10^{9}$	$8.6x10^{-7}$	$3.6x10^{-6}$
17	6.15	15	250	50	$5.58x10^{9}$	$9.2x10^{-7}$	$7.6x10^{-6}$
18	6.15	15	250	20	$5.58x10^{9}$	$9.9x10^{-7}$	$3.5x10^{-6}$
19	6.15	15	100	30	$5.58x10^{9}$	$8.6x10^{-7}$	$3.6x10^{-6}$
20	6.56	20	500	30	$4.14x10^{9}$	$8.8x10^{-7}$	$7.6x10^{-6}$

2.2 Characterization techniques

2.2.1 Chemical and Microstructural characterization

2.2.1.1 IR/Raman Spectroscopy

Infrared spectroscopy (IR) was carried out employing a Bruker spectrophotometer, model IFS-66v with a resolution of 0.25 cm^{-1}. Raman spectroscopy was obtained using a FT-Raman Bruker module coupled to modul FRA 106 equipped with a 350 mW Nd:YAG laser with an excitation wavelength between 3500-20 cm^{-1}, using a Ge detector cooled with liquid N_2 [119].

Infrared and Raman spectroscopies are related to the vibrational and rotational modes in molecules and solids. Both spectroscopies characterize transitions that take place between quantifized vibrational levels, although the mechanisms that induce these transitions are different [119].

In infrared spectroscopy, the molecule absorbs energy and bounces from one vibrational level to another one. On the other hand, Raman spectroscopy is based on light scattering phenomena. When a monochromatic beam of light focuses on a sample and the frequencies of scattered light will be in phase, most of the light will be scattered without change, giiving way to a process known as Rayleigh Scattering. A small portion of incident light, however, will be scattered with changes in its original frequency, thus, the resultant frequencies exhibit higher or lower values with respect to the original resonant frequency; these are denoted as Raman frequencies [119].

The difference in molecular excitation mechanisms causes the existence of different selection rules, so that Raman does not replace Infrared spectroscopy, and both techniques are rather complementary. Thus, both in the Raman and IR spectra the 3n-6 (or in same cases 3n-5) normal resonant vibration modes, according to the selection rules imposed by molecular symmetry, are expected to be observed. Indeed, the so-called “rule of mutual exclusion” applies to

centrosymmetric molecules, where similar resonating peaks related to similar vibrational resonance modes are not observed in both, Raman and IR spectra. Thus for structure studies both, IR and Raman spectra may be very useful and complimentary [119].

In addition, however, Raman spectroscopy may show some advantages over IR spectroscopy:

1.- The complete Raman spectrum, between 4000-10 cm^{-1}, can be obtained in one experiment, as opposed to nIR and midIR measurements, where at least two are required with different spectrometers.

2.- In quantitative analysis, Raman spectroscopy has the advantage that the intensity of a band is directly proportional to the concentration of the substance; in IR spectroscopy the relationship between the intensity of a band and the concentration exhibits logarithmic behavior and may not be used for quantification purposes.

3.- Raman spectroscopy requires no special sample preparation, and the sample is completely recoverable; unlike, Infrared spectroscopy, which in the case of powders or molecular substances, involves the use of sample preparation for analysis which may make the original substance unrecoverable.

4.- The interpretation of the Raman spectrum is much simpler than that from an IR spectrum, since in the former, each band corresponds to one composition structure type or bonding situations; however, in the IR a band can correspond to the resonance of a bond type of different structures or moieties with different or similar composition than those present in other bands in the spectrum.

5.- The use of lasers as excitation sources, allow to obtain the Raman spectrum in a few miliseconds and with spatial resolution. This is a very important factor in the study of fast chemical reactions or short-lived species, and to complement microstructural observations with structural and compositional data.

In essence, however, both techniques are applied for quantitative and qualitative analysis to obtain information on functional group composition and also on structural features. From the qualitative point of view they help determine the presence or absence of certain functional groups or moieties, as a

function of the appearance or disappearance of characteristic bands within the spectra [119].

2.2.1.2 X-Ray Diffraction and Fluorescence

For the analysis of crystal structures that can potentially form within the coating and affect its properties significantly, samples were analyzed using a Siemens D5005 X-ray diffractometer. X-ray diffraction (XRD) is based on the similarity between the wavelengths of some X-rays and the distance among the atomic planes in crystalline solids. When an X-ray beam focused on a crystalline solid, variable intensity diffraction peaks appear because of reasons explained below. The geometric conditions necessary in order to produce diffracted beams by reflection are discussed in relation to Figure 2.9 [58].

Consider a beam of monochromatic X-rays irradiating a crystal surface, as shown in Fig. 2.9. To simplify, crystalline planes of dispersion atomic centers are replaced by crystalline planes that act as mirrors reflecting an incident beam of X-rays. In Fig. 2.9(a), horizontal lines represent a set of crystal planes parallel with Miller indices (*hkl*). When the monochromatic X-rays of the beam imping on a material, the diffraction pattern produced allow determining the structure of this material using Bragg's equation and reference fingerprint type patterns determined for known structures and published in the literature and in specialised data bases [58].

Considering the incident X-rays 1 and 2 as shown in Fig. 2.9c; so that these rays are in phase, the additional distance traveled by ray 2 which is equal to MP+PN, should be equal to the whole number of wavelengths λ. Thus:

$$n\,\lambda = MP + PN \qquad [2.1]$$

where n = 1, 2, 3, ... and called 'diffraction order'. Since MP and PN are equivalent to d_{hkl} sen θ, where d_{hkl} is the interplanar space or the distance between planes of the crystal with indices (*hkl*), the condition for constructive interference should be:

$$n\,\lambda = 2d_{hkl}\,\text{sen}\,\theta \qquad [2.2]$$

This equation, known as Bragg's Law, gives a relationship between the angular positions of diffracted beams as a function of the wavelength λ of X-ray incident radiation and as a function of the interplanar spacing d_{hkl} of the crystalline planes [58].

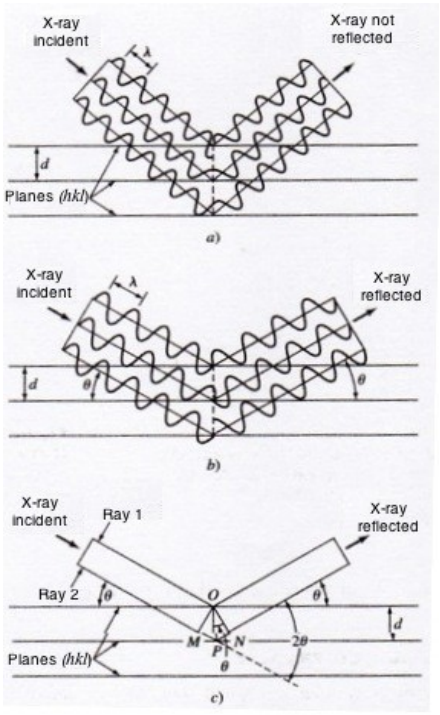

Figure 2.9: Reflection of a X-ray beam by crystal planes (*hkl*). a) The beam is not reflected in an arbitrary angle of incidence. b) In the Bragg angle θ, reflected beams are in phase and reinforced between them. c) Analogous to b) except that it omitts the representation of the wave, for the sake of clarity.

2.2.1.2.1 X-Ray Fluorescence (XRF)

X-Ray Fluorescence Spectrometry was used to identify the chemical elements present in a sample of lead borosilicate frit; employing a fluorescence spectrometer for weak elements (XRDRTF2), manufactured by Dr. Andrij Cheburkin and developed at the USC,.

X-ray fluorescence spectrometry allows us to identify and quantify the chemical elements present in the sample in a fast and precise way without any prior treatment of the sample. The composition of the sample is obtained in a semi-quantitative accuracy, without information regarding to its chemical state (oxidation, bonds or degree of crystallinity). The USC instrument identifies elements with atomic weights ranging from Mg to U [120].

The electrons are distributed on different levels and sublevels of energy inside the atom. Electrons are located occupying the lower energy levels when they are in their "fundamental state" [121]. If these atoms are bombarded with an electron beam or X-ray photons, a small part of the energy is used to produce the characteristic X-ray spectrum of elements present in the sample. The process for producing this characteristic spectrum can be summarized in the following steps:

- Excitement: the impact of one incident electron or photon with an electron from the atom inner energy levels, produces the electron's expulsion leaving the atom in an excited state.

- Emission: the excited atom tends to return immediately to its fundamental state, so that electron jumps from higher external levels to the inner electronic levels are produced. The energy released in the process is equal to the difference in energy between the levels implicated in such jump, and appears in the form of electromagnetic radiation within the X-ray region of the electromagnetic spectrum [121].

The excitement produced by bombarding electrons is called "primary excitation", and the radiation thus observed is called "primary X radiation". The

X-ray tubes are sources of primary X radiation; this radiation is also produced in the electron microscope, due to the sample irradiation by an electron beam; and is used for the chemical analysis of the sample. The excitation process with other X-rays is called “secondary excitation”, and the X-rays produced by the excitation of other X-rays is known as “X radiation” or “fluorescence radiation”. The characteristic of the secondary X radiation is used for chemical analysis with the frame of X-ray fluorescence spectroscopy [121].

As the energies of different electronic levels are characteristic for each atom, X-rays will be observed for each element present in the substance, as long as it is within the limtis established for the experimental apparatus employed. This is so because the detected radiation originated from transitions between internal electronic levels, whose energies are not affected by interatomic bonding [121].

When the energy of electrons that irradiate one atom is equal or greater than its corresponding K energy level, the expulsion of one electron from the same K level may occur; the transitions from upper electronic levels give rise to a series of characteristic wavelength radiations that are denoted as the “K series” (K_α, K_β, ...). If the vacancy occurs from one of the sublevels of the level L, the transitions from upper levels give rise to characteristic radiations of the L series (L_α, L_β, ...). The same can be described the same for the M level (Fig. 2.10). The K series is the most energetic of the three [121].

Although the number of possible features for each radiation element is great, in practice, the intensity of many of them is very small (very low probability of the electronic transition occurrence), and cannot be registered with standard measuring equipment. Moreover, the type of radiation emission lines recorded is further limited, because the energy difference between some of them is so small that they may overlap. This means that in practice, the characteristic XRF spectrum of an element is reduced to two or three lines in the K series, and four to ten in the L series. Emission lines for the M series, under normal conditions only appear for the heavier elements [121].

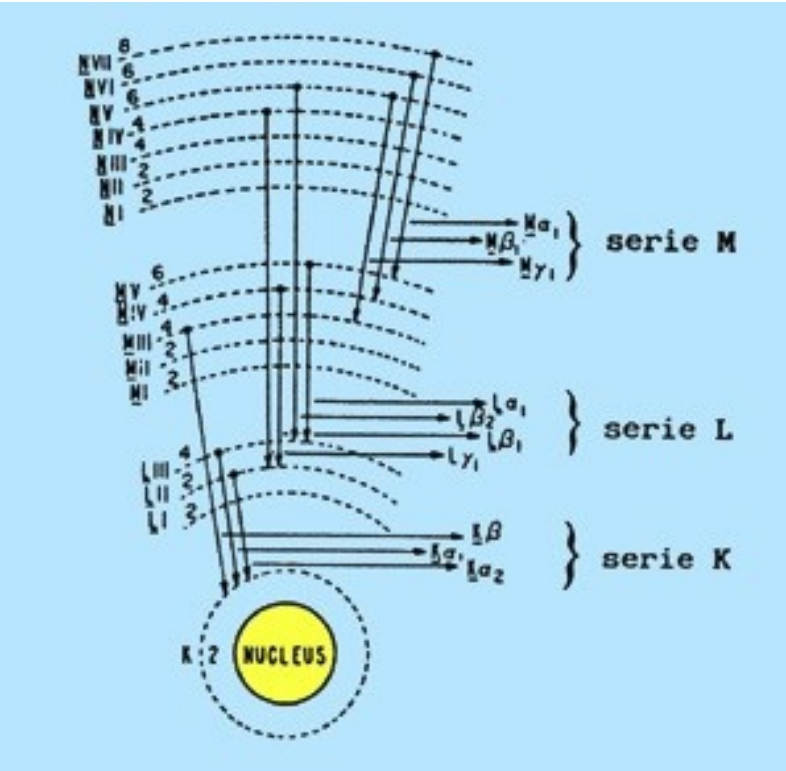

Figure 2.10: Scheme representing the electronic transition series (K, L and M) between internal electronic levels within an atom [121].

2.2.1.3 UV/Vis Spectroscopy

Ultraviolet-visible Spectroscopy (or UV/Vis Spectrophotometry) involves the study of electronic transitions corresponding to electrons in atomic and/or molecular energy levels with energies photons in the range of several eVs (ca. 6.2-1.1 eV from the UV to the nIR) (Fig. 2.11). This technique uses the light in the visible and adjacent ranges (UV) and the near infrared (nIR). This technique is usually complemented with fluorescence spectrometry, which deals with de-excitation transitions taking place from the excited to the fundamental state. Absorption spectrometry measures the excitation transitions taking place between fundamental and excited energy states [122].

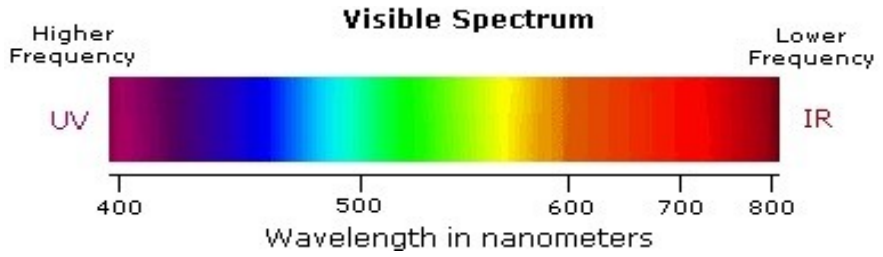

Figure 2.11: Visible spectrum; each wavelenght is represented with its corresponding colour.

UV-Vis spectra are also affected by the concentration of the absorbing species in the sample. All absorption techniques assume that when the sample is irradiated there is a partial absorption of this radiation, which causes a transition between energy levels of the species present in the sample (atoms, molecules or ions) from the fundamental, X, to an excited state, X*; the nonabsorded radiation is transmitted through the sample, as exemplified in Fig. 2.12, where spectra corresponding to microscope slide glass and commercial glass are represented. Thus, analyzing both, transmitted and absorbed radiation, a basic idea of an effective transmission window for our waveguides may be specified [122].

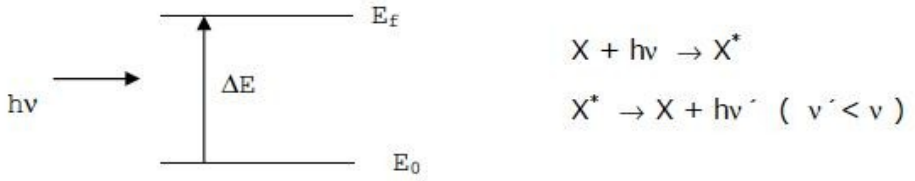

Figure 2.12: Scheme of electronic transition between the fundamental state (E_o) and excited states (E_f) of species (atom, molecule or ion).

The ΔE is characteristic of each substance and provides for a qualitative analysis of the material. This parameter is defined as:

$$\Delta E = E_f - E_0 = h\upsilon \qquad [2.3]$$

where h is the Planck constant and υ is the frequency of the energy needed to promote one electron from the fundamental state to the first excited state.

The proportionality between the intensity of light absorbed or transmitted and the analyte concentration is defined by the Lambert-Beer Law;

$$I = I_0 e^{-\varepsilon lc} \qquad [2.4]$$

where I_0 and I are the intensity (or power) of the incident light and the transmitted light, respectively; ε is the absorbance coeficient, c the concentration of the substance and (l) is the path length. Extrapolating to waveguides, we could determine the optimum composition for a waveguide considering the parameters that increase transmitted light to a maximum value. This relationship has enable, in addition, the development of analytical methods widely used in the determination of substances in solution [122].

UV-vis spectroscopic studies were carried out in order to (I) study the elements present in the sample with a non-destructive analytical method; and, (ii) study the possible transmission of light at the He-Ne wavelenght (633 nm) for each material studied. This probe serves to evaluate adequate guiding wavelengths for each material.

The use of UV-vis spectroscopy allows obtaining some type of fingerprint for each substance, as well as further information, as observed in Fig. 2.13 where we compare the spectra of the substrates employed. It may thus be possible to distinguish the presence of pure or doped substances, to obtain an approximate idea of the particle size or even to distinguish between the presence of suspended particles from the formation of new substances which may be amorphous in nature [123-128]. For example, the size and morphology of metal nanoparticles dispersed in a transparent medium is of significant importance for waveguiding properties, since their corresponding Surface Plasmon Resonance (SPR) characteristics have been shown to affect waveguiding properties to a considerable extent [129-130]. All spectra are represented in transmission percentage; the value for absorbance is inversally proportional to the tranmission value. The measurements are made with the light focusing perpendiculary to the

coatings; this configuration allows us to have an idea of the refractive index difference between substrate and coating.

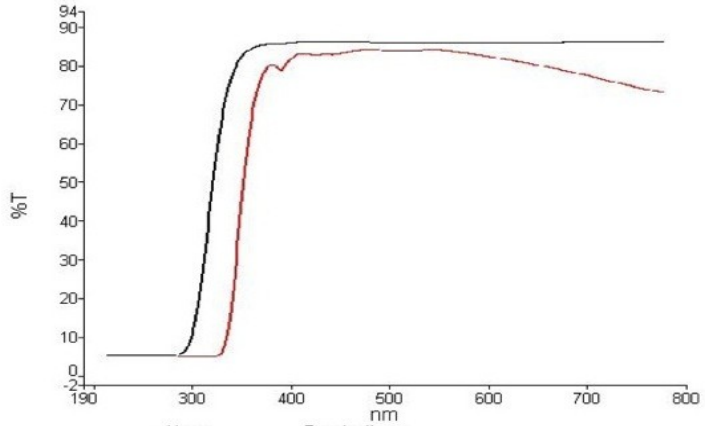

Figure 2.13: UV-Vis transmission spectra of microscope slide glass (black) and commercial window glass (red) samples.

2.2.1.4 Confocal Microscopy

The study of the morphological structure of the surface of samples developed was performed using a dual microscope Sensofar Plμ 2300 working in confocal configuration, with 10x, 20x, 50x and 100x objectives and commercial analysis software provided by the manufacturer. The technique was also used to study and compare channels engraved by mechanical (Fig. 2.14) and laser ablation (Fig. 2.15) machining of the substrate surface before frit deposition and melting. The previous Figures show photographs of commercial glass samples after mechanical and laser machining, respectively. This characterization was performed at the *Instituto de Ciencia de Materiales de Aragón* (ICMA-CSIC, Zaragoza).

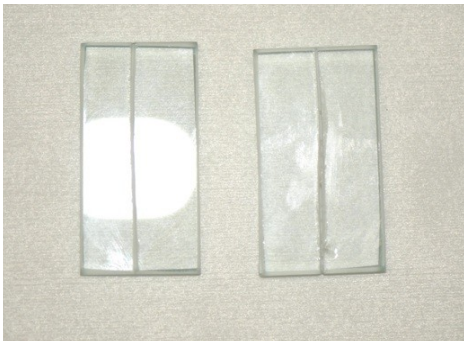

Figura 2.14: Image of mechannically engraved channels onto a commercial glass substrate.

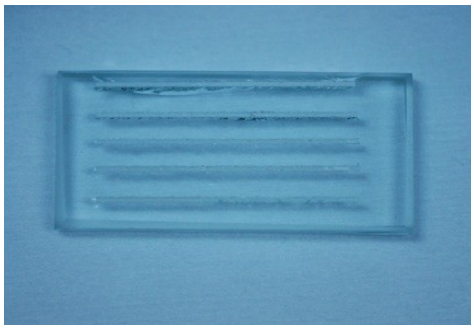

Figura 2.15: Image of laser-engraved channels obtained on a commercial glass substrate.

The Confocal Microscopy supposes a substantial improvement of classical techniques of optical microscopy (bright field and fluorescence), resulting in great interest for various branches of science such as medicine, biology, materials science, geology, etc. Its success is due to obtaining good images of greater clarity and contrast, greater vertical and horizontal resolution and the possibility to obtain "optical sections" of the sample, allowing its three-dimensional study. In the classical techniques of optical microscope observation, the light interacts with various depths, showing that the image that reaches the observer shows areas which are out of focus. This effect is due to the light reflected from areas outside the focal plane which leads to image degradation with respect to contrast and resolution. The principle of Confocal Microscopy is based on removing the reflected or fluorescence light coming from the planes

which are out of focus. To do so, a small area of the sample is illuminated and captures the light beam coming from the focal plane, removing beams originating from the planes above and below [131].

The invention of the first confocal microscope is attributed to Marvin Minsky, who designed a microscope in 1955 that allows observing neural networks in untinted nervous net preparations. Modern confocal systems are based on the principle which he patented in 1957 [131]. The original design is based in the presence of two pinholes: one located between the light source and the objective, and the other one, between the objective and a photomultiplier (Fig. 2.16). Both should be perfectly aligned so that the latter did not pass any light "out of focal plane" to the photomultiplier which is the basis of the whole confocal system. However, the technology of his time did not allow him to show the full potential of this new technique. The spectacular development of laser technology, computer systems and digital image acquisition allowed to exploit all possibilities for this technique. Thirty years after, his method is called "Confocal Scanning Microscopy" and combines the fluorescence microscope with electronic image and points of light provided by laser light directly focused onto the specimen, to obtain three-dimensional images [131-132].

Since the amount of incident light over the sample is too small, it is necessary to utilize powerful sources. A laser beam passes first through the pinhole, afterwards passes through the mirror, as shown in Fig. 2.16. Finally, the beam passes through the objective lens which focus it onto the sample under observation. The light emitted by the sample is received by the objective lens and reflected by the dichroic mirror. The latter totally reflects light at an angle of 45º. This light passes through the pinhole opening which does not allow the passage of the fluorescence caused by the planes out of focus. Then, only the light from the focal plane reaches the detector. Initially, this type of technique allows to observe clearly a single point at which it was necessary to make a clay sample, which required a longer time to obtain a complete picture. To accelerate the image capturate rate, some microscopes displaces the beam with oscillating mirrors. These require that the incident light flows quickly through the sample. These mirrors allow building the image in less than a second. Other systems use pinholes, which accelerate sweeping lines instead of points. Currently, these

microscopes are complemented with digital image processing, giving as a result the three-dimensional construction of samples [131-132].

The confocal system used measures heights on surfaces, ranging from very smooth (tens of nm) to very rough (hundred of μm). A sample is vertically scanned in different planes, thus each point on the surfaces passes through the focus. The system has a high lateral resolution ranging from 0.935 μm (10x) to 0.311 μm (100x). The vertical resolution is in the nanometer scale [131-132].

This microscope may work in interferometric mode, where it combines the light reflected from the sample with a reference beam to form interference fringes. The resolution in such a mode is increased to a value approaching 20 nm [131-132].

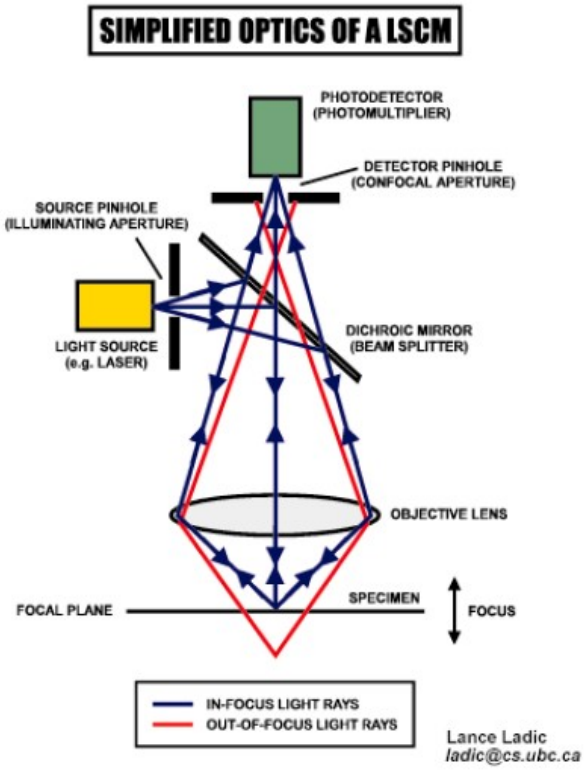

Figura 2.16: Functionality scheme of the confocal microscope designed by Marvin Minsky [133].

2.2.1.5 Scanning Electron Microscopy

Part of the microstructural studies were performed by Scanning Electron Microscopy (SEM) (Fig. 2.17). The scanning electron microscope is used to measure microscopic characteristics, classification of fractures, studies of the microstructure, the compositional and microstructural profiles in thin and thick coatings, study of coating-susbtrate interfaces at a microscopic level, incorporation of contaminants and failures analysis in materials, among others [134-135]. In this type of equipment, semiquantitative analysis is performed with an incorporated X-ray spectrometry unit (EDX).

Figura 2.17: Image of a commercial Scanning Electron Microscope (SEM) where the electron acceleration column and observation chamber are on the left and the computer control is on the right side.

The scanning electron microscope focuses a beam on a point on the surface of the sample and detects and displays the backscattered secondary electrons reflected from its surface, which are converted into electronic signals and displayed on a monitor. Fig. 2.18 schematically illustrates the main components that conform an SEM apparatus. Basically, an electron gun produces a beam of electrons in a vacuum column that are directed and focus onto a small section of the sample. The magnetic lens system allows beam scanning sweeps over a small area of the sample surface. Electrons with a smaller angle of dispersion

interact with the protusions at the surface and generate a scattering of secondary electrons that induce an electronic signal that in turn produces an image with a depth of field aproximately 300 times greater than an optical microscope. The resolution of the SEM instruments is about 5 nm, with a broad range of magnification (between 15 and 1000000 x) [134-135].

Sample characterisation by scanning electron microscopy has been carried out by employing different electron microscopes; in collaboration with expert groups elsewhere.

1 LEO435-VP: scanning electron microscope operated at 30 kV and equiped with an energy dispersive x-ray detector and analytical system (EDX, Oxford 300). It is located at *Universidade de Santiago de Compostela* (USC).

2 FESEM ULTRA plus: is a field emission scanning electron microscope operated at 30 kV and equiped with an Energy selective Backscattered detector (EsB®) and an energy dispersive x-ray detector and analytical system (EDX, analytical system INCA, Oxford). This equipment can be operate in scanning tranmission electron microscope STEM mode (Scanning Transmission Electron Microscope). It is located at *Universidade de Santiago de Compostela* (USC).

3 FEG-SEM JEOL 7001-F: is a field emission gun high resolution scanning electron microscope operated at 30 kV and equipped with an energy dispersive x-ray detector and (Si(Li), analytical system INCA 300, Oxford) and a wavelenght dispersive x-ray detector (discryminatory crystals from boron to uranium and flow proportional detectors, analytical system INCA Wave 200, Oxford). It is located at *Universitat Jaume I* (UJI, Castelló).

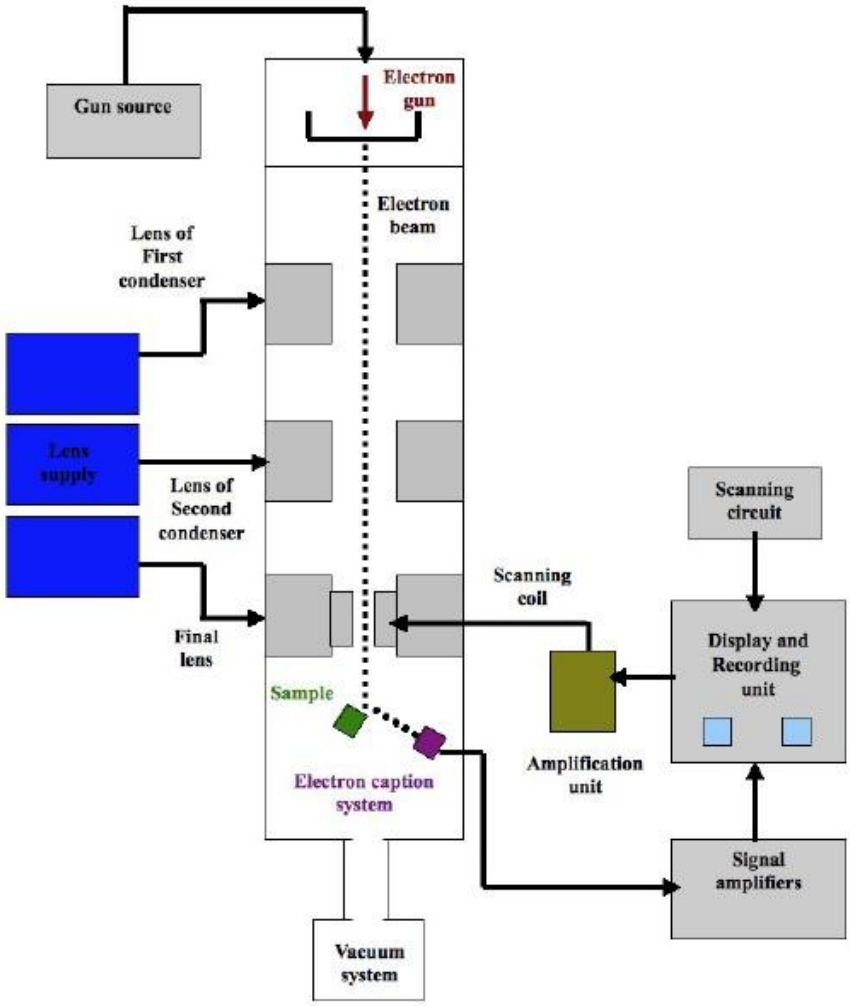

Figura 2.18: Schematic diagram of a SEM instrument with indication of its main components.

2.2.1.6 Transmission Electron Microscopy

The transmission electron microscope (TEM) is an evacuated cylindrical instrument (some about several meters in height) with an illumination system consisting of the electron source (the cathode), the accelerating high voltage unit (100.000 to 300.000 V) and the condenser lens at the top (Fig. 2.19). Therefore, the electrons closely approach the speed of light. The illumination system can produce a spread electron beam or a finely focussed electron probe on the specimen, by tuning the condenser lens [135-137].

Figura 2.19: Photograph of a commercial Transmission Electron Microscope (Philips CM300FEG/ UT-STEM) located in Bonn and used for this study.

The electromagnetic lenses of an electron microscope consits of an electric coil and a soft iron piece with a hole in the centre. The lens system of the transmission electron microscope contains condenser and objective lens elements. These have the equivalent function of convex glass lens elements in conventional optical microscopes. The specimen is mounted into a removable

holder, which is fixed into a goniometer for mechanical shift and tilt operations [135-137].

As the electron beam passes through the specimen, it will interact elastically and inestically with the atoms of the specimen in scattering processes. The most important objective lens forms the first image with the elastically scattered electrons. The intermediate lens is used to control the magnification. The projector lens corresponds to the ocular lens of the light microscope and forms a real image on the fluorecent screen at the base of the microscope column where the image is visible or the image is projected onto a CCD camera. The objective lens aperture removes disturbing electrons scattered to large angles and therefore enhances the image contrast [135-137].

Primary electrons interact with core shell electrons of the atoms (inelastically scattered electrons), remove core electrons and the excited atom will have a transition of outer shell electrons into the partially empty core shell. X-rays are generated by this process carrying chemical elemnt information related to a particular X-ray energy. The X-ray photons are registered on a semiconductor detector, and the counts distributed, according to the photon energy, in a multi-channel analyser. Thus a energy dispersive X-ray spectrum (EDX) is obtained. The chemical elements in a material can be analysed qualitatively and semi-quantitatively using EDX [135-137].

In transmission electron microscopy, adequate preparation of the sample plays a crucial role towards achieving high resolution images. TEM specimens must be electron transparent and representative for the material under study. There are many ways to prepare specimens for TEM. The chosen method will depend on both the type of material and the information one needs to obtain. The most important aspect to bear in mind is that the preparation technique must never affect what one observes or measures. Specimen preparation has thus been a very important step for the task during the stays at the *Institut für Anorganische Chemie* of the University of Bonn (Bonn, Deutschland), because a good specimen is the prerequisite for obtaining useful and representative results in a TEM study [135-140]. For the present studies the samples had to be

prepared in cross-section in order to enable observation of coating-substrate interfaces.

Sample preparation

Samples were selected amongst with optically active layers (frit and sol-gel layers) and LAB derived coatings obtained on the commercial glass substrates (2,5x7x0,5 cm^3) described earlier. For the sample preparation the following equipment was utilized:

- Buehler Isomet diamond disk saw
- Struers Accutom-2 diamond disk saw
- Well-3242 wire saw
- Well-4240 wire saw
- VPG200 polishing plate
- VP200 polishing plate
- Buehler Minimet-1000 polisher
- Gatan Dimple Grinder-656
- Bal-Tec RES010 ion beam thinning system.

First, the sample pieces were reduced in size to dimensions 2.1 x 7.0 x 0.9 mm^3 by cutting with saws. In the LAB samples, the affected part of the substrate was placed at the center position, along the length of the specimen. These specimens were then polished on a semi-automatic polishing plate (VPG200) provided with a SiC PC320 polishing surface disk, on the side of the substrate to a thickness of 0.34 mm.

The confronted face-to-face pieces of the samples were prepared using M-Bond adhesive glue 610A. The pieces were glued together under pressure and heated to 150 ºC for two hours. At this point, the specimen is introduced into an alumina tube and coated with adhesive M-Bond AE-15. Both are introduced into a hollow alumina tube with the glue perfectly cover on the three exposed parts, in order to avoid the formation of bubbles in the glue section. The glue must perfectly cover the three parts to avoid bubbles in the glue. The consolidation of the TEM sample structures is achieved after heat treatment at 100 ºC for two

hours. Such structures provide sufficient sample stability to insure handling during the subsequent processes to be carried out, prior to TEM observation.

The next step is the cutting of the cylindrical piece perpendicular of the cylinder axis, using a Well-3242 wire saw, to obtain disks of about 300 μm in thickness. The disks must be reduced to 100 μm thickness by polishing both faces. This process is realized by a semi-automatic polishing plate, model VP-200 (employing SiC polishing disks P800 and P1200), and subsequently with a Buehler Minimet-1000 automatic polisher, (3 and 6 μm polishing suspensions).

The final mechanical preparation step is the spherical polishing, performed with a Gatan Dimpling Grinder-656, to make a convex dimple in the center of the disk, on both sides. Polishing suspensions mono- (1 and 3 μm) and polycrystalline (¾ μm) diamond particles for frit and solgel coated samples; and mono- (1 and 3 μm) and polycrystalline (¼ μm) diamond pastes for LAB samples.

A final sample preparation step was performed by an ion etching process to obtain a hole in the specimen disk where the hole edges are electron transparent, i.e. The thickness has to be as small as the mean scattering lenght for electrons. This preparation step was carried out in Bal-Tec RES-010 and RES-101 ion etching systems.

This step supposed an important aspect of this research related to the study of waveguides made by laser ablation of metal targets, due to etching and materials incompatibility observed. The ion thinning step is fundamental to reduce the thickness of the samples to electron transparency. Unfortunately, the etching rate for the metal in the waveguide is much higher than for the glass substrate. Thus, using standard conditions, the metal waveguides are destroyed. Soft etching conditions had therefore, to be developed particulary here.

For the first specimens treated, it was observed that in a few seconds, a big hole appeared on the specimen, with the consequent elimination of the zone containing the ablate metal (Fig. 2.20). Furthermore, when a sufficiently small hole was obtained, but the thickness of the material was too large to allow the

pass of the electrons (Fig. 2.21). A wide range of samples was prepared to obtain good specimens for the TEM analysis, applying soft etching process conditions (Fig. 2.22). The size of the holes was observed with a Zeiss Axiotech A620 conventional optical microscope.

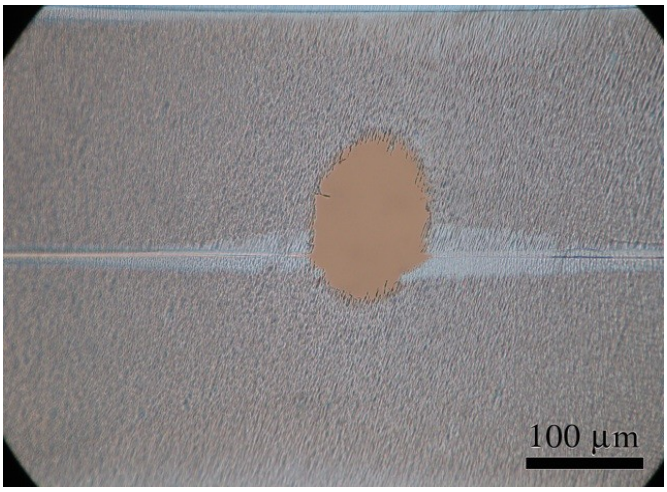

Figure 2.20: Hole made on a LAB sample obtained from an Al target. The wedge shaped edges of the hole are thin enough for the TEM but the big hole indicates that par of the coating has been destroyed.

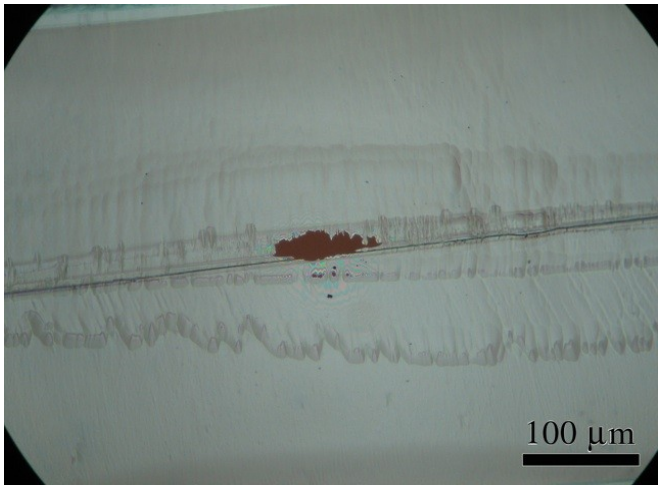

Figure 2.21: Hole made on a LAB sample obtained from an Ag target. In this case, although etching a smaller hole, the thickness is to large for the electrons to pass through.

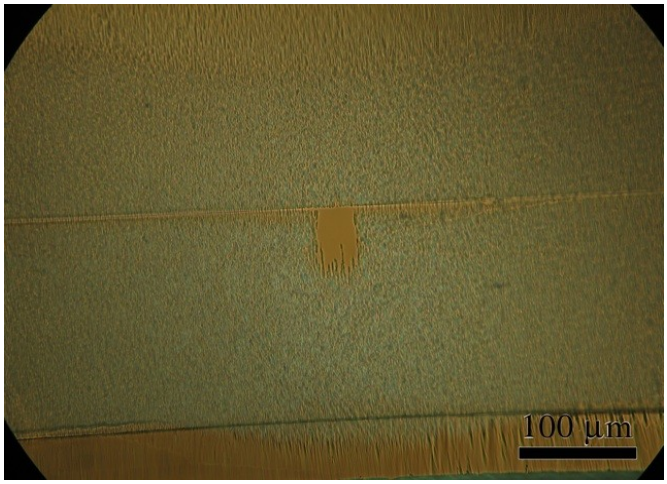

Figure 2.22: Hole made on a LAB sample obtained from a 63Cu37Zn alloy target; the thickness and the smaller hole are convenients for TEM studies.

Sample characterization

Sample characterisation by transmission electron microscopy has been performed employing two different electron microscopes:

- Philips CM300FEG/UT-STEM: transmission electron microscope with field emission gun and ultra twin lens and scanning unit operated at 300 kV and equipped with a energy dispersive x-ray detector (HPGe detector, Noran Inc.) and analytical system (energy dispersive x-ray unit, Noran Inc.). The microscope is dedicated for high-resolution imaging

- Philips CM30ST-TEM: scanning transmission electron microscope operated at 300 kV and equipped with one dispersive x-ray detector (silicon-detector, Thermo Scientific) and analytical system (System Six, Thermo Scientific). This microscope has coupled an energy electron loss spectrometer (PEELS, Gatan). This microscope is dedicated for chemical microanalysis and producing compositional maps.

Preliminary studies resulted in basic differences between the samples; which lead to the use of a specific microscope. With respect to the coated samples; we observed diffusion processes in all samples. In the case of ceramic frit samples we observed diffusion between materials in both directions, but in the case of sol-gel samples we only observed this process in one direction, from the substrate towards to the coating. Thus, the compositonal mapping option in the Philips CM30 ST-TEM microscope, and the option to use the EELS unit, suggests this microscope is adequate for the of both, frit and LAB samples [141-143]. The EELS unit allows us to determine the possible different oxidation states of the species present in the samples studied. On the other hand, the sol-gel samples were studied with the Philips CM300 FEG/UT-STEM microscope [144-147].

2.2.2 Physical characterization

2.2.2.1 Transport properties

2.2.2.1.1 Electrical Conductivity

It is well known that one of the subatomic particles of an atom is the electron. The electrons carry a negative electrostatic charge and under certain conditions can move from atom to atom. The direction of movement between atoms is random unless a force causes the electrons to move in one direction. This directional movement of electrons due to an electromotive force is what is known as electricity [148].

Electrical conductivity (σ) is the property of a metal that measures its ability to conduct the electricity; it is a measure of how well a material accomodates the movement of an electric charge, following Ohm's law, the ratio of the current density to the electric field strength. Its SI (Standard International) unit is the *Siemens per meter* (*S*/m), but conductivity values are often reported as $Ohm^{-1}m^{-1}$ or as percent IACS [149]. IACS is an acronym for International Annealed Copper Standard or the material that as used to make traditional copper wire. The conductivity of the annealed copper (5.8108×10^7 S/m) is defined to be 100% IACS at 20ºC. All other conductivity values are related back to this conductivity of annealed copper. Therefore, Fe with a conductivity value of 1.044×10^7 S/m, has a conductivity of approximately 18% of that of annealed copper and is reported as 18% IACS. An interesting side note is that commercially pure copper products now often have IACS conductivity values greater than 100% because processing techniques have improved since the adoption of the standard in 1913 and more impurities can now be removed from the metal [148].

Conductivity values in S/m can be converted to %IACS by multiplying the conductivity value by 1.7241×10^{-6}. When conductivity values are reported in μS/cm, the conductivity value is multiplied by 172.41 in order to convert to the %IACS value [148].

Electrical conductivity is a very useful property since values are affected by such things as a substance chemical composition, impurities, microstructure and the stress state of the crystalline structures. Therefore, electrical conductivity information can be used for measuring the purity of water, sorting and identification of materials, checking for optimum heat treatment of metals, and inspecting for thermal damage in some materials [148].

Complementary to this property is the electrical resistivity (ρ), which is the reciprocal of the conductivity. It is the opposition of a body or substance to the flow of electrical current through it, resulting in a phenomenon of electrical energy dissipation into heat, and conversion into light or other forms of energy. The amount of resistance depends on the type of material. Materials with low resistivity are good conductors of electricity and materials with high resistivity are good insulators [148].

The SI unit for electrical resistivity is the Ohm meter (Ω m). Resistivity values are more commonly reported in micro ohm centimeters units. As mentioned above resistivity values are simply the reciprocal of conductivity, so conversion between the two is straightforward. For example, a material with 2 μΩ cm of resistivity will have ½ μS/cm of conductivity. Resistivity values in μΩ cm units can be converted to %IACS conductivity values with the following formula:

$$172.41 / \text{resistivity} = \% \text{ IACS} \qquad [2.5]$$

As noted above, electrical conductivity values (and resistivity values) are typically reported at 20ºC. This is done because the conductivity and resistivity of a material is temperature dependant. The conductivity of most materials decreases as temperature increases. Alternately, the resistivity of most material increases with increasing temperature. The amount of change is material dependent, but has been well established in the literature for many elements and engineering materials [148]. The reason for the resistivity to increase as a function of the temperature is that the number of defects in the atomic lattice structure increases with temperature and hampers electron movement. These imperfections include dislocations, vacancies, interstitial defects and impurity

atoms. Additionally, above absolute zero, even the lattice atoms participate in the interference of directional electron movement, as they are not always found at their ideal lattice sites. Thermal energy causes the atoms to vibrate about their equilibrium positions. At any moment in time, many individual lattice atoms will be away from their ideal lattice sites, provoking interference with electron movement [148].

When the temperature coefficient is known, an adjusted resistivity value can be computed using the following formula:

$$\rho_1 = \rho_2 * [1 + a * (T_1 - T_2)] \qquad [2.6]$$

where ρ_1 = Resistivity value ajusted to T_1
ρ_2 = Resistivity value known or measured at temperature T_2
a = Temperature Coefficient
T_1 = Temperature at which resisitivity values need to be known
T_2 = Temperature at which known or measured values were obtained

For example, suppose that resistivity measurements were being made on a hot piece of aluminium. Normally when measuring resistivity or conductivity, the instrument is calibrated using standards that are at the same temperature as the material being measured, and then no correction for temperature will be required. However, if the calibration standard and the rest of the material are at different temperatures, a correction to the measured value must be made. Presume that the instrument was calibrated at 20ºC but the measurement was made at 25ºC and the resisitivity value obtained was 2.706×10^{-8} Ω m (ρ_2). Using the equation [2.6] and the following temperature coefficient value (0.0043/ºC), the resistivity value corrected for temperature can be calculated; $\rho_1 = 2.648 \times 10^{-8}$ Ω m [148].

Note that the resistivity value was adjusted downward since this example involved calculating the resistivity for a lower temperature.

Since conductivity is simply the inverse of resisitivity, the temperature coefficient is the same for conductivity and the equation requires only slight modification. The equation becomes:

$$\sigma_1 = \sigma_2 / [1 + a(T_1 - T_2)] \qquad [2.7]$$

where: σ_1 = Conductivity value adjusted to T_1

σ_2 = Conductivity value known or measured at temperature T_2

a = Temperature Coefficient

T_1 = Temperature at which conductivity values need to be known

T_2 = Temperature at which known or measured values were obtained

In this example let's consider the same Al alloy with a temperature coefficient of 0.0043/ºC and a conductivity of 63%IACS at 25ºC. Using the equation 2.7 at 20ºC, the conductivity value corrected for temperature can be calculated; σ_1 = 65.0%IACS [148].

The temperature coefficient for a few metallic elements is shown in Table XII [148].

Table XII: Temperature Coefficients of some elements.

Material	**Temperature Coefficient ($^oC^{-1}$)**
Nickel	0.0059
Iron	0.0060
Tungsten	0.0044
Aluminium	0.0043
Copper	0.0040
Silver	0.0038
Platinum	0.0038
Gold	0.0037
Zinc	0.0038

We can experimentally measure these properties applying the four-probe test for electrical resistance measurements (Fig. 2.23-2.25) [149]. Current is fed through the outer leads, and the voltage drop is measured on the inner leads. In this way the contact potential drop experienced by the applied current is localized at the junctions with the outer leads. Measuring V with minimal current through the voltmeter minimizes the contact potential contribution to the measured conductance (G),

$$G = I * V \qquad [2.8]$$

The conductivity σ is an intrinsic property of a pure material, related to the measured conductance (Eq. 2.8) via

$$G = \sigma * A / L \qquad [2.9]$$

just as resistance relates to resistivity (ρ) via

$$R = \rho * L / A \qquad [2.10]$$

Thus a large-gauge conductor [large area (A)] of short length has a high conductance, but the physical dimensions do not affect the conductivity σ nor the resisitivity ρ. Positive current flows from higher to lower voltage, and σ is never negative [149].

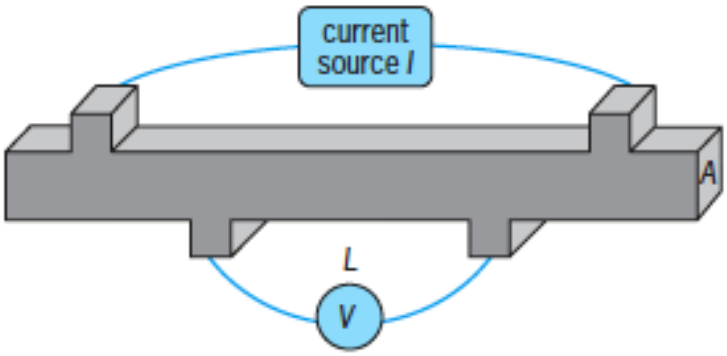

Figure 2.23: Schematic of a four-probe measurement of electrical conductivity [149].

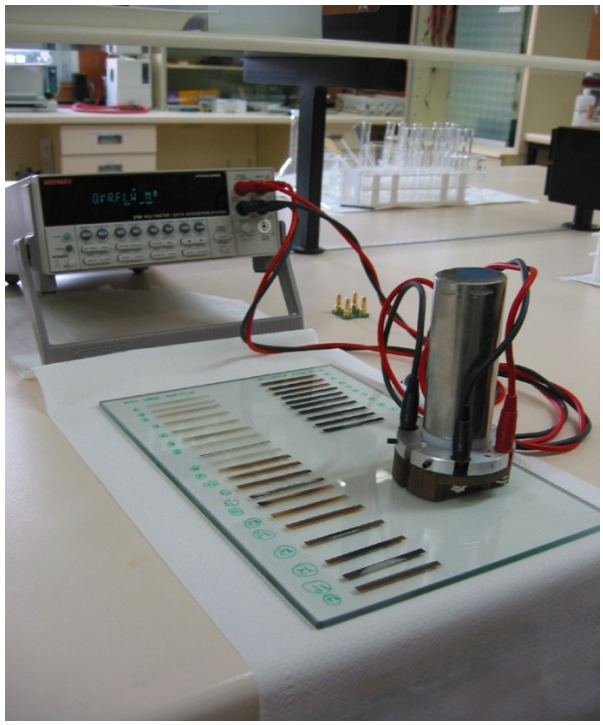

Figure 2.24: Experimental set-up used to measure the electrical resistance of the metallic coatings [courtesy of L.A. Angurel at Instituto de Ciencia de Materiales de Aragón, ICMA-CSIC].

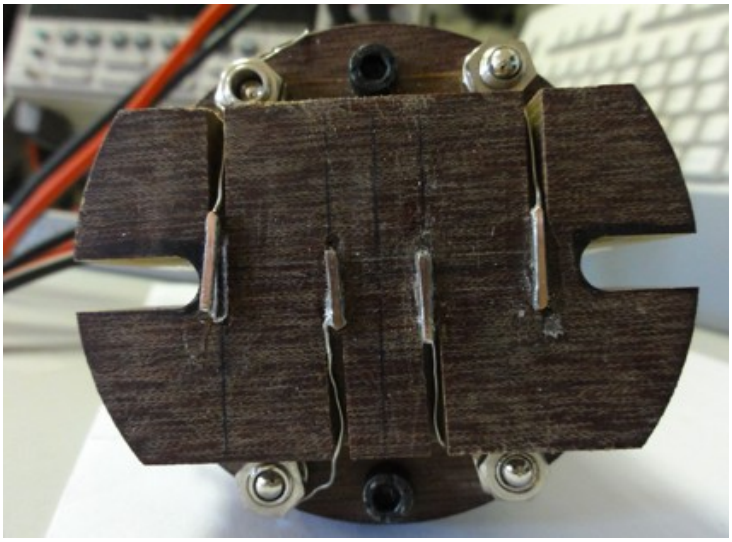

Figure 2.25: Specifically built four-point resistance probe for electrical resistance measurements [courtesy of L.A. Angurel at Instituto de Ciencia de Materiales de Aragón, ICMA-CSIC].

2.2.2.2 Optical properties

As it was already commented in the introduction, the purpose of research is the fundamental study, design, fabrication and characterisation of photonic structures and devices for spatial optics. Until now we have explored new technologies for manufacturing structures, always searching for easily repeatable processes and products of well-defined characteristics and low cost.

The GRIN Optics Group from the University of Santiago de Compostela has working for many years in the development and fabrication of waveguides at the laboratory scale, as well as in their study, both from theoretical as and experimental points of view [29-30]. Experience thus dictated how to optically characterise the LAB and frit samples obtained. The need to use alternative characterisation methods required an intensive collaboration with the *Istituto de Fisica Applicata "Nello Carrara"* (IFAC-CNR) of Firenze. In addition, development of Sol-Gel methods and physico-chemical characterisation

(thickness and refractive index of thin coatings) was performed in collaboration with the *Instituto de Cerámica y Vidrio* (ICV-CSIC).

Thus, the most adequate techniques were selected to characterize the refractive indices, the coating thicknesses and the guiding efficiency (loss measurements) of the different kind of samples prepared by the synthesis methods reported in this dissertation.

2.2.2.2.1 Refractive index

The basic properties of the guiding devices are determined by the distribution of the refractive index within the medium. It is a requirement of the guiding elements that the refraction index value at the core is larger than in the adjacent layers. Therefore, we need an optimal characterisation of this parameter to understand its influence and its dependence on the different experimental settings.

The method for obtaining good measures and determining the refractive index changes depends on the type of guide studied. Thus, three different methods were employed.

2.2.2.2.1.1 Refracted Near-Field Technique

There are different methods for measuring the refractive index, but we have chosen the refracted near-field technique (RNF) in the case of frits coatings because of their large thickness values. Among its many advantages: it allows achieving a high resolution and accuracy, simple interpretation of results and obtaining two-dimensional index profiles. Moreover, the requirements in time to prepare the sample for the measure are minimal [29].

The determination of the refractive index with this technique is based on measuring the intensity of the light refracted in different ways, some of which have a known refractive index [29]. Fig. 2.26 shows a scheme of the elements required for an adequate experimental setup. The beam first passes through a

sectored obstacle that allows us to remove the marginal beams, whose presence is not desirable. Then, we have to couple the light into the waveguide. For this purpose, a microscope objective, whose numerical aperture must be larger than the guide to study, is used to focus the light onto the surface of interest. The substrate that contains the waveguide is located over a block of glass with known refractive index, depositing between them a layer of index matching liquid. In this situation, some light is guided while the rest spreads across the glass block, forming a cone with a central hole. The most intense part of this cone contains evanescent modes (light which traveled a certain distance into the tab, and then exits), while the outside has purely refracted light. The RNF technique is based on the analysis of the refracted light, since the presence of evanescent modes varies importantly from one to another and its contribution is difficult to evaluate. Therefore, an opaque disk that blocks these modes is introduced. Finally, a series of lenses collect the light focusing it over a power detector.

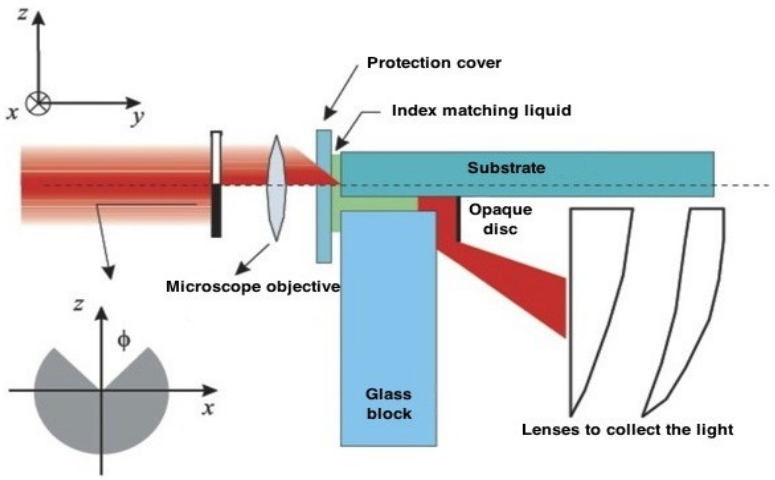

Figure 2.26: Scheme of experimental configuration used to measure the refractive index by the refracted near-field technique [90].

Considering the change of the inducted refractive index on the irradiated area is $\Delta n(r)$, we can define the guide's index as:

$$n(r)=n_s+\Delta n(r) \qquad [2.11]$$

where n_s is the refractive index of the substrate. Assuming that the index change is small, it can be shown that the power which passes trough the disc (P(q)) is proportional to the refractive index at the point of incidence [150], expressed as:

$$P(q)=a_1-a_2 n(r) \qquad [2.12]$$

where a_1 and a_2 are constants that depend on the experimental conditions, and whose value is determined through a calibration process. In this process, power values are provided by the detector when the light that passes through the glass block and the index matching liquid are used. The values of the refractive index of the glass block and the index matching liquid are previously known.

The experimental setup used is shown in Fig. 2.26. To perform the measurement of the refractive index we employed the beam from a He-Ne laser (λ=632.8 nm). In a first step, the beam is collimated by a series of lenses and diaphragms. After passing through these elements, the expanded beam is cut by one shutter (sectored obstacle) to remove the diffraction rings and achieve a more homogeneous beam to perform of refractive index measurements. As noted previously, the laser beam is focused through a microscope objective on the sample surface. The waveguide is placed over a glass block, depositing an index matching liquid layer between both. As can be seen in Fig. 2.27, the waveguide is located on two motorized platforms (Spindler & Hoyer model LT 100 ST), which allow the displacement of the sample in the xyz directions, as shown in the diagram of Fig. 2.26. The light, previously cut by an opaque disc, is collected by a set of lenses and focused on the power detector (Scientech Astral model AA30) that measures the output beam power from the setup.

The indices of the glass block and the index matching liquid are used to calibrate the device. In our case, the glass block is made of borosilicate whose refractive index is n=1.470 for a wavelength of 632.8 nm. On the other hand, the index matching liquid specifications show a value of n_D=1.450±0.0002 for the sodium D line (λ=589.3 nm) at a temperature of 20ºC. These index values are corrected for the wavelength of the laser used (He-Ne, 632.8 nm), for which we

performed an interpolation using values specified by the manufacturer (values n_C and n_F). The objective is to obtain a profile similar to that shown in Fig. 2.28, which corresponds to the refractive index of lead borosilicate frit layer deposited onto a commercial glass substrate. Thus, we obtained a value of 1.58 for the refractive index at a wavelength of 632.8 nm.

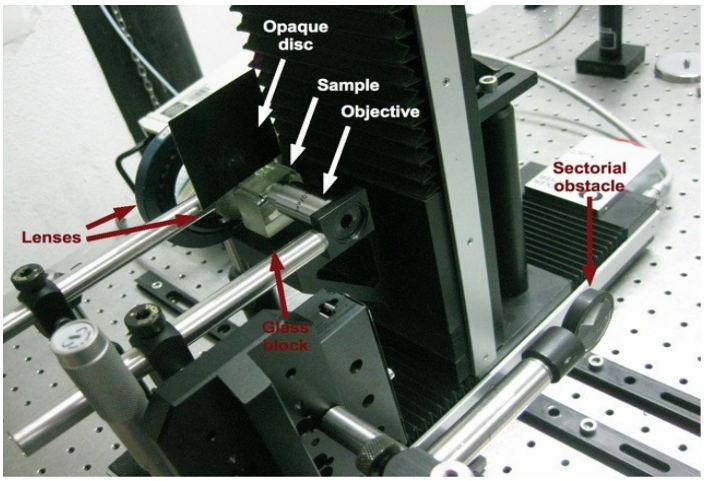

Figure 2.27: Experimental apparatus for RNF technique.

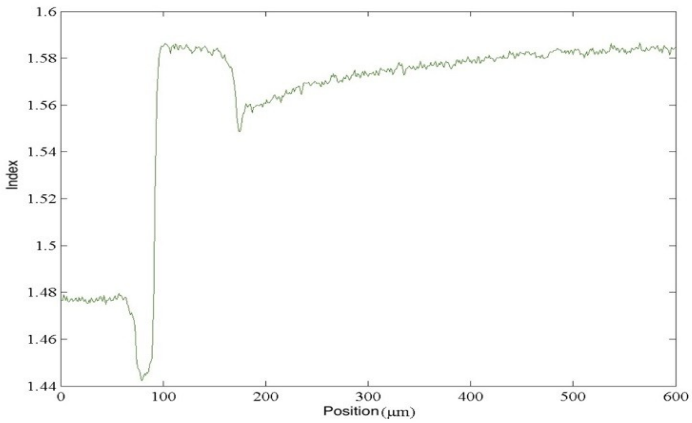

Figure 2.28: Graphic of the refractive index profile measured for a representative lead borosilicate frit sample.

2.2.2.2.1.2 Variable Angle Ellipsometry

Spectral ellipsometry is an effective method for determining the optical constants and thicknesses of thin films and layer systems; this technique was applied using a Woollan M2000U spectral ellipsometer (J.A. Woollan Co.) at the *Instituto de Cerámica y Vidrio-CSIC* (Fig. 2.29) for the characterisation of samples prepared by Sol-Gel. The detection sensitivity of the method is very high and, theoretically, it allows determination of the thicknesses of thin and thick films. Handling of the samples is very easy and the method, as in the previous case, is contact-free and non-destructive. Measurement of the polarisation state of the reflected light is used to determine the film thickness and the optical constants of the samples under study. The spectral ellipsometry measurements were carried out here in the ultraviolet/visible region, but measurements in the infrared region have been widely reported in the literature [151-152].

Ellipsometry is an optical measurement technique that characterizes light reflection (or transmission) from samples. The key feature of ellipsometry is that it measures the change in polarized light upon light reflection on a sample (or light transmission by a sample). The name 'ellipsometry' comes from the fact that polarized light often becomes 'elliptical' upon reflection of the surface. The measured values are expressed as Ψ and Δ (Fig. 2.30). These represent the amplitude ratio Ψ and phase difference Δ between waves known as p- and s-polarized light waves. In ellipsometry, therefore, the variation of light reflection with p- and s-polarizations is measured as the change in polarization state. In particular, when a sample structure is simple, the amplitude ratio Ψ is characterized by the refractive index n, while Δ represents light absorption described by the extinction coefficient k. In this case, the two values (n, k) can be determined directly from the two ellipsometry parameters (Ψ, Δ) applying the Fresnel reflection coefficients [153].

Figure 2.29: Image of the spectral Woollan M2000U ellipsometer used in this work for the characterisation of Sol-Gel films.

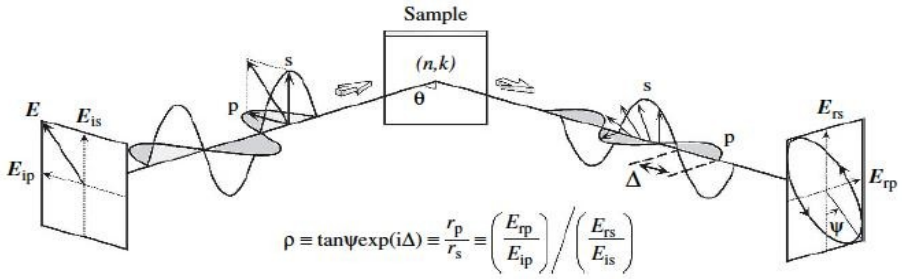

Figure 2.30: Illustrative diagram representing the measurement principles of ellipsometry.

Figure 2.31 shows the coordinate system used to describe the ellipse of polarization is the p-s coordinate system. The s-direction is taken to be perpendicular to the direction of propagation and parallel to the sample surface. The p-direction is taken to be perpendicular to the direction of propagation and contained in the plane of incidence [153].

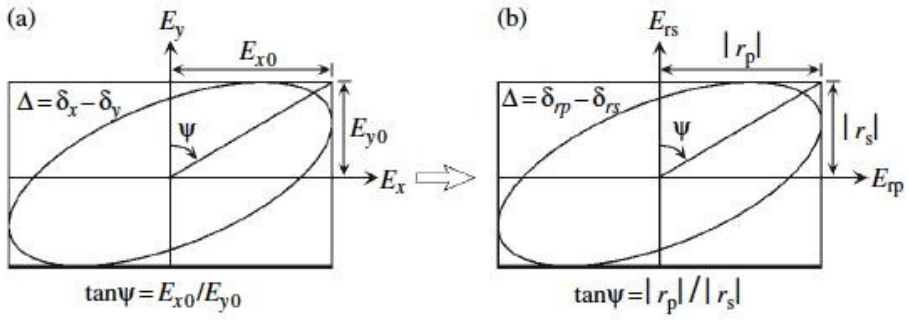

Figure 2.31: Coordinate transformation from (a) the (E_x, E_y) coordinates to (b) the (E_{rp}, E_{rs}) coordinates.

The optical constants define how light interacts with a material. The complex refractive index is a representation of the optical constants of a material, it is represented by;

$$\check{n} = n + ik \qquad [2.13]$$

the real part or index of refraction, n, defines the phase velocity of light in a material:

$$v = c / n \qquad [2.14]$$

where v is the speed of the light through the material and c is the speed of the light in vacuum. The imaginary part or extinction coefficient, k, determines how fast the amplitude of the wave decreases. The extinction coefficient is directly related to the absorption of a material and related to its absorption coefficient by :

$$\alpha = [4\pi k] / \lambda \qquad [2.15]$$

where α is the absorption coefficient, k is the wavenumber and λ is the wavelength of light. Because ellipsometry measures the ratio of the two values, it can be highly accurate and very reproducible [154].

In order to achieve high accuracy and for testing unknown layer systems, measurements can be combined across the entire spectrum at several angles of incidence. For known samples, a few specific wavelengths and angles of incidence can be selected in order to carry out routine measurements within a short time. The data values obtained for Ψ and Δ allows building a mathematical model through which values for thickness and refractive index may be estimated.

2.2.2.2.1.3 Dark M-line Spectroscopy (The Mode theory)

Before explaining Dark M-line Spectroscopy we must describe the Mode Theory to understand the existence of guiding modes at the waveguides. The Mode theory, along with the Ray theory, describes the propagation of light along an optical fiber. It can thus be extrapolated to planar waveguides. Mode theory is used to describe the properties of light that Ray theory is unable to explain. The Mode theory uses electromagnetic wave behavior to describe the propagation of light along a fiber. A set of guided electromagnetic waves is defined as a mode of the fiber [155-156]. Fig. 2.32 shows the electric transverse mode or TE mode, and the magnetic transverse mode or TM. The TE mode has the magnetic field in the xz plane and the electric field perpendicular to the same. In the case of the TM modes, the electric field is in the xz plane and has the magnetic field perpendicular to this plane. The components of these fields for each mode are [9]:

TE mode: $\mathbf{E}$ $(0, E_y, 0)$, $\mathbf{H}$ $(H_x, 0, H_z)$

TM mode: $\mathbf{E}$ $(E_x, 0, E_z)$, $\mathbf{H}$ $(0, H_y, 0)$

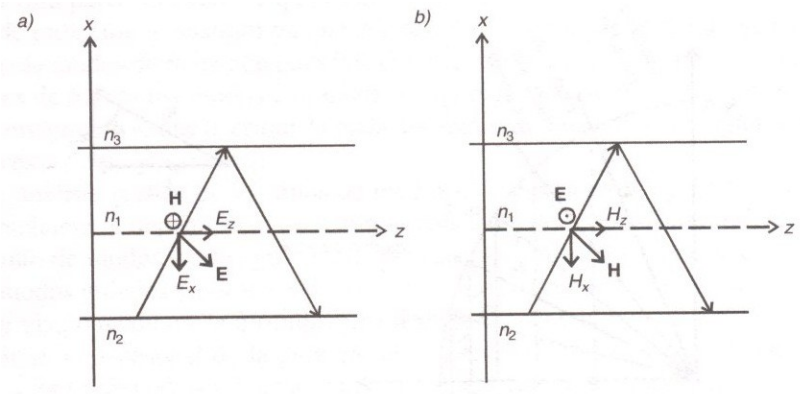

Figure 2.32: Kinds of modes in a planar waveguide: a) *TM* and b) *TE* [9].

Dark m-line spectroscopy is a widely used technique for the characterization of planar optical waveguides, oppening access to the main waveguide parameters, i.e. waveguide thickness and refractive index [10, 56, 157-158]. It allows fast characterization without any sample preparation, such as end-face polishing. This technique is based on a prism coupling, and the measurement is made on a small waveguide region, allowing to test for homogeinity and/or to work with intermediate quality samples during waveguide fabrication optimization. The m-line measurement does not cause any damage, allowing further sample processing. Automated m-line systems have been commercially available for several years [56, 159].

M-line spectroscopy was developed in the seventies by Tien et al. [160] and Ulrich [161]. They complete the experimental observation of waveguide modes in semiconductor thin films [160] by the theoretical treatment [161] of a prism coupler using a plain wave approach [56]. Later, this theory was extended to non linear distributed couplers, allowing to simulate dynamical and non linear effects in prism and grating couplers [159]. The literature consulted reports several papers employing this technique for the optical characterisation of sol-gel waveguides [56, 111, 157-158, 162].

This technique was used here for the investigation of the TE and TM modes on sol-gel samples and the subsequent calculation of the refractive indices by

mathematical methods. We used the COMPASSO instrument, which is a spectrometer developed by the IFAC research center. The equipment consists of a set of laser sources operating at different wavelengths. The laser beam strikes on an isosceles prism placed in contact with the sample (optical contact is achieved applying pressure). The prism/waveguide set is placed onto a rotational stage. The light reflected at the prism waveguide interface (by total internal reflection) is recorded by a photodiode. At certain angles, when the modes of the waveguide are coupled, a depth on the intensity of the reflected light signal, which is monitored by a photodiode, is detected. The basic scheme of the equipment is shown in Fig. 2.33. The apparatus is controlled by a computer with dedicated software. Two lasers are available with wavelengths of 635 nm and 1550 nm, as well as three different prisms, named SF-14, GGG and rutile, which allow measuring the refractive index between 1.45 and 1.6, between 1.5 and 1.9 and between 1.9 and 2.4, respectively. The thickness and the effective refractive index of each waveguide are calculated after a mathematical analysis of the data based on the WKB method [56]. This is a mathematical method for finding approximate solutions to linear partial differential equations with spatially varying coefficients. Before the measurements, the surface of the sample was cleaned with ethanol using a cotton tissue.

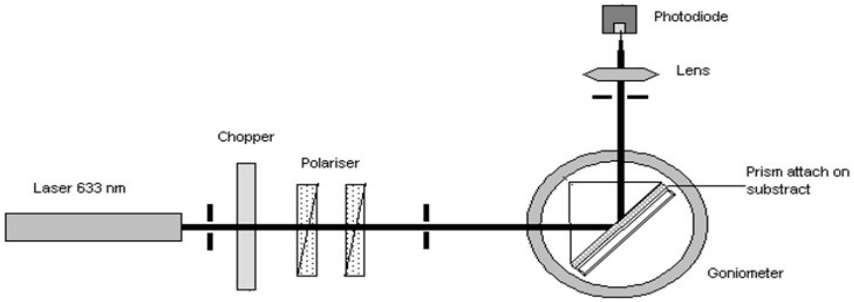

Figure 2.33: Scheme of Dark m-line spectrometer [56]. One laser of wavelength 633 nm is represented in this scheme; however, the laser and its wavelength can be changed.

2.2.2.2.2 Loss measurements

As we have described previously, different types of samples were structurally and optically characterised through different appropriate methods. In the case of loss measurements, we have again different options, each one more appropiate for a given kind of sample. Thus, this reasearch step requires choosing specific method depending on the coupling technique or the thickness of the guiding layer. Moreover, the study of the waveguide efficiency is complex in itself, as demonstrated in the literature [10, 155-156].

An established form to express the efficiency of the guiding process is based on the measurement of losses through the attenuation coefficient, α [dB/cm]. This coefficient is easily calculated through the equation:

$$dB = 10\log (P_0 / P_i) \qquad [2.16]$$

where P_0 is the waveguide output power and P_i the laser source emission or waveguide input power.

2.2.2.2.2.1 Direct Coupling Method

This is the simplest arrangement which we have constructed for the loss measurements. Input and output powers were measured using a Uniphase 1508-0 potentiometer and a He-Ne laser coupled to the guiding layer with a 40x and numerical aperture (NA) 0.6 microscope objective (Fig. 2.34). This method was employed to characterize the guides made by LZM. The samples must be previously polished at the two faces to obtain sufficient optical quality to allow efficient coupling of the light.

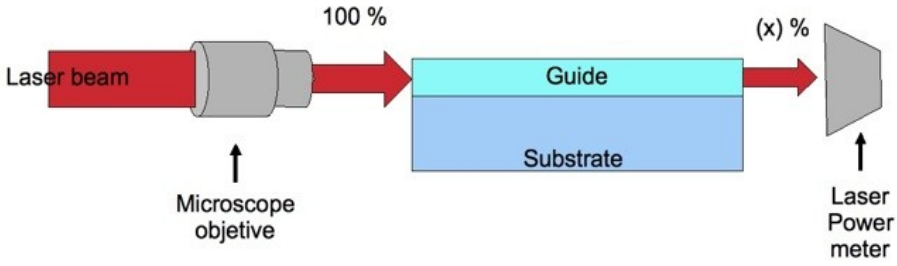

Figura 2.34: Experimental configuration of laser power measurements by a direct-coupling method.

2.2.2.2.2.2 Direct Butt-coupling Method

The butt-coupling method consists in the direct coupling of an optical fiber to the waveguide. The fiber is coupled to the light source, which in this case is a 635nm wavelength laser. Microscope objective is positioned at the output of the waveguide to image the waveguide output face onto a screen (Fig. 2.35).

This method was applied to waveguides obtained by LAB, which were previously polished to obtain the best optical quality for the coupling. A laser powermeter is used to measure the waveguide power input and the output.

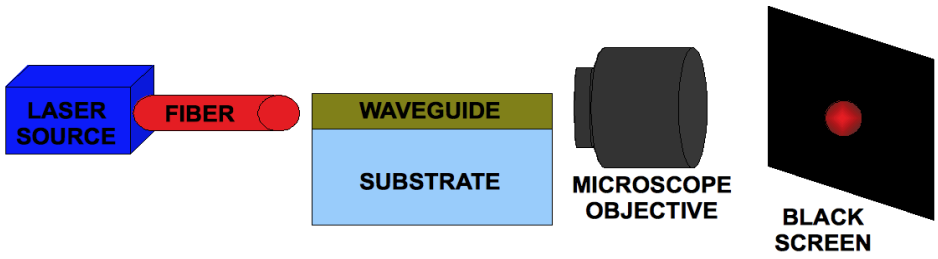

Figure 2.35: Illustrative scheme of the butt-coupling method.

2.2.2.2.2.3 Double Prism Method

The thick SiCe waveguides produced via the sol-gel method described earlier were studied by the double prism method to measure their losses (Fig. 2.36). However, this method supposes the existence of coupling losses at the input and at the output prism, so that only approximate waveguide efficiency values may be determined. Rectangular prisms were used to make measurements with this method [156, 160-161, 163].

The beam of a He-Ne laser emitting at 633 nm with a nominal power of 35 mW was introduced into prism by focusing it through a microscope objective (40x, NA 0.6). The input angle into the prism (n=1.779, NSFL-11, Edmund Optics) is defined mathematically using Snell's law, resulting a value of 1º42' respect to the normal of the hypotenuse of the entering prism. A second prism was placed 2 cm away. Coupling between the prisms and the waveguide was achieved with a refractive index matching liquid (n=1.561 and λ=310 nm, Cargille Labs.). A laser power meter (Beam Profiler, Thorlabs GmbH) was used to measure the input and output laser beam power (Fig. 2.37).

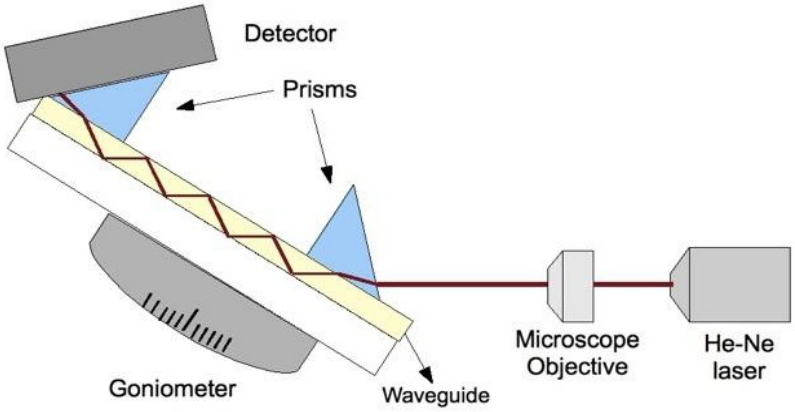

Figure 2.36: Schematic drawing of the experimental double-prism set-up.

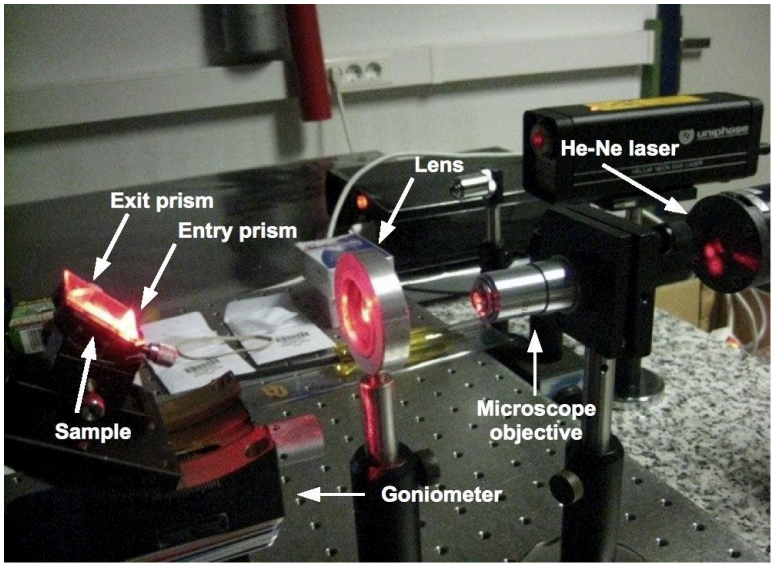

Figure 2.37: Experimental double-prism set-up for loss measurements of thick sol-gel waveguides.

2.2.2.2.2.4 Method based on Scattered Light

Among the different ways to obtain the propagation losses which are reported in the literature [163-165] we took the method developed by the IFAC group to evaluate losses in waveguides obtained via sol-gel [56]. The measure of the waveguide propagation losses is instead obtained by an image caption device, specifically a vidicon camera (Hamamatsu) which collects the light scattered out of the plane of the film (Fig. 2.38). Scattered light is assumed to be proportional to the guided light I, which propagates according to equation:

$$I=I_0 e^{-\alpha d} \qquad [2.17]$$

where I_0, is the input intensity, α is the attenuation coeficient and d is the propagation distance.

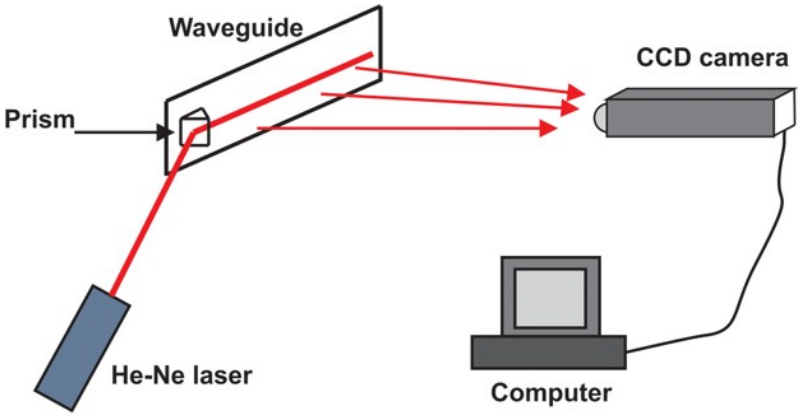

Figure 2.38: Waveguide loss measurement set-up developed at IFAC [56].

The decay curve of scattered light along the propagation length can be fitted by an exponential curve to calculate the attenuation coefficient. Before the measurements, the surface of the sample was cleaned with ethanol using a cotton tissue.

Chapter 3

RESULTS and DISCUSSION

3.1 Sol-Gel method

Planar slab waveguides coated commercial glass substrates were obtained by the Sol-Gel method. These coatings were firstly characterized by ellipsometry at the *Instituto de Cerámica y Vidrio* (ICV-CSIC, Madrid). Table XIII summarizes different representative coatings prepared and shows their critical thicknesses and refractive indices. The critical thickness refers to the maximum thickness attainable by dip-coating without film breakdown.

An important microstructural factor related to losses by geometry is the surface roughness. To study this parameter on Sol-Gel samples we used the confocal microscopy at the *Insituto de Ciencia de Materiales de Aragón* (ICMA-CSIC, Zaragoza). In particular, we studied the surface roughness of SiTi (70:30) and ZrCe (70:30) monolayers. The observation in detail of the surface layer from a Sol-Gel sample through confocal microscopy allowed us to check the homogeneity of the surface in extensive areas (Fig. 3.1). This low roughness was measured and is represented in Table XIV.

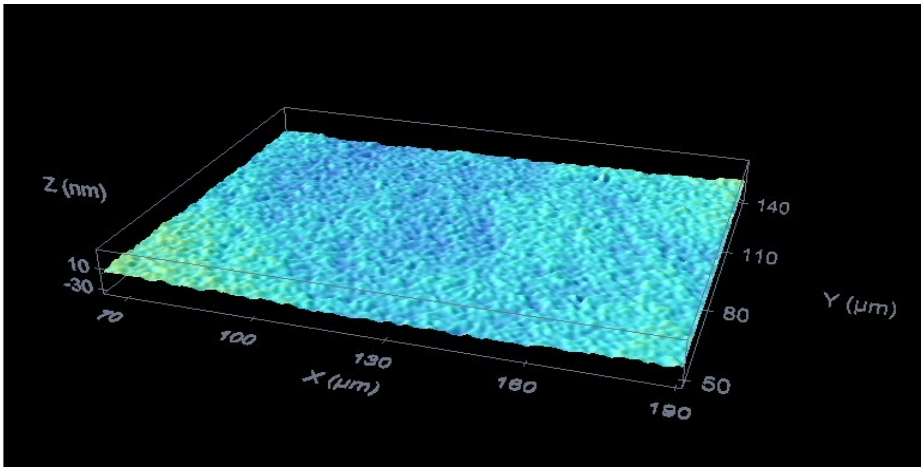

Figura 3.1: Surface topography of the ZrCe (70:30) sample obtained by confocal microscopy.

Table XIII: Refractive index (λ=633nm) and critical thickness values for the different Sol-Gel coatings prepared. (a) internal coating adjacent to substrate (b) intermediate coating (c) external coating.

System		***Molar composition***	***Refractive index***	***Thickness (nm)***
Single layers				
SiTi		90:10	1.45	1100
		80:20	1.51	400
		70:30	1.63	360
		50:50	1.73	140
ZrCe		90:10	1.98	150
		70:30	1.99	200
SiZrC		75:25	1.53	210
SiZr		65:25:10	1.59	220
SiCe		95:5	1.47	2330
Multilayers				
SiTi		70:30	1.59	1230
SiTi		50:50	1.75	610
ZrCe		70:30	2.04	490
Sandwiches				
#1	ZrCe (a)	70:30	2.04	130
	SiTi (b)	70:30	1.62	350
	ZrCe (c)	70:30	2.04	130
#2	ZrCe (a)	70:30	1.04	130
	SiTi (b)	70:30	1.62	350
	SiTi (c)	50:50	1.73	140

Table XIV: Roughness average values tested for Sol-Gel compositions.

Sample	**Roughness average (nm)**
SiO2:TiO2 (70:30) monolayer	5.7
ZrO2:CeO2 (70:30) monolayer	7.2

The third type of studies carried out on this kind of waveguides were related to their microstructural, and were particulary focused on the coating-substrate interfaces, observed by Transmission Electron Microscopy at the *Institut für Anorganische Chemie der Universität Bonn* (Bonn, Deustchland).

The study of the SiO_2:TiO_2 (70:30) sample was the first performed for Sol-Gel samples by transmission electron microscopy. Fig. 3.2 shows a micrograph corresponding to a representative SiTi sample, where no discontinuities arising from cracks or mismatches were observed between both phases, identified clearly in the micrograph. A darker contrast zone is observed in the area of the coating approaching the substrate, consistent with the presence of heavier atomic weight elements, such as Ti, within it. An excellent adherence between the SiTi Sol-Gel coating and the commercial, soda-lime glass substrate, may be deduced from this micrograph, as no cracks or apparent mismatches with accumulation of defects or large impurities are observed at the interface. In addition, a well-defined coating layer is observed which, combined with the precisely defined interface geometry, should result in a good light guiding behavior.

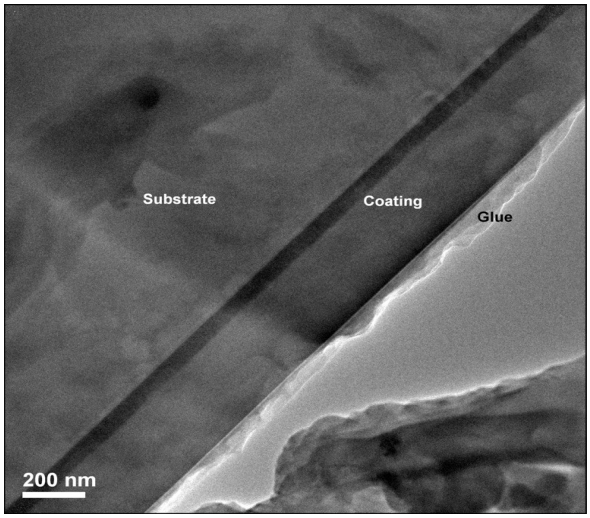

Figure 3.2: TEM image (CM300) of a polished SiTi sample interface area near the substrate. The interface is well-defined by a dark contrast line within the film, which corresponds to a higher content of higher atomic weight species and Ti.

A diffusion process involving alkalis and alkaline-earth species is confirmed in the micrograph of Fig. 3.3, where observation is made under higher magnification and complemented with EDX analysis. This figure suggests that Na, K and Ca ions have migrated from the glass substrate toward the Sol-Gel coating, as recently explained in the literature by Sunder et al [166]. These authors claim that diffusion of the species within Sol-Gel coated silicate glasses are independent of the preparation method, and are influenced by the presence of reducing atmospheres during the heat treatment, as expected here during decomposition of the organic moieties present within the original sol-gel coating. In contrast, the Ti concentration in the proximity of the interface area is found to be higher than at the external part of the coating, and its presence, as expected, is not detected within the substrate. The concentration of alkali and alkaline earth atoms is higher within the darker contrast area than within the rest of the coating. The substrate area adjacent to the coating (near the substrate-coating interface) has thus become, with respect to the rest of the substrate, enriched with Si. This is consistent with the fact that it appears with lighter contrast, as expected for the lower atomic weight of Si with respect to K and Ca. The associated alkali and alkaline-earth metal cation diffusion process is thus held responsible for the excellent chemical matching between the coating and the substrate materials, deduced from the interface observed and the EDS spectra given in Fig. 3.3.

Moreover, crystalline phases have not been observed within the coatings, which confirmed to posses an amorphous character. This is further supported by X-ray difraction, where no diffraction maxima appear. Light guiding may therefore not arise from the presence of crystalline phases, nor nanoparticles present within the guiding medium. It may rather occur because of the intrinsically higher index of refraction of the Sol-Gel coating, as compared to that of the substrate and air, which limits the surfaces of the coating not in contact with the substrate. This is the reason for having a slab waveguide here. Previous theoretical studies have established the development of multilayer structures in order to obtain waveguides with sufficient thickness to conveniently achieve light guiding [section 2.1.1]. Following such study, multilayer silica-titania (SiTi-M) coatings were thus prepared in this work by stacking up to 5 single layers in subsequent deposition and drying steps over

similar glass substrates with the aim of carrying out microstructure characterization and light guiding efficiency studies [Table XIII].

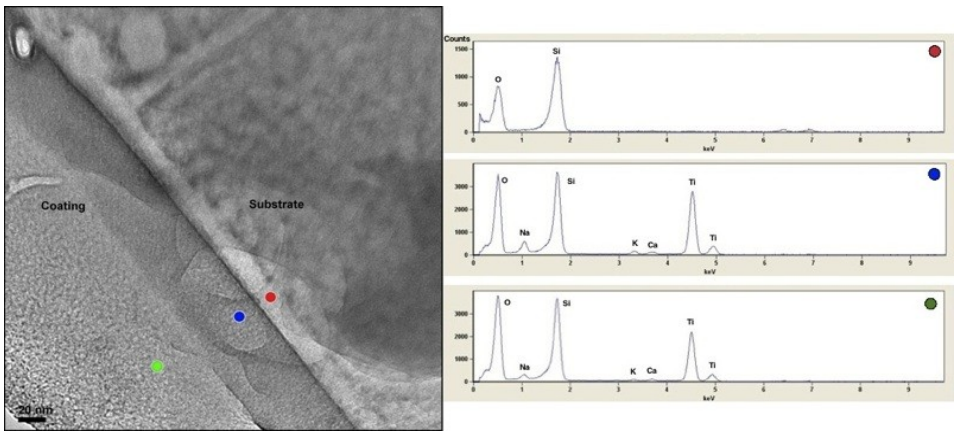

Figure 3.3: TEM (CM300) image (left) corresponding to a close-up view of the substrate-coating interface region of the SiTi sample; EDS spectra (right) obtained at the marked, colored points within the substrate near the interface (red), coating near the interface (blue) and coating away from the interface (green). The substrate (red, top spectrum) appears without Ti and depleted of alkalis and alkaline-earths, which are abundant in the coating layer near the interface (blue, center). Further away from the interface, the coating still contains Na, K and Ca, with much lower relative amounts.

Figure 3.4 shows a micrograph of a polished cross section corresponding to a five-layer SiTi-M coating sample thus obtained. The successively stacked layers are easily identified, as they are separated by a clean interface. The influence of the drying step may be intuitively deduced by observing the areas between layers 1-2 and 2-3, where defficient drying results in the appearance of air bubbles near these layer interface areas. The presence of bubbles was not observed in the upper layers, however, since the drying procedure applied after each dip-coating step seems sufficient to remove bubbles from the outermost layers. The study of the interfaces between these layers allow us to check the homogeinity and continuity between layers, as demonstrated in Figures 3.5 and 3.6, where a close-up look at the interfaces between layers 2-3 and 3-4-5 are shown. These micrographs exhibit interfaces which appear to be clean,

suggesting that coupling between amorphous layers takes place at the atomic level, apparently with no significant structural perturbations. No-long range structural order is observed, however, even at the highest magnification, as exemplified by the micrograph exhibited in Fig. 3.5. This result suggests that it would be possible to prepare a single, homogeneous thick layer from the successive stacking of several thinner SiTi layers (Figs. 3.5-3.6).

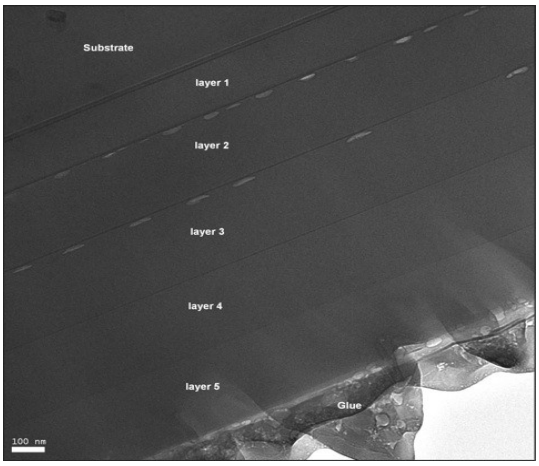

Figure 3.4: TEM image (CM300) of the multilayer SiO_2:TiO_2 sample. Well-defined interfaces are observed between the substrate and the first SG layer, although a dark-contrast interlayer appears within this region due to diffusion of alkali and alkaline-earth species from the substrate towards the coating, as discussed in the text. Porosity is observed near the interfaces of layers 1-2 and 2-3, arising most likely from an innapropiate drying procedure during the sol-gel process.

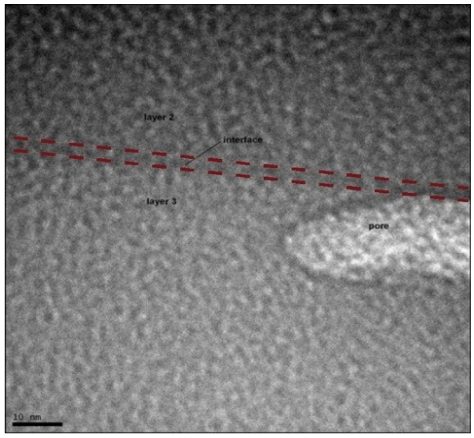

Figure 3.5: TEM image (CM300) of the interface between layers 2 and 3 in the cross section of a polished and thinned SiTi-M sample. The interface is highlighted by two dim lines, and it is observed to be a uniform match between layers 2 and 3, as if were a continuous material. A pore, caused presumably by an innapropiate drying procedure, is observed on the right side of the micrograph.

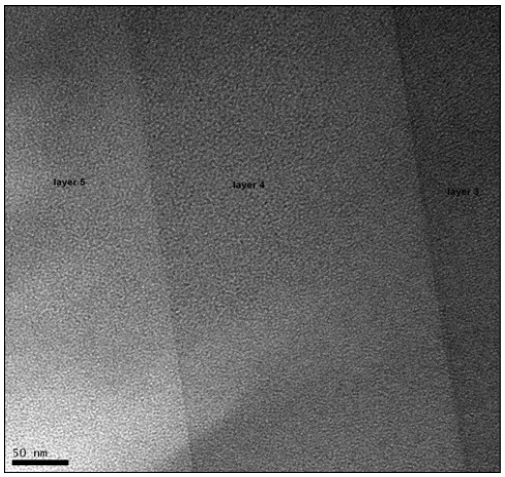

Figure 3.6: TEM image (CM300) of layers 3 to 5 viewed in the polished and thinned cross section of sample SiTi-M. Well defined interfaces are observed between each sol-gel layer, although no long-range structural order, nor structural mismatches are identified within these regions. These layers appear to be very similar between them, as if they made up a continuous single layer. The different contrasts observed, lighter grey as the layer moves away from the substrate, are due to the progressive thinning of the sample, not to a difference in composition.

The interface between the first layer of the coating and the substrate that is shown in Figure 3.7, however, is considerably more diffuse than appears in the SiTi single layer sample of Figures 3.2 and 3.3. Such a difference is assigned to arise from the successive heat treatments performed on the multilayer sample. This suggests that, in the fabrication of multilayer coatings, only a single step, longer heat treatment should be carried out after an adequate drying step, as opposed to multiple drying and heating steps.

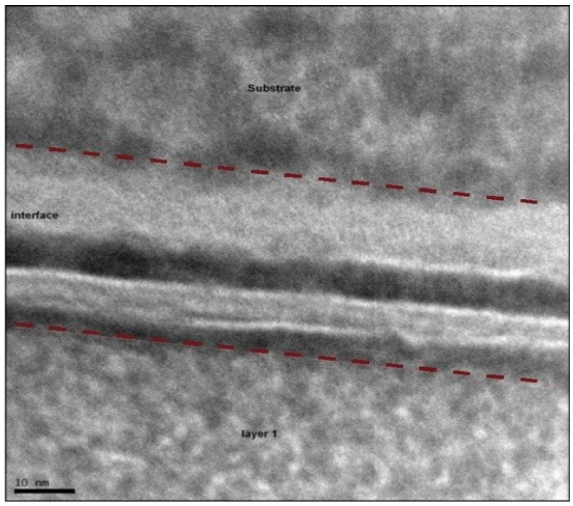

Figure 3.7: TEM image (CM300) of the interface between coatings derived from a SiTi-M sol and a commercial glass substrate. An excessive number of heat treatment steps apparently results in a much less defined interface than observed for the previous SiTi layers (seen Fig. 3.3, for example). Multi-step diffusion of alkalis and alkaline-earths may be the cause of this interface disrupture.

Rare earth doping has been studied in order to open the possibility to explore the wide range of photonics applications that these materials have. Figure 3.8 shows a micrograph corresponding to a representative erbium-doped SiTi sample. Like the non-doped sample, the phases are clearly identified, and no discontinuities due to cracks or mistmaches are present. The darker contrast area observed at the coating placed together to the interface between materials is due to the presence of heavier atomic weight elements, such as Ti and Er. An excellent adherence between coating and substrate is demonstrated again.

The EDS analysis allowed corroborating the existence of the diffusion process mentioned earlier (Figs. 3.9-3.10). Alkalis and alkaline-earth species migrate from the substrate to the coating; in the same way that we explained before for the non-doped SiTi sample. This diffusion process yields a silica enriched zone at the top of the substrate, as deduced from the spectra represented in Figure 3.3. The EDS analysis also allowed observion of a higher Ti and Er concentration in the proximity of the interface than in the external part of the coating. In contrast, the concentration of alkalis and alkaline-earth atoms seems continuous along the thickness of the coating (Fig. 3.10).

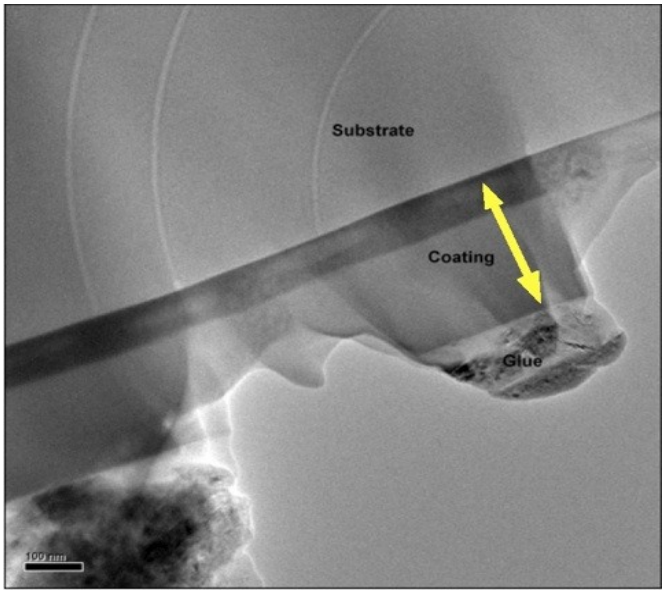

Figure 3.8: TEM image (CM300) of a polished erbium-doped SiTi sample interface area near the substrate. The interface is well-defined by a dark contrast line within the film, which corresponds to a higher content of higher atomic weight species and Ti. The thickness of the coating is denoted by a yellow arrow.

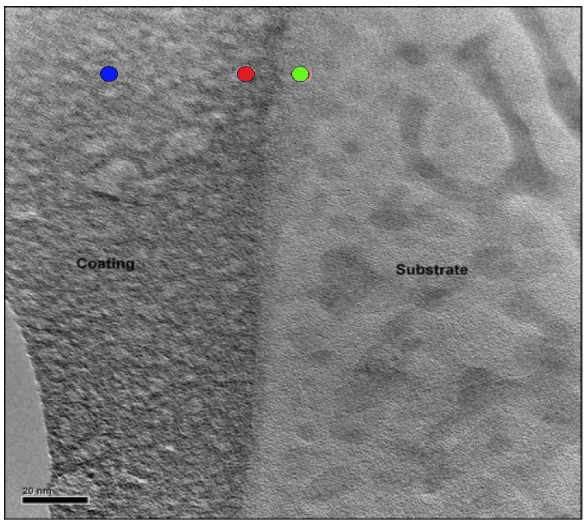

Figure 3.9: TEM (CM300) image corresponding to a close-up view of the substrate-coating interface region of the erbium-doped SiTi sample; EDS analysis were performed over the different phases present at the interface: the darker contrast area of the coating (red dot) and the external part of the coating (blue dot). The silicon-rich zone is marked by a green dot.

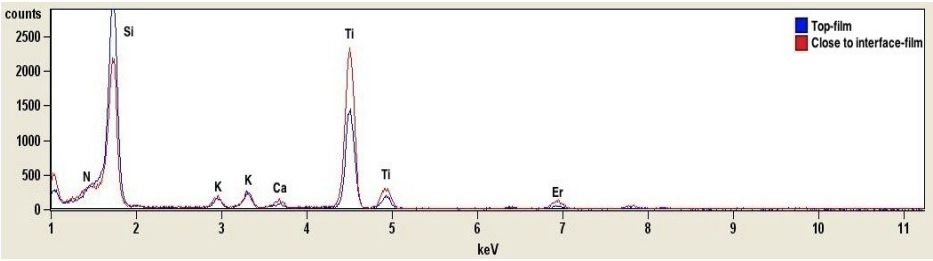

Figure 3.10: Comparison of the EDS spectra obtained at the marked, colored points of Figure 3.9 for an erbium-doped SiTi sample. The amount of Ti and Er in the area close to the interface (red) is higher than the external parts of the coating (blue) and is responsible for the darker contrast zone observe adjacent to the coating-substrate interface. In contrast with non-doped samples, the concentration of alkalis and alkaline-earth elements is practically constant along the thickness of the coating.

In order to test the applicability of this preparation route to coating compositions which may yield layers with higher index of refraction values, a ZrCe coating was prepared to be similarly characterized. A TEM image of the polished and thinned cross section of a ZrCe sample, obtained by dip-coating of the corresponding sol onto a soda-lime glass substrate is shown in Figure 3.11. A well-defined interface is observed between the apparently homogeneous coating and the substrate. The much darker contrast observed for the coating is due to the presence of heavier metals, Zr and Ce, in addition to K and Ca species, expected to migrate via diffusion from the soda-lime glass substrate, as discussed earlier in the text. The micrograph of Figure 3.11 also suggests efficient coupling between the sol-gel derived layer and the substrate, in view of the clear-cut and clean interface exhibited. The rest of the sol-gel ZrCe layer is apparently homogeneous and, in principle, it appears to contain no crystalline phases.

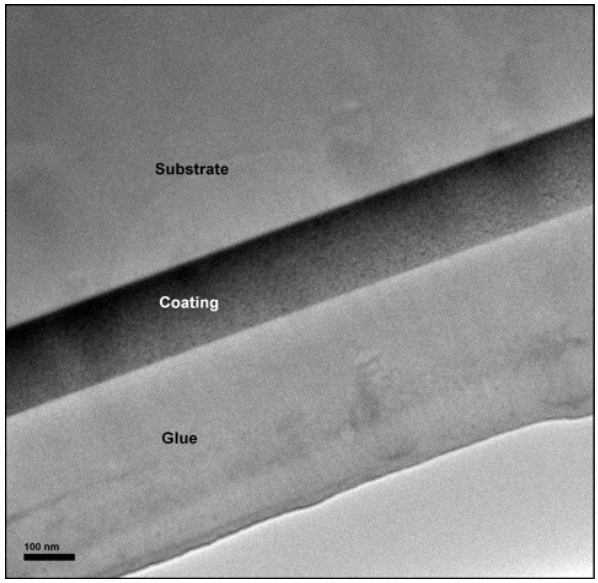

Figure 3.11: TEM image (CM300) of the polished and thinned cross section of a ZrCe sample, obtained by dip-coating of the corresponding sol onto a soda-lime glass substrate. A well-defined interface is observed between the apparently homogeneous coating and the substrate. The much darker contrast observed for the coating is due to the presence of phases containning heavy elements, such as Zr and Ce.

Figure 3.12 shows a high magnification TEM micrograph (a) and its corresponding EDS spectra (b) obtained at points near the ZrCe coating-glass substrate interface, on the substrate (red) and on the coating layer (blue) of the sample observed in Figure 3.11. This was performed in order to ascertain compositional uniformity and atomic diffusion processes, as observed in the previous Si-Ti system. The EDS spectra shown (Fig. 12b, right) confirm the abundant presence of K and Ca within the coating, along with Zr and Ce (blue dot, top), giving it also a dark contrast appearance. The spectrum obtained on the red dot (bottom) corresponds to a silica-rich zone at the substrate near the interface, developed at the expense of intense alkali and alkaline-earth diffusion into the coating. The latter region appears, consequently, with a much lighter grey contrast.

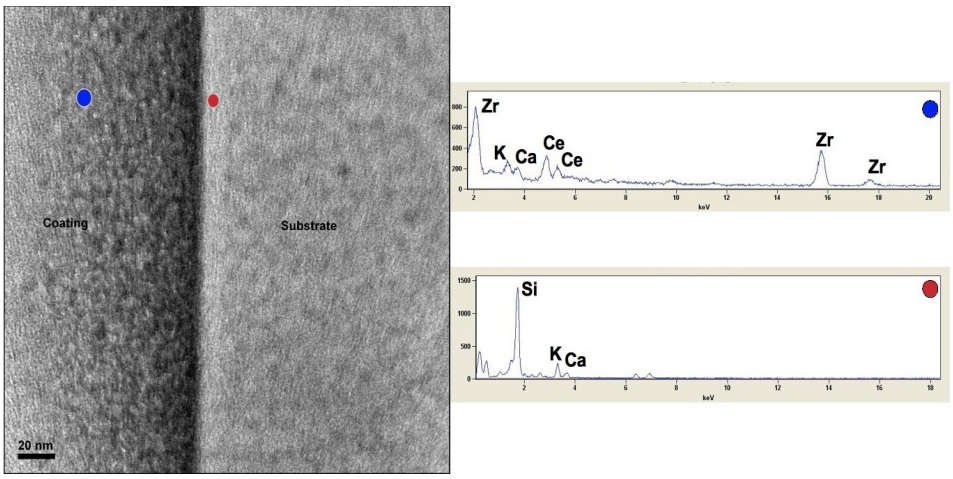

Figure 3.12: TEM (CM300) image (left) corresponding to the interface between the ZrCe sample coating and the commercial soda-lime glass substrate. Analysis was performed at points of the interface, on the substrate (red) and on the coating (blue). The EDS spectra shown (right) confirm the abundant presence of K and Ca within the coating, along with Zr and Ce (blue dot, top), giving it also a dark contrast appearance. The spectrum obtained on the red dot (bottom) corresponds to a silica-rich zone at the substrate near the interface, developed at the expense of intense alkalis and alkaline-earth diffusion into the coating. The latter region appears, consequently, with a much lighter grey contrast.

The last final TEM microstructure studies for Sol-Gel waveguides correspond to the characterization of the SiO_2:CeO_2 hybrid system , prepared in order to obtain a thick layer in a one-single step, dip-coating process. For the latter, the corresponding sol contains a considerably higher concentration of organic ligands, as compared to the previous sol-gel preparations discussed in this work. A TEM micrograph, obtained on a thinned, polished SiCe hybrid coating at high magnification, is shown in Figure 3.13. The adhesion between the hybrid coating and the glass substrate appears similar to those in other Sol-Gel samples reported here. The alkali and alkaline-earth diffusion effect previously mentioned is observed again here, favouring efficient coupling between the coating and the substrate materials. Moreover, the silicon rich zone near the interface is observed more clearly in this micrograph, where it appears with a big contrast and very close to the interface (white area). Contaminant phases, such as KCl, present due to contamination arising from the polishing and thinning procedures employed, are clearly identified throughout the sample cross section, especially on the side of the coating, as expected from its lower apparent density.

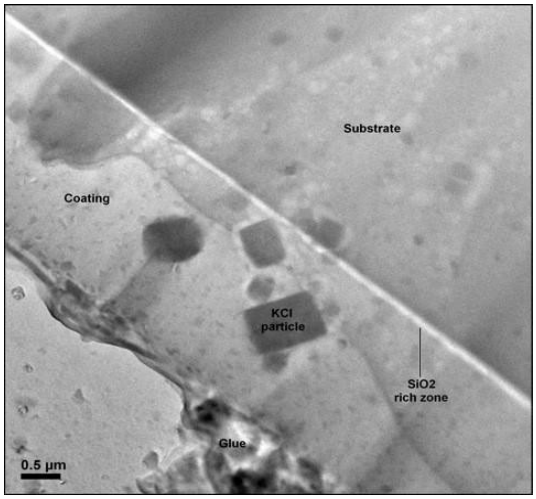

Figure 3.13: TEM image (CM300) obtained on a thinned and polished SiCe sample coating. A SiO2 zone, depleted of alkalis and alkaline-earths is indicated as a much lighter, white contrast line, parallel to the substrate-coating interface. Contaminant phases, such as KCl, present due to contamination from the polishing and thinning procedures employed, are clearly identified throughout the sample cross section, especially on the side of the coating, as expected from its lower density.

The UV/Vis transmission spectrum of Sol-Gel layers appears greatly different depending on the kind of composition registered. It is due to the different precursor materials employed for their preparation and, therefore, their different composition. The SiO_2:TiO_2 and SiO_2:CeO_2 introduce a small change in transmission with respect to the substrate, due to their similar glass composition (and, therefore, their similar refractive indices). The ZrO_2:CeO_2 system present several differences with the microscope slide glass substrate spectrum. In this case, we have a material absolutely different in its composition, exhibiting a much higher refractive index. The fact that a high refractive index supposes a high reflection of light, results in much lower percentage of transmitted light along of the part of the electromagnetic spectrum measured (Fig. 3.14). The maxima and minima of the curves due to surface plasmon resonance (SPR) and/ or nanoparticle structures are in concordance with the results presented in the literature [38, 56-57 and references therein].

The spectrum of the same composition changes depending on the quantity of layers as observed in Fig. 3.15 for the SiO_2:TiO_2 (70:30) composition sample. The use of Er as dopant modifies the spectrum significantly.

The multilayer structures present multiple maxima and minima. This fact was referred to when the utility of this technique was discussed to check the transmission windows of films for light guiding. These windows permit us to have an approximate idea about the adequate light sources to be used in order to achieve reasonable guiding efficiencies.

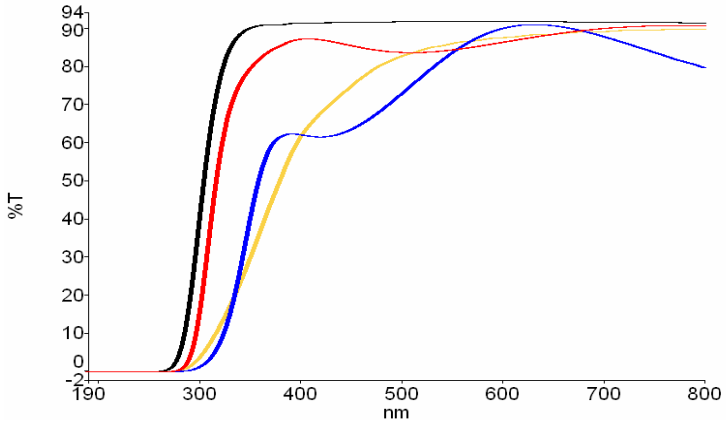

Figure 3.14: UV-Vis transmission spectra of the microscope slide (black) and monolayer coatings of SiO_2:TiO_2 (70:30, red), SiO_2:CeO_2 (95:5, yellow) and ZrO_2:CeO_2 (70:30, blue).

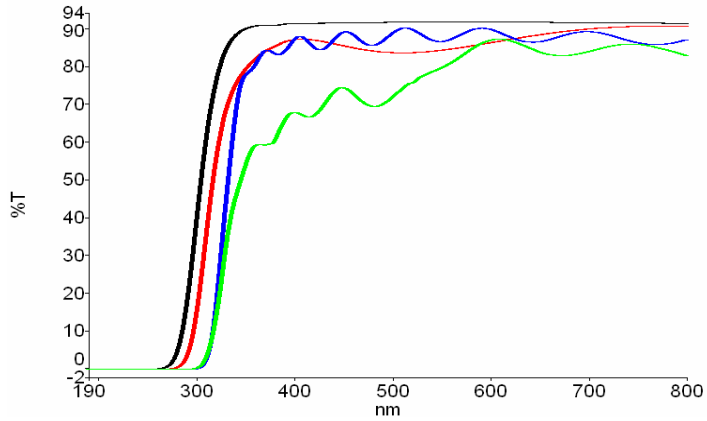

Figure 3.15: UV-Vis transmission spectra of the microscope slide (black) and the different formats of the composition SiO_2:TiO_2 (70:30); monolayer (red), multilayer (blue) and erbium-doped (green).

Finally, after the microstructural analysis of the samples, the optical studies over Sol-Gel samples were carried out. These measurements, consisting of mode characterisation and measurement of losses were realised at the *Istituto di Fisica Applicata 'Nello Carrara'* (IFAC-CNR, Firenze, Italy). The waveguiding modes were characterized by the instrument COMPASSO, and the results obtained allowed us to calculate the effective refractive index and the thickness of the waveguides by mathematical analysis through the dedicated sofware (based in the inverse of the WKB method) as explained in the experimental chapter of this thesis.

The first specimen investigated was the multilayer structure SiTi (70:30). As observed in Figs. 3.16 and 3.17, where abscissas axis represents the refractive index value and the ordinates axis represent the power intensity received by the photodiode, two modes were founded for TE and for TM polarizations at wavelength λ=635 nm. At 980 nm and 1550 nm only one propagation mode was found. In Figs. 3.16 and 3.17 the dip of the signal curve corresponds to a waveguiding mode; the knee of the curve, n=1.512 corresponds instead to the refractive index of the commercial glass substrate (in this case, microscope slides).

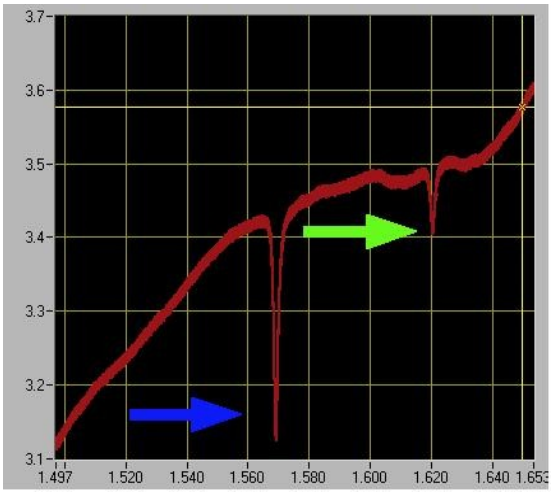

Figure 3.16: TE modes (n_0=1.6206, green; n_1=1.5693, blue; SF-14 prism) at 635 nm for multilayer SiO_2:TiO_2 (70:30) characterised by the COMPASSO instrument [56].

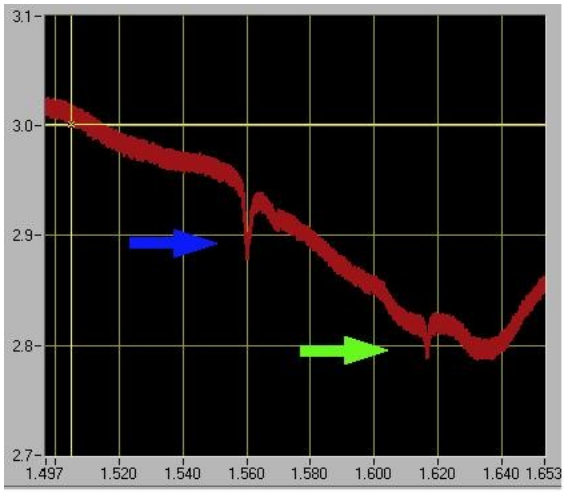

Figure 3.17: TM modes (n_0=1.6218, green; n_1=1.5604, blue; SF-14 prism) at 635 nm for multilayer SiO_2:TiO_2 (70:30) characterised by the COMPASSO instrument [56].

The results obtained are summarized in Table XV. In order to complete this study, Table XVI compares the effective refractive index obtained by this method with the value obtained by spectral ellipsometry. The values are somehow different. Most of the published literature considers more reliable the values obtained by the dark m-line spectroscopy.

Table XV: TE and TM mode indices (±0.0005) obtained with the COMPASSO instrument for multilayered SiO_2:TiO_2 (70:30) Sol-Gel coatings deposited onto microscope slide substrate.

Wavelenght	**prism**	**TE mode**		**prism**	**TM mode**	
635 nm	***SF-14***	n_0	1.6206	***SF-14***	n_0	1.6218
		n_1	1.5693		n_1	1.5604
980 nm	***SF-14***	n_0	1.5864	***SF-14***	n_0	1.5798
1550 nm	***SF-14***	n_0	1.5381	***SF-14***	n_0	1.5381

Table XVI: Refractive index (±0.001) and thickness calculated from mode indices compared with spectral ellipsometry values obtained for multilayered SiO_2:TiO_2 (70:30) Sol-Gel coatings deposited onto microscope slide substrate.

SiO_2:TiO_2 (70:30) multilayer	**Ellipsometry (633 nm)**	**TE (635 nm)**	**TM (635 nm)**
Refractive index (n)	1.590	1.640	1.643
Thickness (nm)	1230	1080	1040

The specimens deposited onto commercial glass substrates were also measured, yielding the same results in terms of the number of modes allowed by the waveguide. Both, indices and thicknesses are similar to the values obtained with the microscope slides, but the large thickness of these specimens make these measurements more complex. Another factor which promotes differences is the refractive index of the commercial glass substrates (n=1.517), which is just a little higher than that of the microscope slides (n=1.512). Table XVII presents the calculated refractive indices obtained for the multilayer coatings prepared on microscope slides, while Table XVIII presents a comparison of these with values obtained by spectral ellipsometry.

Table XVII: TE and TM mode indices (±0.0005) obtained with the COMPASSO instrument for multilayered SiO_2:TiO_2 (70:30) Sol-Gel coating deposited onto commercial glass substrate.

Wavelenght	**prism**	**TE mode**		**prism**	**TM mode**	
635 nm	***SF-14***	n_0	1.6118	***SF-14***	n_0	1.6090
		n_1	1.5678		n_1	1.5615
980 nm	***SF-14***	n_0	1.5807	***SF-14***	n_0	1.5756
1550 nm	***SF-14***	n_0	1.5387	***SF-14***	n_0	1.5385

Table XVIII: Refractive index (±0.001) and thickness calculated from mode indices compared to values ontained by spectral ellipsometry and with the values calculated for the multilayer SiO_2:TiO_2 (70:30); all coatings were deposited onto commercial glass substrates.

SiO_2:TiO_2 (70:30) multilayer window glass	**Ellipsometry micro-slide (633 nm)**	**TE micro-slide (635 nm)**	**TE window glass (635 nm)**	**TM micro-slide (635 nm)**	**TM window glass (635 nm)**
Refractive index (n)	1.590	1.640	1.627	1.643	1.625
Thickness (nm)	1230	1080	1190	1040	1190

When dark m-line spectroscopy was applied to a monolayer of the same composition, only one mode for TE and for TM was found at the wavelenght λ=635 nm. No modes were found for higher wavelengths, apparently due to the smaller thickness of the coating (358 nm), in consonance with the theoretical studies on the thickness restriction for waveguiding [section 1.2.1]. Moreover the corresponding index is much lower than the value obtained for the monolayer by ellipsometry and for the multilayer by dark m-line spectroscopy (Table XIX)

Table XIX: Refractive index (±0.001) and thickness obtained by dark m-line spectroscopy for a SiO_2:TiO_2 (70:30) Sol-Gel monolayer deposited onto microscope slides and comparison with the results obtained by ellipsometry for the same sample and with the values calculated for the multilayer sample.

SiO_2:TiO_2 monolayer 70:30	**Ellipsometry monolayer (633 nm)**	**TE monolayer (635 nm)**	**TE multilayer (635 nm)**	**TM monolayer (635 nm)**	**TM multilayer (635 nm)**
Refractive index (n)	1.630	1.530	1.640	1.515	1.643

Er-doped silica-titania composition samples were also characterized by dark m-line spectroscopy. A multilayer structure (5 layers) was prepared for a 5mol% Er-doped silica-titania 70:30 composition following the standard experimental procedure to obtain multilayers on microscope slide substrates. The results obtained by the Compasso instrument at the different wavelengths checked show the same number of modes as an undoped composition. While the refractive index is equal for the TE mode and is closer for the TM mode; the thickness is

clearly affected by the introduction of Er. For the same extraction speed of the fabrication technique and the same number of layers, the thickness is lower than for the undoped samples. The critical thickness for this composition was observed to be lower than that obtained for undoped composition. Table XX reports the modes found and Table XXI compares the refractive indices for doped and undoped silica-titania samples.

Table XX: TE and TM mode indices (±0.0005) obtained by COMPASSO instrument for multilayered Er-doped SiO_2:TiO_2 (70:30) Sol-Gel samples.

Wavelenght	prism	TE mode		prism	TM mode	
635 nm	***SF-14***	n_0	1.6150	***SF-14***	n_0	1.6048
		n_1	1.5440		n_1	1.5303
980 nm	***SF-14***	n_0	1.5768	***SF-14***	n_0	1.5641
1550 nm	***SF-14***	n_0	1.5192	***SF-14***	n_0	1.5193

Table XXI: Refractive index (±0.001) and thickness calculated from mode indices for Er-doped and undoped SiO_2:TiO_2 (70:30) multilayer Sol-Gel samples.

SiO_2:TiO_2:Er 635 nm	**TE non-doped**	**TE Er-doped**	**TM non-doped**	**TM Er-doped**
Refractive index (n)	1.640	1.640	1.643	1.632
Thickness (nm)	1080	880	1040	890

The silica-titania multilayers characterised at IFAC did not exhibit a well-densified coating. Due to this fact, when we tried to measure the losses, the higher diffusion of light did not allow us to perform this measurement. To avoid this problem, samples were annealed at 500ºC during 30 minutes. After this process, the samples were studied again with the Compasso instrument. No changes in the number of modes were found, but we can observe how the annealing process induces a slight increase on the refractive index from those measured for each mode at a wavelength of 635 nm (Table XXII). Simultaneously a silica-titania sample was checked. In both cases, a GGG prism was employed.

Table XXII: TE and TM mode indices (±0.0005) obtained with the COMPASSO instrument for annealed and non-annealed multilayer SiO_2:TiO_2 (70:30) Sol-Gel samples.

Wavelenght	prism	mode	TE annealed	TE not-anneal		prism	mode	TM annealed	TM not-anneal
635 nm	**GGG**	n_0	1.6364	1.6210		**GGG**	n_0	1.6331	1.6171
	GGG	n_1	1.5711	1.5673		**GGG**	n_1	1.5610	1.5579
1550 nm	**GGG**	n_0	1.5347	1.5347		**GGG**	n_0	1.5299	1.5298

Table XXIII shows these values and compares them with the previous values obtained by spectral ellipsometry and by dark m-line spectroscopy for the silica-titania multilayer waveguide. The previous study by dark m-line spectroscopy employed a SF-14 prism. In Table XXIII, values for non-annealed specimen studied with a GGG prism are marked in green, and the corresponding values for the specimen studied with the SF-14 prism are coloured in yellow.

Table XXIII: Effective refractive indices (±0.001) and thickness calculated from mode indices compared to values obtained by spectral ellipsometry and with the values calculated for the different kind of SiO_2:TiO_2 (70:30) multilayer Sol-Gel samples.

SiO_2:TiO_2 multilayer microslide	Ellipsometry (632 nm)	TE previous (635 nm)	TE not-anneal (635 nm)	TE anneal (635 nm)	TM previous (635 nm)	TM not-anneal (635 nm)	TM anneal (635 nm)
Refractive index (n)	1.590	1.640	1.640	1.660	1.643	1.638	1.658
Thickness (nm)	1230	1080	1060	940	1040	1060	950
prism	**x**	**SF-14**	**GGG**	**GGG**	**SF-14**	**GGG**	**GGG**

As we can see in Table XXIII, the annealing process supposes a decrease on the thickness due to the densification of the Sol-Gel coating. The literature studied [56] to prepare this type of Sol-Gel composition does not report any birefringence effect.

Finally, the ZrCe (70:30) multilayer was also optically characterized by dark m-line spectroscopy. In contrast to the silica-titania compositions, the high refractive index of this composition forced us to use a prism with a higher refractive index. The use of rutile and GGG prisms enabled access to a range of

index values lying between the substrate (microscope slide, n=1.512) and the rutile prism (n=2.1) (Fig. 3.18).

In Fig. 3.18c, a secondary minimum at n=2.04 is observed. After mathematical treatment of the data (inverse of the WKB method), indicates that this point is neglected as originating from a mode corresponding to the zirconia-ceria coating. In Fig. 3.18a the knee signal (dip) associated to the waveguide-substrate interface is also clearly identifyable and marked with a violet coloured arrow.

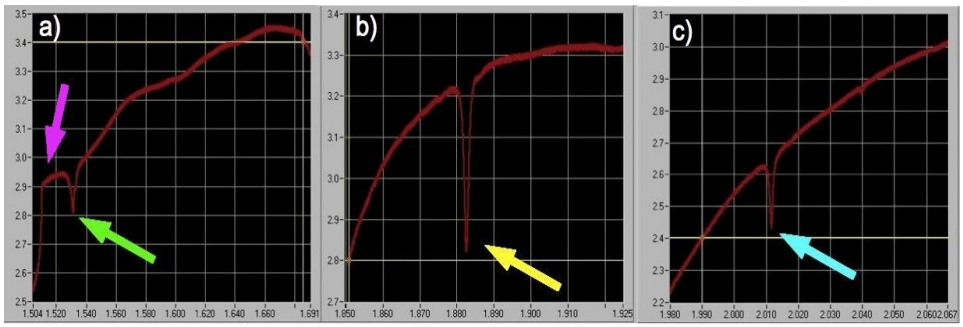

Figure 3.18: TE fundamental modes (n_0=2.0108 (blue arrow), rutile prism; n_1=1.8078 (yellow arrow) and n_2=1.5316 (green arrow), GGG prism) at 635 nm for the ZrO_2:CeO_2 (70:30) multilayer Sol-Gel coating. The knee signal arising from the coating-substrate interface is around n=1.512 (violet arrow).

Table XXIV summarizes the propagation modes for the zirconia-ceria multilayer waveguide at 635 nm and 1550 nm. At λ=635nm we have found three TE propagation modes and only two for the TM modes, that is, this multilayer behaves as a birrefringent medium. For a wavelength of λ=1550nm only one TE and one TM mode were found. The effective refractive indices for TE and TM propagation modes are clearly different (Table XXV). This means that the coating will behave optically different depending on the polarization state of the beam coupled to the waveguide. Incidently, birefringence is not found in the SiO_2:TiO_2 media, as expected from its glass nature.

Table XXIV: TE and TM mode indices (±0.0005) obtained with the COMPASSO instrument for ZrO_2:CeO_2 (70:30) multilayer Sol-Gel coatings .

Wavelenght	prism	TE mode		prism	TM mode	
635 nm	***rutile***	n_0	2.0108	***rutile***	n_0	2.0068
	GGG	n_1	1.8078	***GGG***	n_1	1.7635
	GGG	n_2	1.5316		-	-
1550 nm	***rutile***	n_0	1.8826	***rutile***	n_0	1.7020

Table XXV: Refractive index (±0.001) and thickness calculated from mode indices for ZrO_2:CeO_2 (70:30) multilayer Sol-Gel coatings.

ZrO_2:CeO_2 (70:30) multilayer	Ellipsometry (633 nm)	TE (635 nm)	TM (635 nm)
Refractive index (n)	2.040	2.070	2.087
Thickness (nm)	490	520	500

The presence of tetragonal type ZrO_2 crystalline phases, which may account for the coating's birefringence, was detected by XRD. Crystalline phases are observed by XRD (Fig. 3.19). These crystalline phases are identified as zirconium-cerium oxide type nanostructures, since no crystalline phases were observed by TEM. In fact, Crepaldi et al. [167] studied the preparation of thin films of yttria-zirconia and ceria-zirconia by evaporation-induced self-assembly (EISA) and reported the presence of different zirconium nanocrystalline particles. Their morphology was observed to depend on the annealing temperature; at 300ºC 3D cubic nanostructures were present, while 2D hexagonal structures were predominant at 500ºC. Moreover, Crepaldi et al. [167] observed that it is possible to obtain multilayers free of organic compounds at an annealing temperature of 400ºC. Ruiz et al. [168] and Sotelo et al. [169] have demonstrated that a combustion process takes place during formation of oxide films from Sol-Gel type coatings, assisted by the high potential energy stored in organic compounds. These suffer combustion processes via exothermic routes, contributing to raise the internal temperature of the substance under combustion, above that set as the external annealing temperature for the process. This fact is in consonance with the study of Liu et al. [170], which reported on the presence of ZrO_2 tetragonal structures within 87:13 ZrO_2:CeO_2 mixture thin films,

prepared by the sol-gel route and annealed at 600ºC. Soo et al. [171] observed the presence of cubic phases within ZrO_2 films deposited by ion-beam-assisted-deposition (IBAD) and the diffraction peak values reported differ from those obtained for tetragonal phases within the present zirconia-ceria sol-gel coating (Fig. 3.19). These values recorded here with diffraction maxima at 30º and 50º, are, however, in consonance with the values reported by Turko et al. [172] and the bibliography reported therein for the zirconia-ceria compositions. Four signals arising from the presence of crystalline structures, recorded for the ZrO_2:CeO_2 monolayer sample are also present in the spectrum corresponding to the ZrO_2:CeO_2 multilayer sample. These values are placed at 30, 35, 50 and 60º.

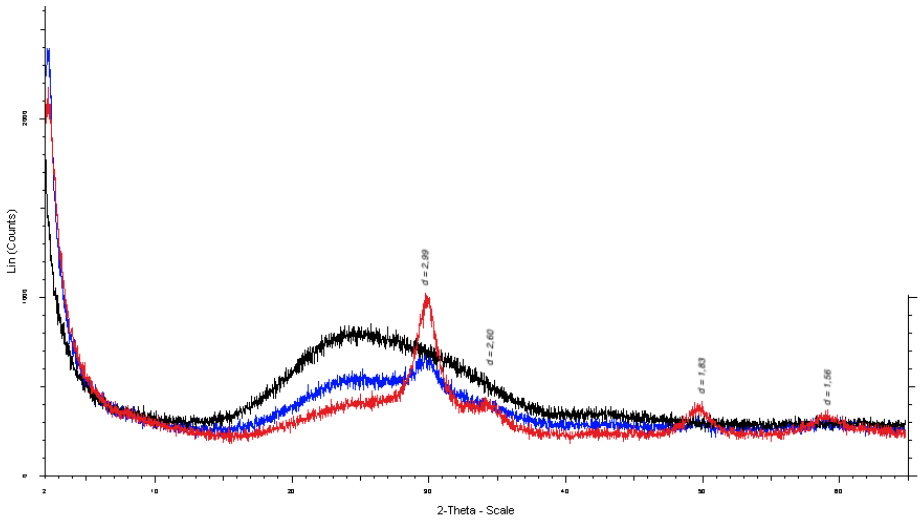

Figure 3.19: XRD patterns obtained on the commercial glass substrate (black), the Zr-Ce monolayer (blue) and the Zr-Ce multilayer (red). The peaks at 30º and 50º 2-theta-scale (d=2.99 and 1.83, respectively) correspond to tetragonal phases of zirconia which appear after the heat treatment at 450ºC.

In order to test the potential applicability of the thick planar SiCe Sol-Gel layer as a slab waveguide, a He-Ne laser beam was focused onto the front part of a SiCe coated glass substrate using a 40X objective of NA 0.6. Figure 3.20a depicts light propagation through the substrate when no layer has been applied. The light refracted into the glass is scattered and, at the output face, a spread spot can be observed. For comparison, in figure 3.20b we can see how light is

confined into the SiCe layer by multiple internal reflections. The size of the spot at the output is related with the NA of the objective and the longitudinal dimension of the coating, and slight waveguide losses are present due to absorption and scattering phenomena that take place within the coating. These were measured using the double prism method [160-161]. Considering an input power of 24 mW and outpower of 17 mW, waveguide losses of 1.50 dB/cm were calculated according to Equation 2.20.

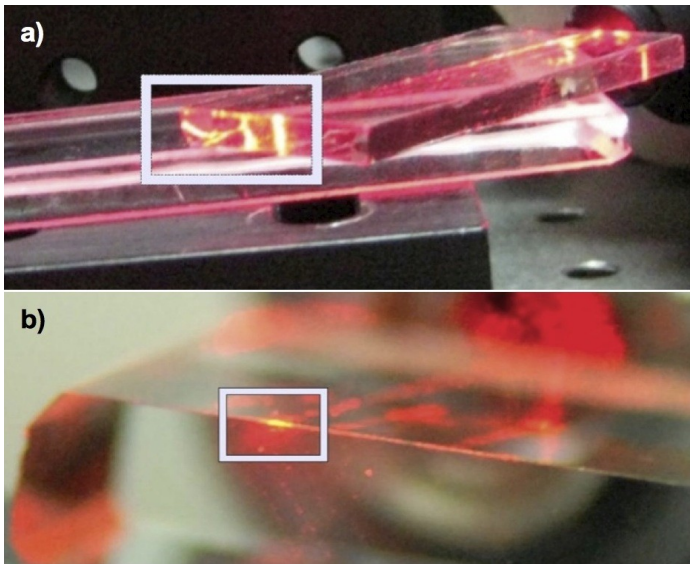

Figure 3.20: a) Light propagation through the glass substrate, without the presence of a Sol-Gel layer. The light refracted into the glass substrate is scattered within its volume, giving rise to a wide spot at its output face. b) Light confinement in the Si-Ce step-index Sol-Gel waveguide by multiple internal reflections.

Losses of SiTi and ZrCe Sol-Gel multilayers deposited on microscope slide substrates were measured at the *Istituto di Fisica Applicata 'Nello Carrara'* (Firenze, Italy) by a method based on scattered light. The SiTi (70:30, 5 layers) sample was first annealed to densify the coating in order to measure the losses reliably. A thermal treatment at 500ºC during 30 minutes was applied to the sample. The two TE propagation modes at 633 nm are easily found after the

annealing process (Fig. 3.21); but only one exhibit enough intensity levels to facilitate measuring the losses (see Fig. 3.22 and Table XXVI).

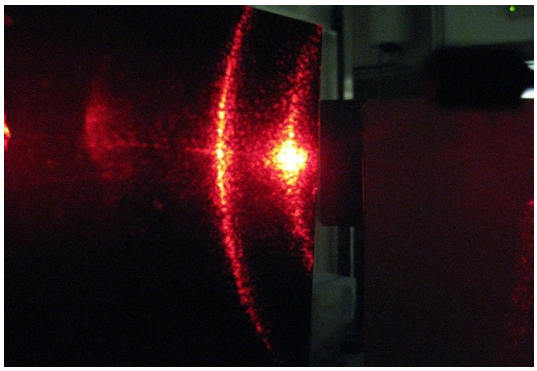

Figure 3.21: Image of the two modes observed on SiO_2:TiO_2 multilayer Sol-Gel coatings projected on a black screen. Laser coupling was realised through a rectangular GGG prism. He-Ne laser emitting at the wavelenght of 633 nm was used as light source.

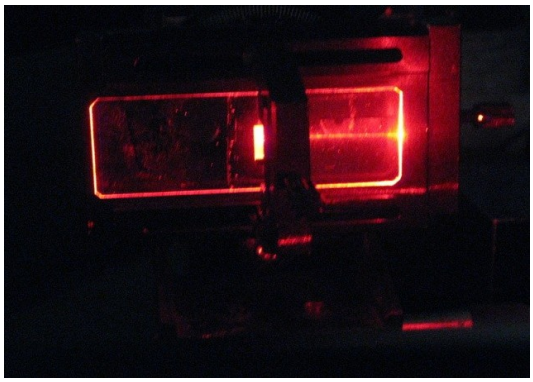

Figure 3.22: Guiding of light from an He-Ne laser (633 nm) trough an annealed SiO_2:TiO_2 (70:30) multilayer Sol-Gel coating. The coupling was made through a rectangular GGG prism.

The ZrO_2:CeO_2 Sol-Gel coating exhibits two values for the attenuation coefficient at a wavelength of 633 nm: 0.9±0.2 dB/cm and 1.5±0.2 dB/cm, for the TE and TM modes, respectively (Table XXVI). Bihn et al. [173] previously

reported this property for a ZrO_2 waveguide obtained by ion-assisted deposition; observing how the attenuation coefficient depends on the polarization of the light. This supports the fact that the structural anisotropy intrinsic to the tetragonal zirconia phase is responsible for the birefringence observed in the ZrCe samples studied here.

Table XXVI: Losses measures (±0.2) obtained for Sol-Gel waveguides by a method based on scattered light.

System	Polarization	Losses (dB/cm)
SiO_2:TiO_2 (70:30)	***TE polarization***	1.3
ZrO_2:CeO_2 (70:30)	***TE polarization***	0.9
	TM polarization	1.5

3.2 Laser Zone Melting (LZM)

Planar and channel waveguides from inorganic oxides coated commercial glass substrates were made by (i) melting in a conventional furnace and (ii) by LZM. Compositions based on lead borosilicate glasses were prepared and studied using physico-chemical characterization techniques.

IR spectra were taken on a lead borosilicate frit (Fig. 3.23) and on a commercial soda-lime glass substrate (Fig. 3.24). The IR spectrum registered for the frit exhibits a series of peaks that correspond to structures formed within the coating and which do not appear in the spectrum of the substrate.

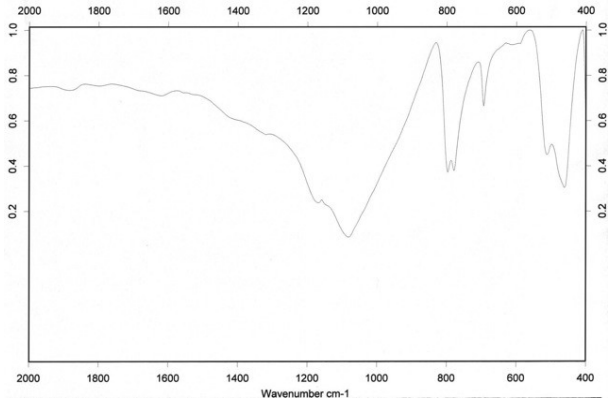

Figura 3.23: FTIR transmission spectrum of lead borosilicate frit.

The spectrum represented in Fig. 3.23 contains the following bands: at around 600 cm^{-1} which corresponding to the characteristic vibration of Pb-O bonds; at around 700 cm^{-1} corresponding to B-O-B vibrational bending; at about 790 cm^{-1}, corresponding to Si-O-Pb vibrations. From 830 cm^{-1} to 1300 cm^{-1} a depression is observed and is assigned to the BO_4 stretching vibration (around 1000 cm^{-1}), the tetrahedral SiO_4 stretching vibration and Si-O vibrations due to non-linked oxygens in tri-coordinated Si groups [67, 174].

When we analyze the comercial glass substrate (Fig 3.24), it clearly appears that there are no vibrations where Pb atoms are involved. Moreover, it was

observed that the signal due to the SiO_4 tetrahedral stretching vibration (band around 1100 cm^{-1}) is more intense [67, 174].

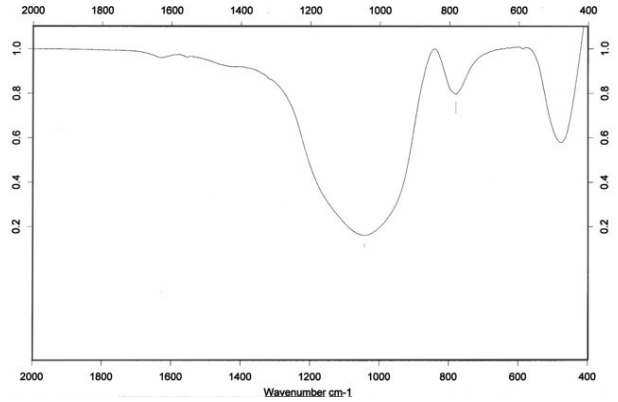

Figura 3.24: FTIR transmission spectrum of commercial soda-lime glass substrate.

The Raman spectrum of one lead borosilicate frit is shown in Fig. 3.25 confirming the results obtained by IR spectroscopy. A resonance peak around 560 cm^{-1} corresponds to the B-O-B stretching vibration, influenced by the presence of BO_4 groups in the proximity, the tail of this peak is probably an effect caused by the presence of Pb-O bonds in its vicinity. The latter resonate at ca. 620 cm^{-1}. The peak around 800 cm^{-1} is assigned to the BO_4 type rings. The peak above 1100 cm^{-1} corresponds to Q_4 groups (SiO_4) and seemed increased in intensity by the presence of Si-O-Pb groups [134, 174].

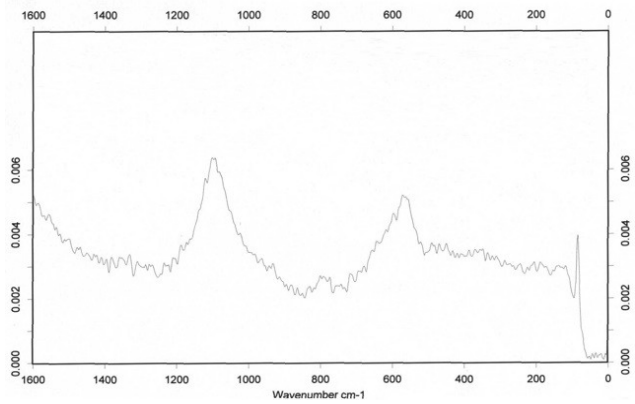

Figura 3.25: Raman spectrum of lead borosilicate frit.

X-ray diffraction was also used to analyze the lead borosilicate frit. As we observe in the subsequent diffractogram (Fig. 3.26), there are no diffraction maxima, an indication that the system study is composed basically of glass or amorphous phases, as desired initially for the waveguiding coating.

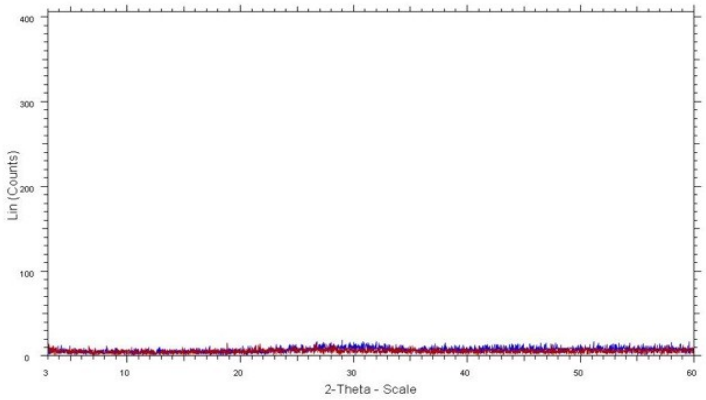

Figura 3.26: XRD diffractogram of a lead borosilicate frit. The blue pattern corresponds to the frit-derived coating; the red pattern corresponds to the soda lime glass substrate.

X-ray Fluorescence analysis perform on frit coating indicated that it was mostly composed of Pb and around 8% Si. This amount of silica suggestd that significant diffusion has taken place across the subsatrate-coating interface,

which Si from the original frit composition in the coating, incorporated into the glass substrate. These results confirms the existence of a diffusion phenomenon that could help to increase the chemical compatibility between the materials involved as substrate and coating. This diffusion driven coupling process will be studied in detail by transmission electron microscopy and discussed in a later section of this text. The results of the X-ray fluorescence analysis performed on the substrate are also shown in Table XXVII and confirm their coincidence with typical commercial soda-lime glass compositions.

Table XXVII: Proportion of main elements (in at%) found in the XRD analysis of the guiding layer and substrate corresponding to the lead borosilicate frit coated sample.

	%Pb	***%Si***	***%Ca***	***%Al***	***%Ti***
Substrate	ppm	35.04	2.93	1.82	0.11
Guiding layer	majority	8.04	-	< 0.2	-

Before the study of the samples by transmission electron microscopy, they were checked by confocal microscopy, showing special interest on the channel preparation by mechanical and by laser ablation methods. Optical photographs are shown in Figs 3.27 and 3.28 for the mechannically machinning and laser engraved channel, respectively. This study was carried out at the *Instituto de Ciencia de Materiales de Aragón* (ICMA-CSIC, Zaragoza). Thus, the first study conducted by confocal microscopy deal with the observation of the surface of channels which were engraved mechanically and with laser ablation onto planar commercial glass substrates. This was performed in order to determine which engraving method provides smoother surfaces and thus to avoid the increased number of guiding losses by geometric irregularities on one of the surface of the waveguide. Confocal microscopy surface scanning was performed on a mechanically engraved channel and on a laser ablation engraved substrate. These scans are shown in Figs. 3.29 and 3.30, respectively.

Figura 3.27: Image of mechanically engraved channels obtained on soda lime commercial glass substrates.

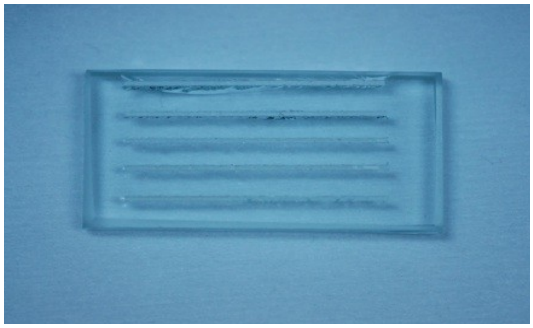

Figura 3.28: Image of channels engraved by laser ablation on a soda lime commercial glass substrate.

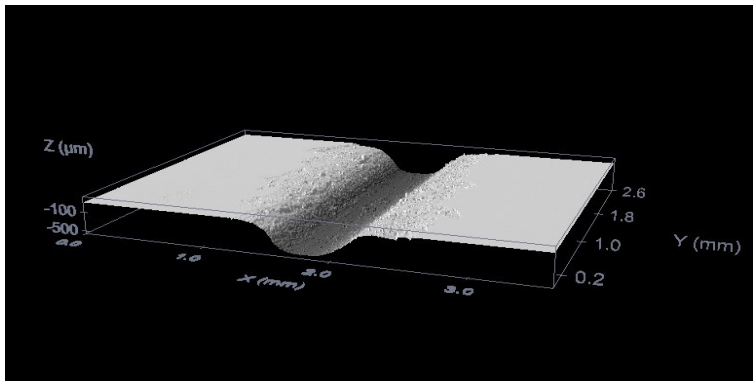

Figura 3.29: Image obtained by confocal microscopy of the surface of a channel mechanically engraved onto a commercial glass substrate.

Figura 3.30: Image obtained by confocal microscopy of the surface of a channel engraved via laser ablation of one planar commercial glass substrate.

The obtention of channels via mechanical methods is laborious and, furthermore, the channels obtained exhibit large surface inhomogeinities. The surfaces show large variations in surface roughness. Furthermore, it is a highly restrictive and slow technique for the development of complex structures and geometries. Laser ablation allows a greater control on geometric aspects such as depth, width or shape in the channel, favors the obtention of complex structures and geometries and allows achieving significantly lower surface roughness, as discussed in the following study, centered on the sample whose photograph is shown in Fig. 3.31. Moreover, the engraving by laser ablation enables process automation, reducing time and facilitating scale-up processes, thus favoring its potential for industrial applications at large.

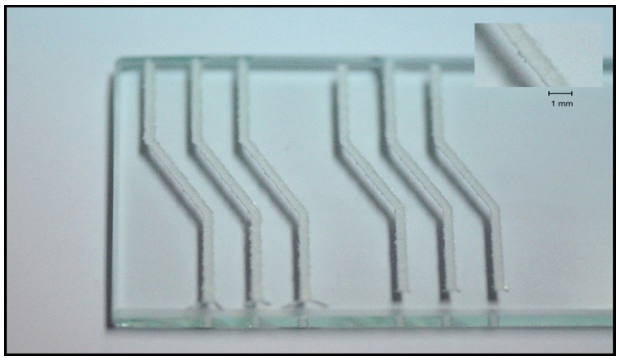

Figura 3.31: Image of broken channels (width 1 mm) engraved via laser ablation of one planar commercial glass substrate.

Laser ablation allows to create channels through various ways, either by marking a filled rectangle (Fig. 3.32) or marking a succession of straight lines (Fig. 3.33). Both situations were studied by confocal microscopy assisted with profilometry. A comparison of both figures indicates that the marking parameters largely determine the surface profiles obtained. Laser ablation channels obtained using line-filled rectangular figures projected onto the substrate result in higher definition channels. Increasing the number of laser pulses per mm, or the pulse rate, will improve surface roughness uniformity and help achieve lower average surface roughness values. In turn, the application of successive straight line-scanning allows obtaining taper structures which tend to form cylindrical cross sections for the channels, which favour the reduction of guiding losses associated to channel geometry.

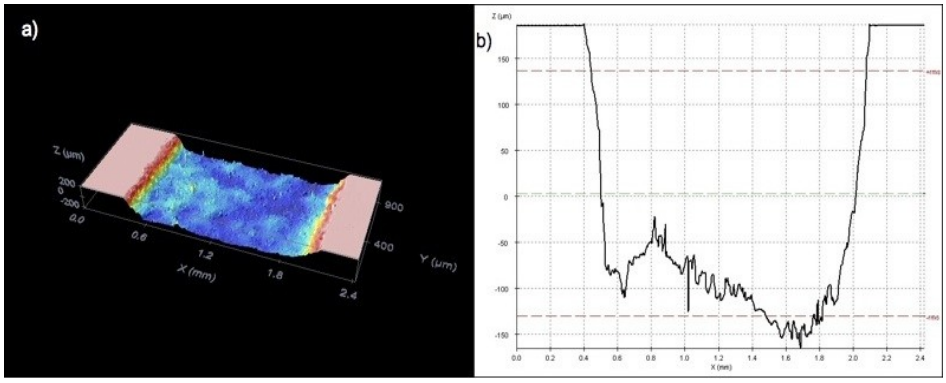

Figura 3.32: a) Confocal microscopy image of a laser ablation channel machined in a soda lime glass substrate using a line-fill rectangular figure projected onto the focal plane. b) XY profile corresponding to the same channel. The machining geometry includes straight vertical walls with nearly rectangular corners.

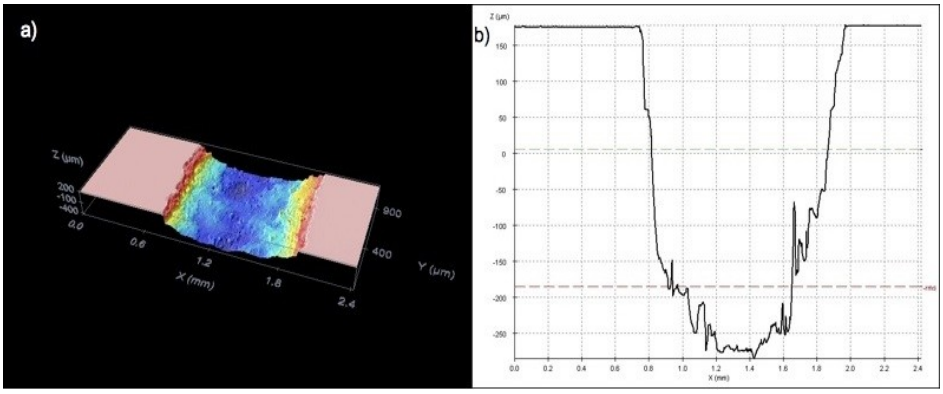

Figura 3.33: a) Confocal microscopy image of a laser ablation channel machined in a soda lime glass substrate using successive straight line scanning procedure. b) XY profile corresponding to the same channel. The resultant machining geometry includes vertical walls with tapered corners.

Laser ablation machining by scanning with a wobbling option, where the laser spot is additionally move in a circular configuration, was also studied. This option allows the retrieval of complex figures in the form of a succession of

arches, intended for decoration, but not for efficient guiding since guiding losses could arise from such a complex geometry (Fig. 3.34).

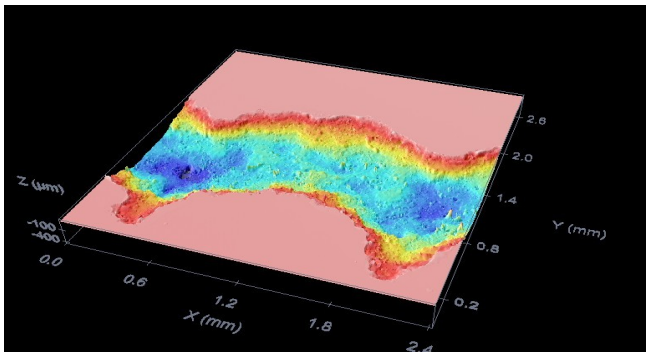

Figura 3.34: Confocal microscopy image of a channel engraved on a planar commercial glass substrate via laser ablation applying the wobbling option.

Once the method and conditions to make channels were establishes, the surface of the glass waveguides subsequently processed was further studied in the case of both, flat and channel substrates. Large macroscopic roughness average values were found in samples prepared by conventional melting. These would be expected to suffer significant waveguiding losses, as the traveling light beam approached the outer surface of the guide layer, where considerable scattering would take place. In contrast, the minimum surface roughness value obtained for the LZM lead borosilicate sample was determined in the range of 230 nm (Fig. 3.35).

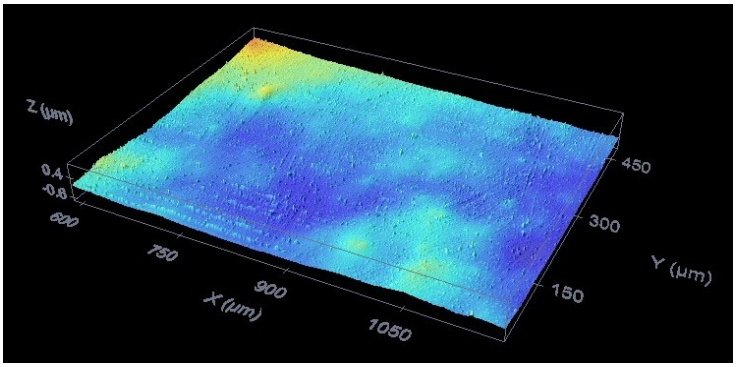

Figura 3.35: Confocal microscopy image of the surface of a lead borosilicate frit coating prepared on a planar commercial glass substrate and treated by LZM.

The application of LZM results in highly homogeneous surfaces with low roughness values. In addition, LZM enables the preparation of any geometrical figure, thus opening the possibility to obtain complex geometry uniform waveguiding channels in one step. Furthermore, LZM achieve this without a previous mechanical or laser ablation process. This means that, once a coating is deposited onto a substrate, the laser can process exclusively the desired channel geometry (Fig. 3.36). But this method has the disadvantage that the non-irradiated areas remain opaque or translucent (Fig. 3.37). The use of CO_2 laser based LZM allows to obtain directly channels with complex geometries using softer processing conditions than other well-known alternative methods. A future study would be the investigation of how emission and scanning parameters affect depth, width and roughness of the channels obtained, and how this affect their waveguiding properties.

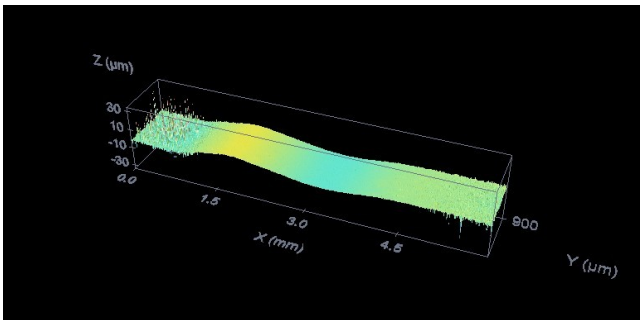

Figura 3.36: Confocal microscopy image of a channel engraved by LZM (blue-green depression). Melting channels onto an inorganic oxide layer deposited over a planar commercial glass substrate.

Figura 3.37: Image of channels obtained by LZM on an inorganic oxide layer coated onto a planar commercial glass substrate. Only the LZM selectively treated areas remain with a permanent optical quality coating (transparent fringes).

One of the first studies performed by scanning electron microscopy on frit samples was the observation of the surface of channels etched into the substrate prior to inorganic oxide deposition. Although the mechanical engraving achieves rounded edges channels in a macroscopic scale as observe in Fig. 3.38, the laser ablation treatment allows, as seen in studies by confocal microscopy, to obtain a

more uniform surface with much lower roughness values (Fig. 3.39). This is achieved with minor variations in geometry in similar lengths in both cases. These results are in consonance with those obtained by confocal microscopy and reinforce the use of the laser ablation method to engrave channels onto commercial glass substrates for the subsequent deposition of glass mixtures.

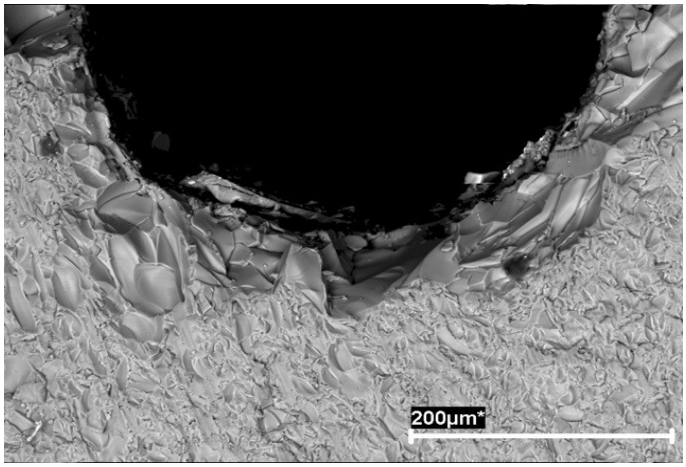

Figura 3.38: SEM image of a mechanically engraved channel onto a planar commercial glass substrate. The surface of the dip is not homogeneous and presents a high average roughness value.

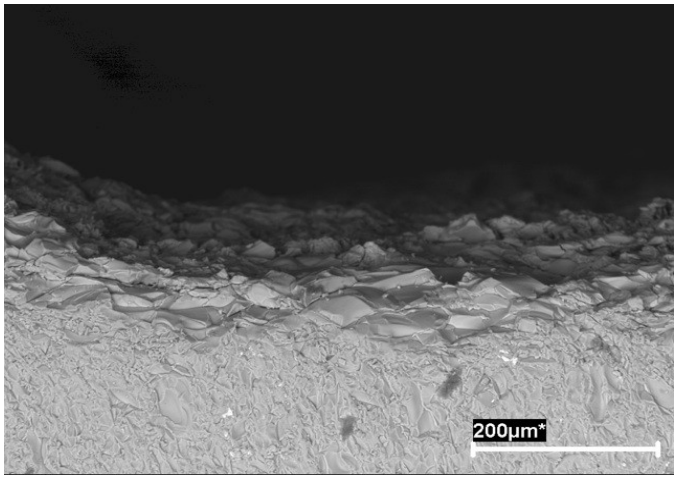

Figura 3.39: SEM image of a channel engraved via laser ablation on a planar commercial soda lime glass substrate. The surface is relatively uniform and its average roughness is bellow 30 µm.

The subsequent SEM study centered on the physical and chemical compatibility between coatings and substrates. The SEM micrographs displayed in Fig. 3.40 correspond to frit coatings with different geometries obtained onto soda-lime glass substrates by conventional furnace thermal treatments. Two types of geometries are shown on the micrographs, corresponding to channel (a, c) and planar (b, d) geometries. The channel type coatings were obtained by initial mechanical machining of the glass substrate, followed by filling with a frit in powder form. The frit was then melted in a furnace at a temperature of 690ºC. On the other hand, the planar coatings were obtained by following the same thermal treatment after deposition with the Doctor Blade method. The resultant materials exhibit excellent surface coupling between the Pb containing glass coating and the soda-lime planar glass substrate, as observed in Figs. 3.40a and 3.40b, where no gaps or bubbles appear at the interface, nor dissimilar phases are present. Figs. 3.40c and 3.40d correspond to compositional maps obtained on the same samples by EDX analyses. They demonstrate that the Pb content is restricted exclusively to the coating, as expected from the observed differences in contrast within the corresponding backscattered electron images (a and b). The mechanically non-uniform interface observed in Figs. 3.40a and 3.40c is an indication that the soaking temperature used was able to melt the frit efficiently,

but did not apparently change the surface roughness induced by machining on the glass substrate. In addition, macroscopic defects are observed at the surface of the coating in Fig. 3.40b. These are expected to cause light scattering, as observed in some of the samples studied (Fig. 3.41).

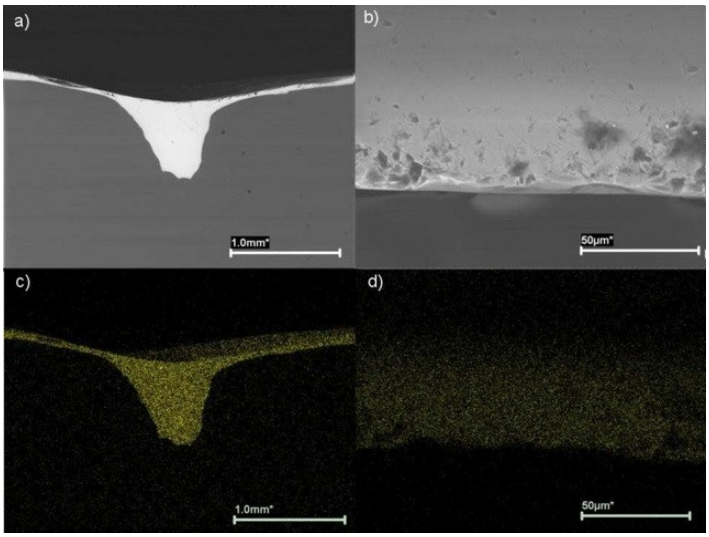

Figura 3.40: SEM micrographs (a & b) and EDX compositional maps of the Pb content within a mechanically engraved channel and within a planar coating obtained on a planar commercial glass substrate. The lead contents promotes the lighter contrast at the micrographs a) and b). The thickness of the layer (d) is around 50 µm.

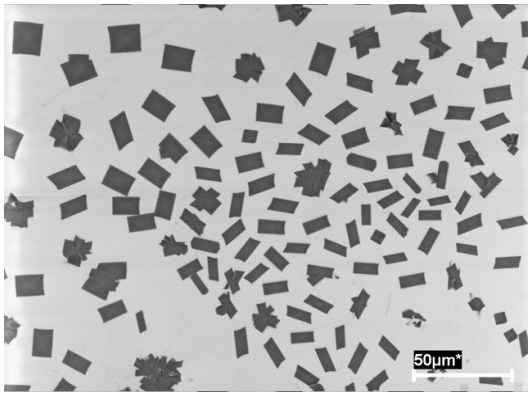

Figura 3.41: SEM micrographs of crystal defects called 'guelelites' at the surface of a lead borosilicate planar waveguide.

These results are consistent with the fact taht guiding is favoured by the presence of a lead containing phase, the lead borosilicate frit coating, which intrinsically has a significantly higher refractive index than the soda lime glass. Although efficient coupling between the two materials is observed, as commented earlier, further interface studies using TEM were considered as necessary, in order to determine coating-substrate coupling at higher resolution. The interface and the process responsible for the good chemical union between these materials were studied as described in the experimental section of this work.

Lead borosilicate sample studies allowed checking the existence of a diffusion process between the substrate and the frit coating, which produces chemical and physical union between both materials. From the lead borosilicate sample study, the existence of a diffusion process between the substrate and the frit layer is deduced from Figs. 3.42 and 3.43. Calcium cations are thus observed to diffuse from the substrate to the frit layer, while a similar phenomenon takes place with the diffusion of lead in the opposite direction, from the coating into the substrate, although at a much lower level. This study allows to discover a thin interface around 5 μm (Figs. 3.42-3.43), somewhat diffuse but sufficiently clear to be a nonequivocally identified. In Figures 3.42 and 3.43 are represented the compositional profiles of Ca and Pb; the interface is a diffuse zone around

the compositional equilibrium point. No crystalline phases were found in the adherent layer. Its compositional and structural uniformity along its thickness, which is aproximately 30 µm, may be observed in the micrograph which appears in Fig. 3.44.

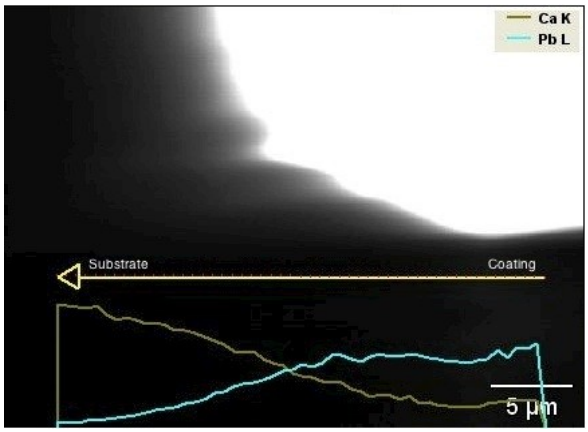

Figure 3.42: TEM image (CM30) of polished and thinned lead borosilicate sample comparing compositional profiles of Ca and Pb. The interface is a place around 5 microns of thickness around the compositional equilibrium point.

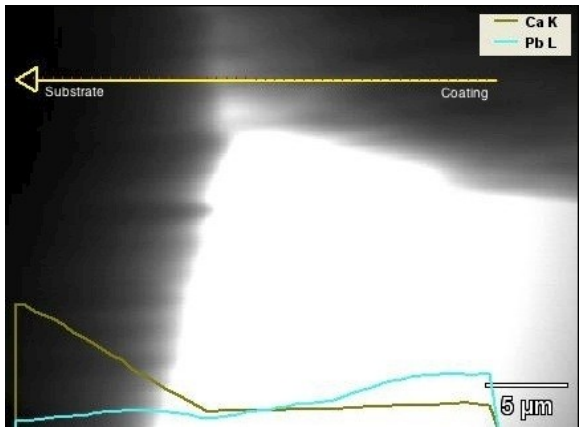

Figure 3.43: TEM image (CM30) of polished and thinned lead borosilicate sample comparing compositional profiles of Ca and Pb. The interface is a place around 5 microns of thickness around the compositional equilibrium point.

Fig. 3.44 is a collage of micrographs that illustrate a larger section of a sample, in order to ascertain the presence of irregularities on a minimum section of the coating-substrate interface. No crystalline phases were found in the observed coating, nor within the substrate layer. The fixing glue is labeled with a green point, while the coating is dark, and labelled with a blue point. An interface area is indicated with two parallel red lines and is consistent with a partial penetration of the organic glue (light contrast) into the coating (dark contrast), probably due to polishing and ion thinning effects.

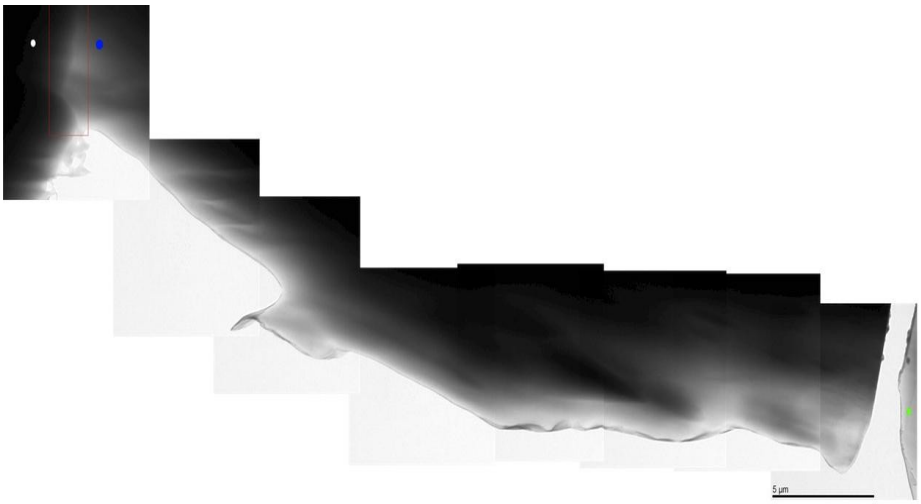

Figure 3.44: Composition of TEM images (CM30) of lead borosilicate sample along the thickness of the layer. The white point corresponds to the substrate, the layer is marked by the blue point and the glue has the green point. The red zone defines the interface place; which is an irregular straight line of light color. The thickness of this sample is aproximately 30 µm.

These studies also allow checking the appearance of interfaces; being a fusion process in which both materials are heat-treated, the interface is not linear; this could be corrected with a longer-in-time heat-treatment.

The lead borosilicate composition was doped with 5mol% Yb; in order to study the influence of the doping with functional Rare Earths. No significant difussion has been observed to take place from the coating into the commercial glass. However, it is observed that dopant-rich areas do not show a significant amount of Pb. Crystalline phases do seem to appear, however, as judged from the micrograph of Fig. 3.45, within the lighter contrast coating, where faceted phases of ca. 0.5 μm are easily identified. It should be considered whether this is due to a poor mixing of raw materials or driven by a particular thermodynamic process. Interdifussion processes between Ca and Pb were checked again; Pb and Yb are only appear within the guiding layer (Fig.3.46).

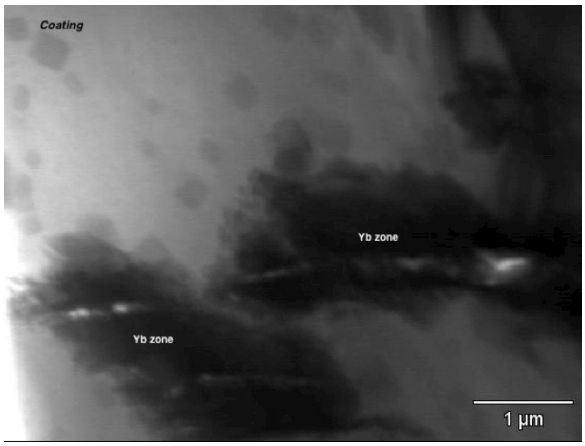

Figure 3.45: TEM (CM30) micrograph of a Yb-doped lead borosilicate sample. The heavier atomic weight element, Yb is found at the darker areas.

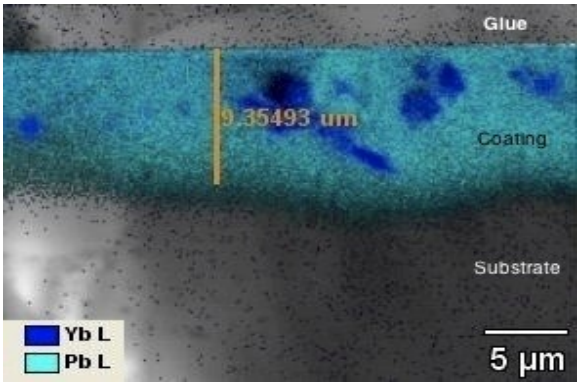

Figure 3.46: TEM image (CM30) of a Yb-doped lead borosilicate sample showing compositional maps of Pb and Yb. Moreover, at this area, variable thickness is observed due to a non-homogeneous deposition of the frit.

The basic lead borosilicate composition was treated by a CO_2 laser, resulting in melting of the inorganic oxide layer onto the commercial glass substrate; this study allowed to discover a minimum interdiffusion process as well as a thin interface which undergoes diffusion again but in a more defined fashion than the samples sintered by conventional melting. In addition, there is a higher surface regularity that favors the guiding of light through the lead layer with lower geometry losses (Figs. 3.47-3.48). The layers obtained by this method are thinner that those obtained by conventional fusion. Fig. 3.47 shows a micrograph corresponding to the interphase of a Pb borosilicate coating obtained on a soda-lime glass substrate using the LZM treatment described. The interface appears clean and uniform, with a sharp change in contrast between the coating (dark) and the substrate (light grey). A dilution type zone seems to appear at the interface (intermediate grey). In addition, darker spots appear along the substrate, which may indicate the presence of phases with different composition, in this case containing heavier elements than in the average glass composition. In Figure 3.48 we can observe how the interface between these materials, around 2 µm of thickness, is thinner than in the samples obtained by conventional melting; the amount of Pb is practically concentrated only at the coating, and the profile for the alkaline-earth element decreases suddenly after entering into the waveguide. The thickness of this coating, represented in Fig. 3.47 is just a

slightly higher than 5 μm. We must keep in mind that, in order to characterise this by TEM, a hole must be made in the face-to-face contact area, erasing some part of the coating. Since it is confirmed on Fig. 3.48, that the thickness of the coating in the same sample, but in another section of measure, is around 12 μm, a thick area for TEM sample preparation was thus conveniently selected.

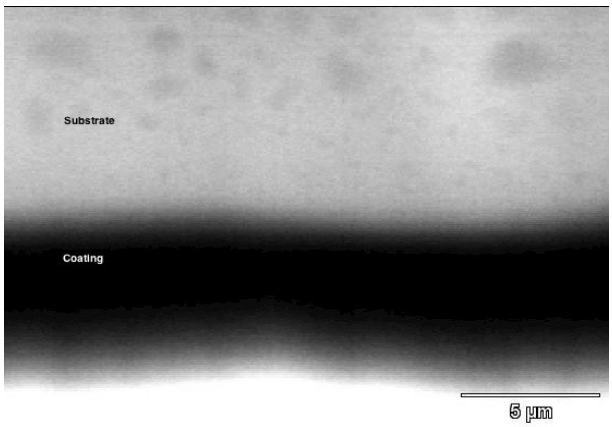

Figure 3.47: TEM (CM30) micrograph of a lead borosilicate sample coating obtained on a commercial glass substrate by LZM. The coating appears dark and with a relatively sharp interface, where essentially the heavier elements are expected to be exclusively present. The substrate appears to contain phases ca. 1 μm in size with heavier elements. A dilution type zone is identified at the interface. The thickness of this coating is just above 5 μm.

The presence of a SiO_2 grain, included within a lead borosilicate sample studied, has been confirmed by TEM, as shown in Figure 3.49. This is the only foreign phase found in microscope observations but no evidence has been found as to whether it is crystalline or amorphous in character. All samples were studied by X-ray diffraction in order to confirm the amorphous nature of the LZM processed coating (Fig. 3.26).

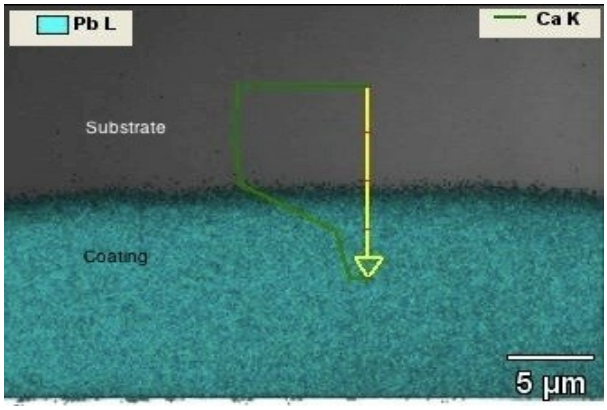

Figure 3.48: TEM image (CM30) of lead borosilicate sample treated by LZM combining Pb compositional map and Ca compositional profile. A minimum interface is present, and, therefore a minimum interdiffusion process ocurred between the coating and the substrate. A thickness around 12 µm is observed around this area of the sample.

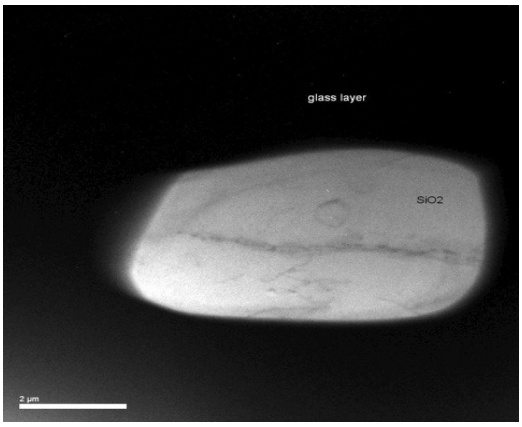

Figure 3.49: SiO_2 grain observed by TEM (CM30) and found within a lead borosilicate sample obtained by CO_2 LZM.

The lead borosilicate composition was also doped with Bi. The study of Bi-doped samples corroborated the minimum interdiffusion process observed when the coatings were treated by LZM. With respect to the dopant influence, the dopant is observed in a lower zone within the coating (Fig. 3.50). This factor should be studied in the future to clarify the reasons behind this phenomenon,

which may be related to the presence of denser Bi-O species within the directionally solidifying melt, as observed by Lennikov et al. [75] in the case of Ba-O coatings. The darker contrast of this area is due to the presence of heavier atomic weight elements, such as Pb and Bi, at the coating. Again, no evidence of the presence of crystalline phases was found.

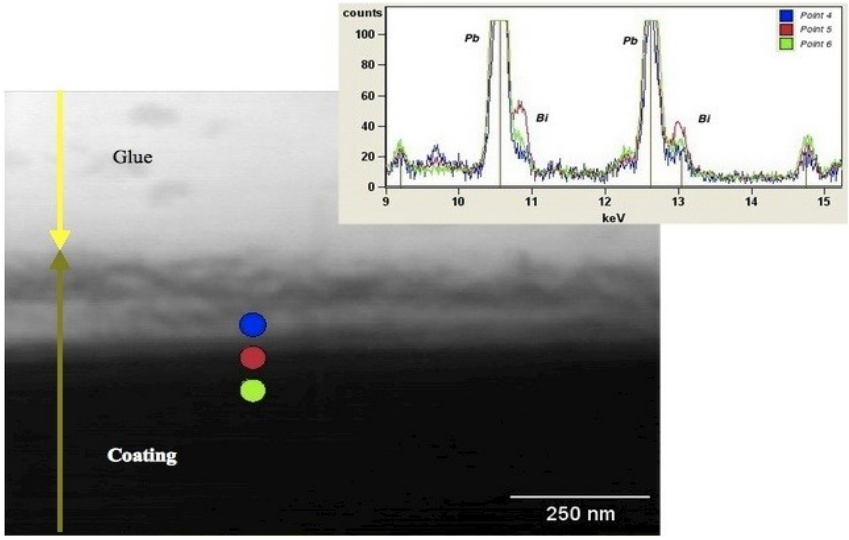

Figure 3.50: Combination of TEM image (CM30) and EDX spectra from a Bi-doped lead borosilicate sample treated by LZM. Three zones were analyzed within the coating interface to determine the distribution of Bi. It appears to be substantially concentrated in the area marked by the red dot. In the viccinity of the blue and green dots it s presence is much lower.

When the coatings are studied by UV-Vis spectroscopy, together with the commercial soda lime glass substrate, the observe spectra are essentially influenced by the coating composition and thickness. basically, we can talk about a commercial glass doped material. In effect, the spectra registered for the samples studied vary in percentage of light transmitted, as well as in the characteristic features related to their distinct composition. Fig. 3.51 depicts a an absorption peak at around 380 nm, already present as a characteristic of the substrate. The shape of the spectra for all samples registered. The lead (red) and the bismuth-lead borosilicate coatings practically have the same transmission

characteristics, showing an approximately a 5% increase in absorption with respect to the substrate. The inclusion of Yb causes a considerable (20%) increase in absorption with respect to the Bi containing coating, although the shape of the spectrum is essentially the same.

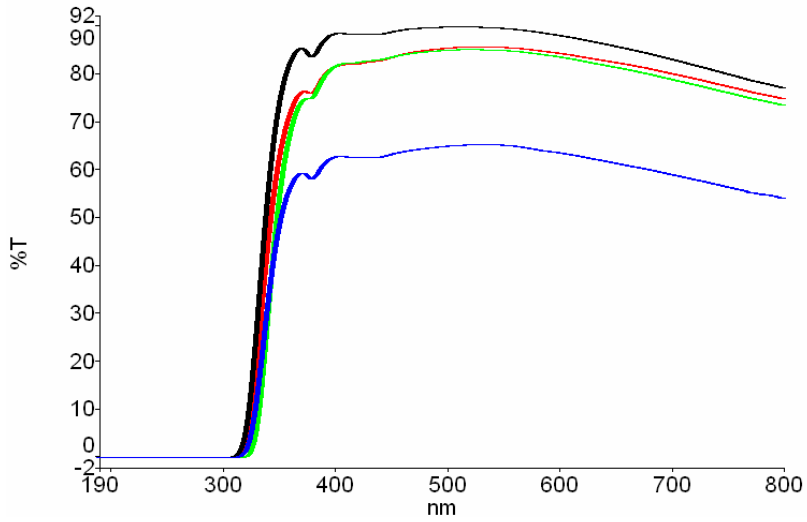

Figure 3.51: UV-Vis transmission spectra for commercial glass substrate (black), lead borosilicate frit coating (red), as well as coatings containing Bi (green) and Yb (blue).

Finally, illustration of the light guding capability of the materials obtained and described above, was achieved by using the direct coupling method described earlier in the experimental section of this text. Selective light guiding through a representative coatings, obtained on a commercials window glass substrate, is macroscopically demonstrated in Figs. 3.52-3.56. Figure 3.52 shows how a He-Ne laser beam, coupled with a 40x, NA 0.65 microscope objective, is preferentially guided through a planar lead borosilicate frit waveguide obtained by LZM.

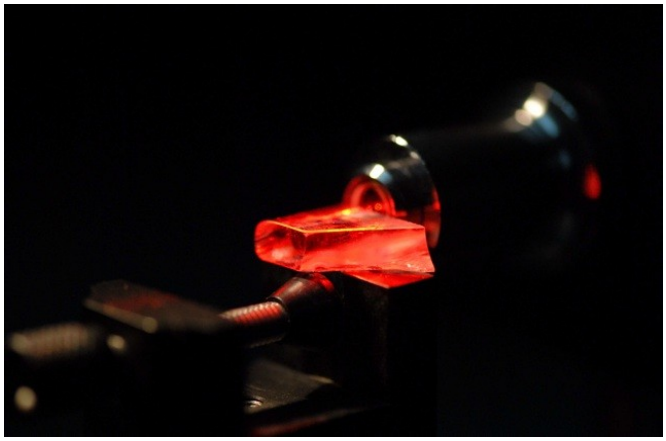

Figura 3.52: He-Ne laser beam, coupled with a microscope objective (40x, NA 0.65), guided through a lead borosilicate frit-derived, LZM processed coating .

The potential of attaining complex geometry waveguides structures was also explored. Thus, straight (Fig. 3.53) and curved line channels (Fig. 3.54) were prepared using mechanical and laser ablation machining methods, followed by furnace melting as described earlier (section 2.1.2)

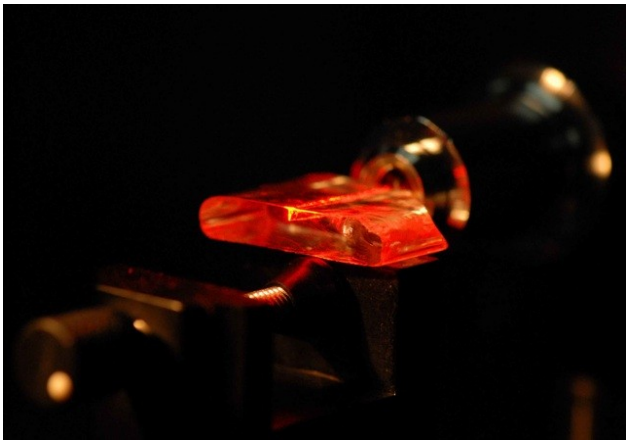

Figura 3.53: Photograph of a He-Ne laser beam guided through a straight channel mechanically engraved and coated with Pb borosilicate frit obtained by furnace melting.

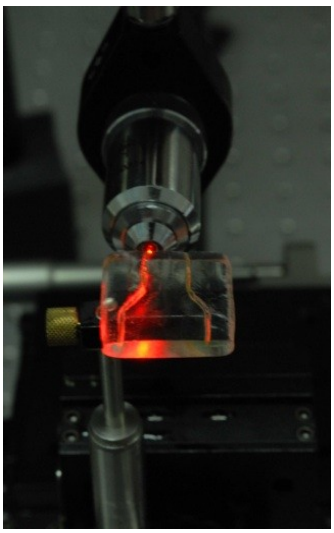

Figura 3.54:Photograph illustrating how a He-Ne laser beam travels through a curved line channel obtained by conventional machining on a commercial window glass, coated with Pb borosilicate frit and melted via conventional furnace heating.

An additional demonstration which is of interest for suggested potential integrated optical components is shown in Fig. 3.55. Here, the He-Ne laser beam initially coupled into a single straight channel guide is split into two, symmetrically disposed channels. The beam intensity appears to distribute as a function of beam coupling, so that further studies are necessary to develop techniques which may allow full control of light distribution amongst multiple channels. In any case, Figure 3.55 demonstrates the feasibility of the present method to prepare waveguiding structures where light may be steered in complex geometrical patterns. The structure shown in the Figure would represent a basic laser beam splitter component. The inserted photographs which appear on the bottom of the Figure correspond to enlarged views of the output beams. The left output beam suggests total confinement of light whitihn the channel waveguides, while the right output also exhibits scattering. The latter is probbably related to poor coupling of the entering beam.

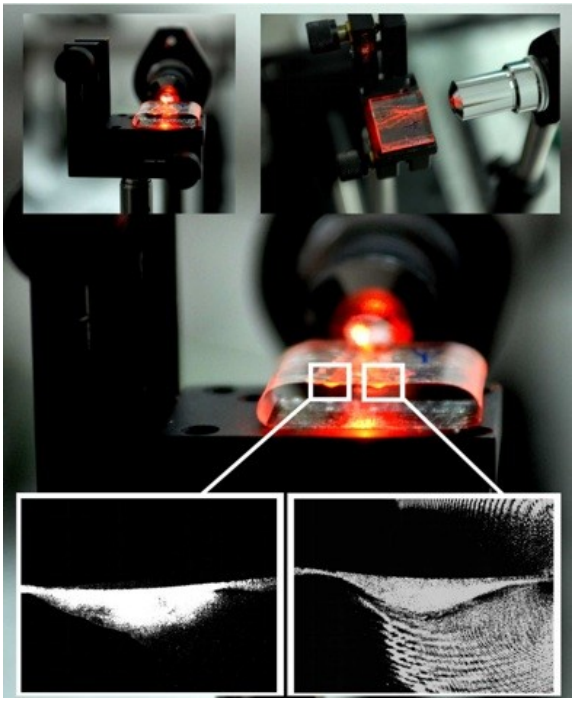

Figura 3.55: The laser beam light enters into the frit-derived guide coupled by a microscope objective and is bifurcated. The CCD images at the outputs confirm the confinement of the light and the subsequent guiding with similar intensity for both outputs. At the bottom of the figure we can observe two enlarged pictures, on the left side we can observe the light totally confined into the guide. On the right side the confinement of the light is also observed, along with additional scattering due to the experimental configuration presented.

An additional channel geometry explored is presented in Fig. 3.56. It is composed of a curved channel obtained by conventional machining, filled with Pb borosilicate frit and melted in a conventional furnace. The input He-Ne laser beam is coupled through the polished entry side, is confined along the curved path of the frit-filled channel, and exits intensely at a 90º angle through the output side the channeled glass substrate.

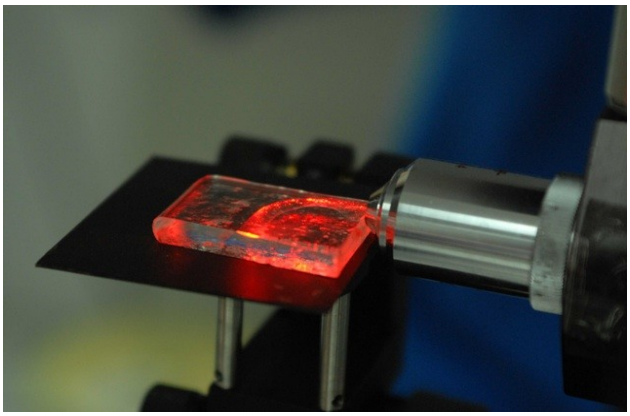

Figura 3.56: The laser beam light enters into a frit-filled channel prepared by conventional melting on a furnace after conventional machining. The input He-Ne laser beam is coupled through a microscope objective (40x, NA 0.65), follows the channel geometry and exits at a 90º angle.

In order to quantify the light guiding capability of the structures presented above, losses were determined by direct coupling of the light to the polished faces of the waveguides and measuring the input and output power measurements. In the case of the planar lead borosilicate waveguides, a value of 4.15 dB/cm for the attenuation coefficient. For the Yb-doped composition, the inclusion of the rare earths appears to increase waveguide efficiency, yielding a value of 3.04 dB/cm for the attenuation coefficient. Both of these samples were approximately 10 μm thick.

3.3 Laser Ablation Backwriting of Metal Targets

Channel waveguides deposited onto microscope slides and commercial glass substrates by laser ablation backwriting (LAB) of metal targets were studied by transmission electron microscopy in order to contribute to the understanding of the phenomena involved in the LAB structures reported by Rangel-Rojo et al. [29] and Castelo et al. [30]. Microstructure (SEM) and electrical conductivity were studied on coatings derived from selected metal targets measuring 50x4 mm^2. Finally, coatings with similar dimensions were also studied, after acid cleaning by SEM and UV-Vis spectroscopy, in addition to their initial waveguiding characteristics.

LAB modified glass substrates were obtained using three different kinds of metal targets. Both, laboratory glass slides and window commercial glass substrates were initially evaluated. The results obtained from this initial evaluation indicated a similar behavior amongst both types of soda-lime type glasses. For this reason, laboratory glass slides were selected to continue this study further.

Initial TEM studies centered on the Ag derived waveguides, as exemplified by the micrograph shown in Fig. 3.57. This micrograph corresponds to a glass slide obtained by LAB using a silver metal foil as a target. The unaffected substrate (right), the affected substrate surface (center, delimited by red lines) and the glue used for sample consolidation (left) are observed in the micrograph. The dark contrast, corresponding to Ag particles, indicates the presence of a well-defined, inner affected layer-like arrangement of Ag in a direction parallel to the substrate surface. Three layers of Ag particles are easily observed within the affected substrate inner surface and with Ag particles ranging in size between ≈10-100 nm. Larger size particles tend to appear towards the outer surface of the substrate.

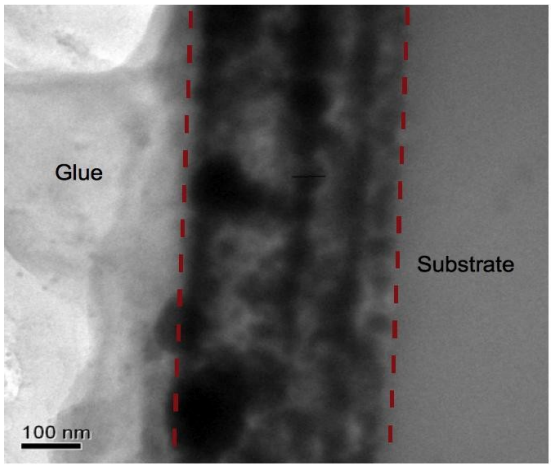

Figure 3.57: TEM (CM30) micrograph of a microscope glass slide modified by laser backwriting using a silver metal target. The unaffected substrate (right), the affected substrate surface (center, delimited by red lines) and the glue used for sample consolidation (left) are observed in the micrograph. The dark contrast, corresponding to Ag particles, indicate the presence of a well defined, inner affected layer-like arrangement of Ag in a direction parallel to the substrate surface. Three layers of Ag particles are easily observed within the affected substrate inner surface and with Ag particles ranging in size between ≈10-100 nm. Larger size particles tend to appear towards the outer surface of the substrate.

A 150 nm modified substrate surface layer is shown in Fig. 3.58, where silver particles, initially present on the outer part of the substrate, appear to have been removed into the glue by the sample preparatory etching process. The latter suggests a significant general effect of the etching process on the metal channels initially formed by laser backwriting, where metal particles are moved away from the position where they were deposited by irradiation. Fortunately, these positions may be deduced from the voids left behind, observed as white contrast areas on the right side of the red dotted area within the micrograph of Figure 3.58.

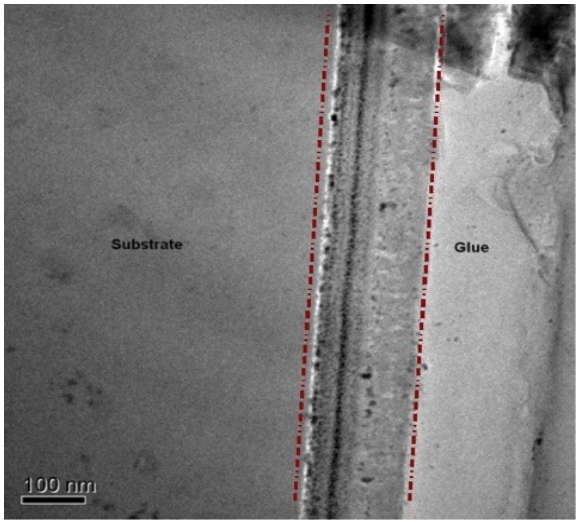

Figure 3.58: TEM (CM30) micrograph of a microscope glass slide modified by laser ablation backwriting (LAB) using a silver metal target. The original substrate, its modified area (delimited by discontinued red lines and formed by layers of metal particles incrusted into the glass matrix) and the glue used for consolidation during sample preparation are indicated in the micrograph. The dotted red line on the right represents the outer surface of the glass substrate. The Ag nanoparticle track is approximately 80-100 nm inwards into the substrate and could thus be viewed as a "burried waveguide".

In contrast, the dark contrast line onserved in the same area, near the substrate, indicates that a large, uniform accumulation of Ag takes place at the cost of diffusion into the glass substrate. This diffusion, found below >100nm in Figure 3.58, must be a consequence of a pronounced photothermal laser irradiation effect associated to the 20-200 ns range pulse applied. A pausible explanation for this effect would take into account (a) an initial backwriting ablation process whereby Ag metal particles are ejected from the metal foil target and projected onto the glass substrate; (b) an intermediate follow-up process which entails direct laser heating of particles deposited onto the glass surface, and (c) heating of the glass surface by hot Ag particles, which cool and diffuse simultaneously into the cooler inner volume of the glass substrate. These processes would be consistent with the appearance of the multiple Ag layers observed in Figs. 3.57 and 3.58 for the outer substrate surface. In fact,

subsequent layers become less uniform as expected from the initial Ag deposited partially absorbing the incoming laser radiation and consequently blocking the new outer Ag layers formed on the glass surface exposed to the plasma plume, as well as the metal foil target. The Ag nanoparticle track is approximately 80-100 nm inwards into the substrate and could thus be viewed as a "burried waveguide".

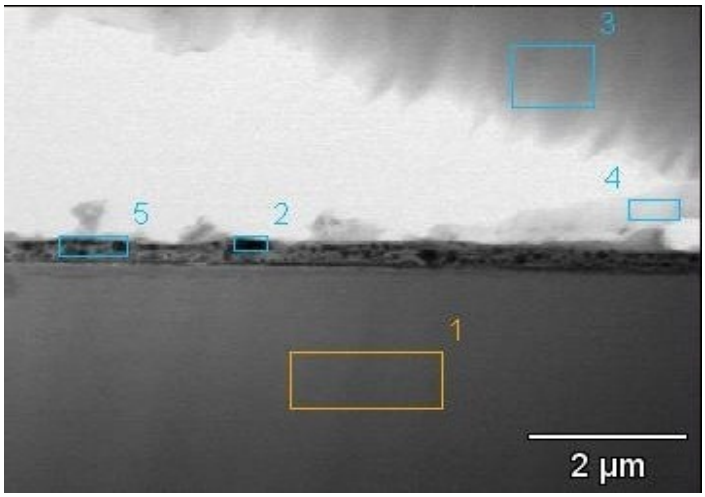

Figure 3.59: TEM (CM30) micrograph of a polished and thinned silver sample and the corresponding areas for the EDX analysis. One channel is observed at the center of the micrograph, and can be distinguished from the substrate because of the darker contrast of the silver nanoparticles, associated to its heavier atomic weight with respect to the that elemnts present in the commercial glass substrate.

The EDS analysis of a typical Ag laser backwritten sample was obtained in order to identify the different zones containing Ag and marked in Fig. 3.59. The spectrum of the inner substrate areas is shown in Figure 3.60 and contains peaks which correspond to the elements typically presented in soda-lime glasses. Figure 3.61 shows the spectrum corresponding to the substrate surface areas affected by the LAB of a Ag target. These spectra exhibit high intensity signals associated to the presence of silver particles, confirmingtheir presence at the substrate surface. Finally, the intense C and O signals appearing in Fig. 3.62

corroborate the presence of C and O containing species within the glue employed for sample consolidation. The Na and Si peaks originate in part from the presence of glass particles incorporated into the glue section via the etching process.

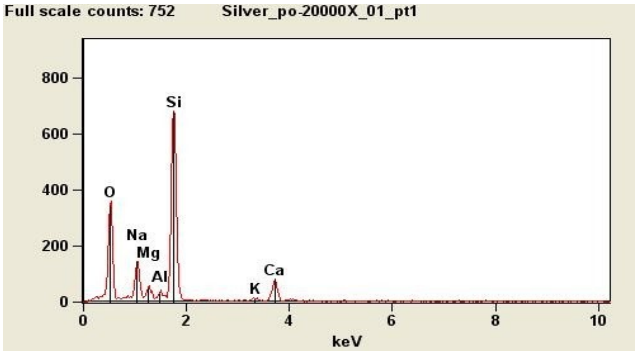

Figure 3.60: EDS spectrum of the substrate, corresponding with points 1 and 3 in Fig. 3.59, showing the typical composition for the commercial soda lime glass.

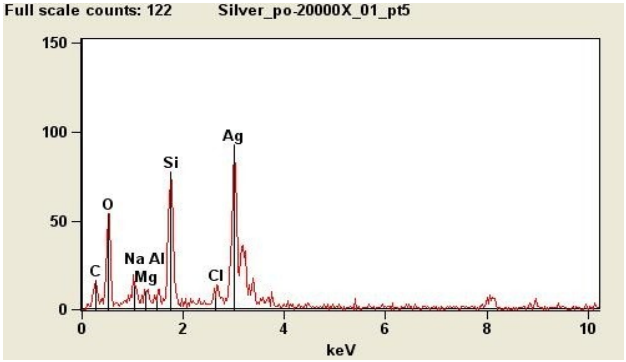

Figure 3.61: EDS spectrum of the metal layer, corresponding with points 2 and 5 in Fig. 3.59, confirming the presence of Ag on the surface of the substrate, specifically, within the LAB affected area. Although the presence of the elements which typically form commercial soda lime glass is observed along with Cl. The latter probably appears as a consecuence of contamination during TEM sample preparation.

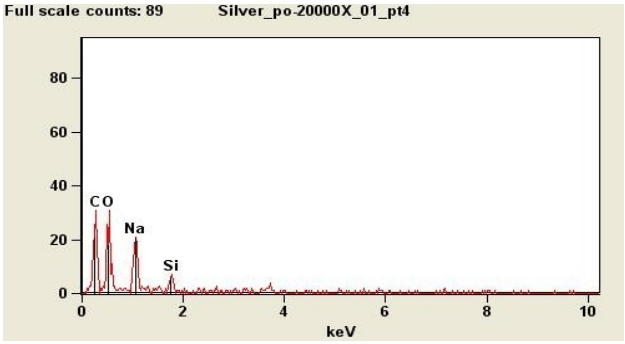

Figure 3.62: EDS spectrum of the glue area, corresponding with point 4 in Fig. 3.59. The high percentage of C and O originate from species present as a components in the glue.

Another LAB target studied was 63Cu37Zn, a typical commercial brass alloy. The micrograph shown in Fig. 3.63 exhibits a layer of metallic particles encrusted into a glass matrix, limited by two parallel discontinuous lines displayed in this figure. Particles of a large size (tens to hundreds of nm) appear on top of the laboratory glass slide substrate closer to the glue. The etching process is held responsible of the damage observed on the substrate, characterised by the discontinuity along the upper diagonal discontinuous line drawn in the figure.

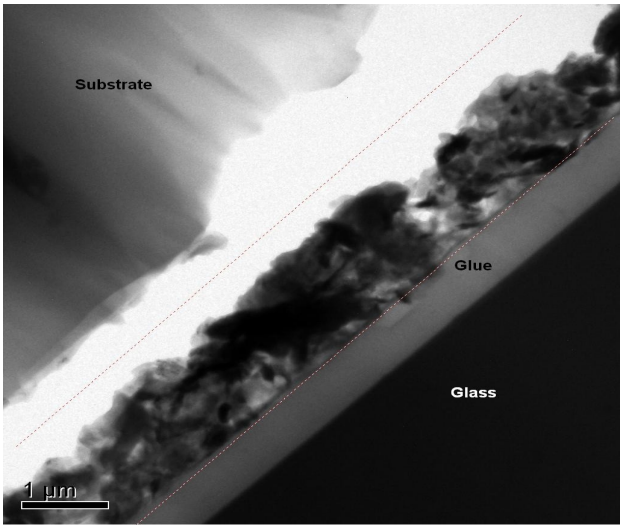

Figure 3.63: TEM (CM30) micrograph of a 63Cu37Zn commercial alloy derived glass substrate coating. Two parallel discontinuous red lines indicate the approximate limits of the LAB modified zone or coating; the hollow area which appears at the interface between the coating and the substrate is due to ion etching, performed during sample preparation for TEM observation. Particles with a widespread size distribution, ranging between tens and hundreds of nm, are observed on the area near the glue section on top of the glass substrate.

The results obtained from EDS analysis, for a sample arranged in a confronted substrate configuration, are given in Figures 3.64 and 3.65. The presence of copper is detected by EDS analysis on area number 4 in Figure 3.64. This area corresponds to the substrate surface. Areas 1 and 2 within the figure denote glass substrate zones which are apparently unaffected by laser irradiation and whose composition corresponds to that of the original glass substrate. The zone around the glue, also analysed by EDS, is identified as area 3 and is found to be essentially composed of C. No EDS signal for Zn can be detected in any of the zones, suggesting that it has been eliminated during the etching process applied for TEM specimen preparation.

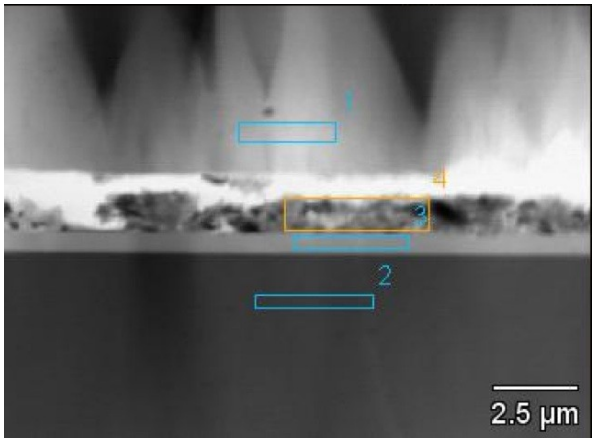

Figure 3.64: TEM (CM30) micrograph of a 63Cu37Zn alloy sample in a face-to-face configuration. Areas where EDS analysis was performed are identified with numbered rectangles. Glass substrate areas are noted by rectangles 1 and 2, while rectangle 3 is located within the glue zone. The layer formed by metal particles embedded into the glass substrate corresponds to rectangle 4.

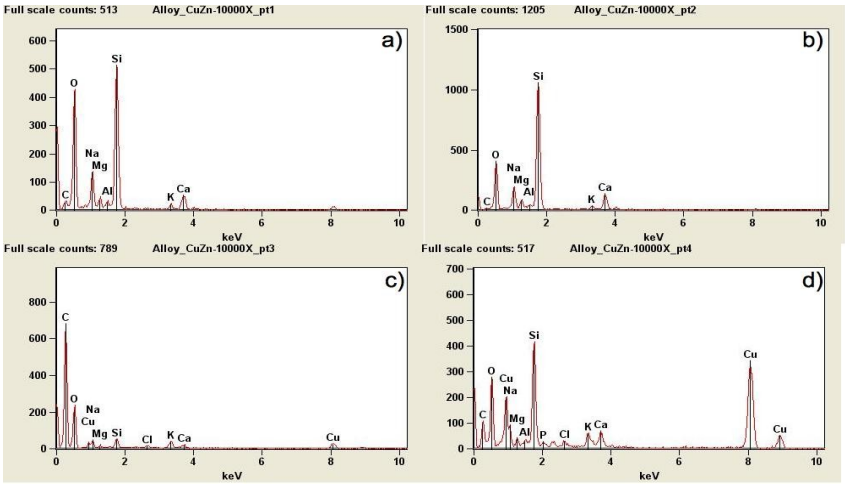

Figure 3.65: EDS analysis of the rectangular areas marked in Fig. 3.64 where a) and b) mark substrate areas (rectangles 1 and 2) and correspond to the typical spectrum obtained on the unaffected glass substrate. Spectrum c) corresponds to the sample joining glue (rectangle 3), where a very low signal for Cu is observed. Spectrum d) corresponds to the coating deposited by LAB and confirms the presence of a considerable amount of Cu (rectangle 4).

The presence of elemental copper particles was confirmed by electron diffraction analysis, where the electron diffraction pattern observed correlates well with the data reported for fcc Cu (Fig. 3.66) [175-176]. As shown in Figure 3.65, four diffraction peaks were registered. This peaks correspond to diffraction peaks of Cu crystals with indices {111}, {200}, {220} and {311}. The {111} reflection peak is typical of single crystal fcc Cu, while the {200} reflection is observed when the material contains small crystals with the fcc structure [175-176]. The peaks for {220} and {311} reflections were also observed, but with lower intensity, as reported by Germer et al. [175], who registered these four peaks for Cu/Zn alloy samples. This means that the original 63Cu37Zn brass alloy substrate was decomposed during the ablation process into its constituents. Zn remains at or near the surface of the glass substrate and may be removed by the polishing and etching processes applied during TEM specimen preparation, as will be confirmed by FE-SEM observation.

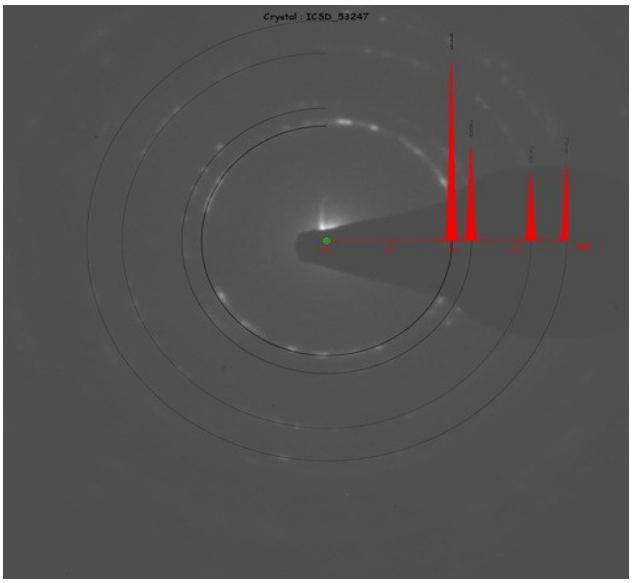

Figure 3.66: Electron diffraction pattern of 63Cu37Zn alloy confirming the presence of crystalline copper particles, by comparison with the calculated diffraction pattern of pure Cu, shown in red. The electron diffraction pattern observed correlates well with the data reported for the diffraction pattern of fcc Cu. Four diffraction peaks were registered corresponding with the {111}, {200}, {220} and {311} Miller indices of de fcc structure.

The last type of sample studied by TEM were based on Al target LAB. This metal is not expected to remain in its elemental state after passing through an intense ablation plume, as it readily oxidises under very mild conditions in contact with air. It is also expected to react with the oxide components present in the glass substrate, since Al excited species should be hot and very reactive as they impinge onto the substrate surface when ejected from the plume generated by the ablation. Electron diffraction studies do not indicate the presence of any crystalline particles of Al, suggesting that it has been incorporated into an oxide glass phase. This is consistent with its mentioned level of reactivity. In fact, Al species should diffuse into the substrate as glass-former components. Consistently with these arguents, no particles were found dispersed within the substrate near its ablation-affected surface, as observed in Figure 3.67. In this figure, the bright spots correspond to voids originated at the etching, while the grey contrast delimited by two parallel discontinuous lines, within a ca. 100 nm width, is characteristic of the presence of lighter elements, consistent with an enrichment of Al. Observation of the affected area also suggests that Al diffuses into the substrate gradually, up to about 50 nm further.

EDS analysis of this sample (Fig. 3.68) clearly establishes the presence of Al. This figure shows a micrograph marked with a point (1) and a rectangular area (2) where an EDS linescan analysis was made to sudy whether the Al amount was higher near the surface directly affected by the laser backwriting ablation plume. The EDS spectra shown on the right side of the figure confirm the presence of Al within the affected surface. Not only the signal for Al in the spectrum (b) corresponding to the rectangular area (2) is higher than in the spectrum corresponding to point (1), but, except for Si, the rest of the elements such as Ca, Mg, K and Na are also present in much lower amounts. Moreover, the peaks corresponding to Si and O appear proportional in all samples studied, consistent with the presence of an Al-containing or enriched Si-O glass phase. The peak intensity differences observed suggests that Al-enriched glass phase is etched under mild conditions easier than the original unaffected substrate glass. This is the reason for the appearance of the voids within the ablation affected substrate area observed in Fig. 3.67.

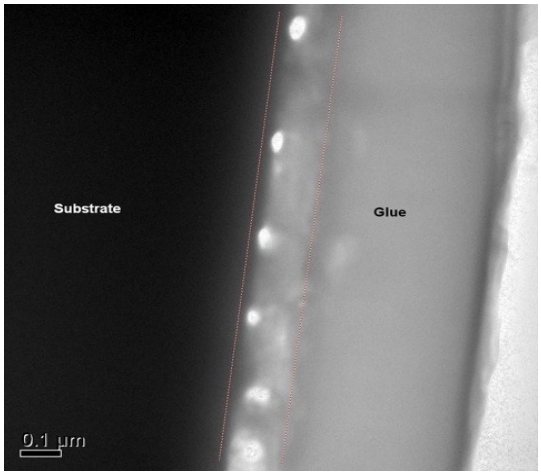

Figure 3.67: TEM (CM30) micrograph of one sample obtained by LAB of Al targets. The Al layer is indicated by two discontinued red lines. Several holes are visible near the surface of the substrate. Light contrast particles are found in this layer, as expected from the reactivity of Al with oxides, in this case expected to form an amorphous phase with soda-lime glass.

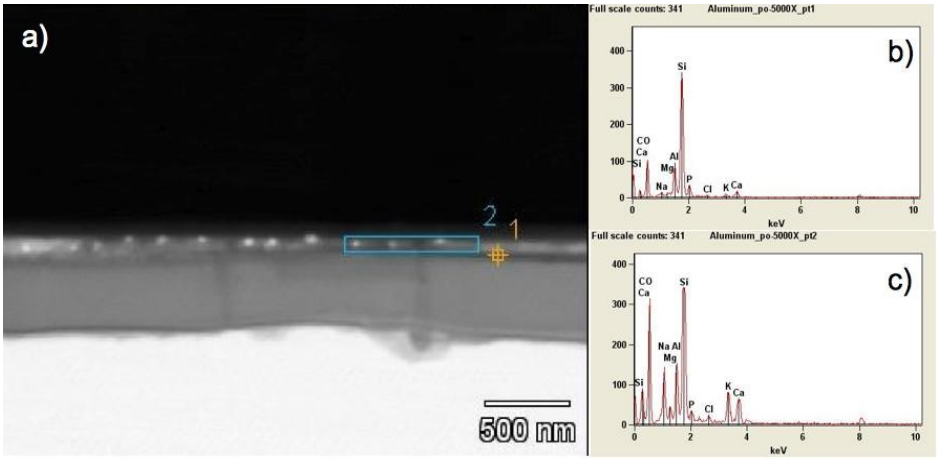

Figure 3.68: TEM (CM30) micrograph of an Al sample and the corresponding EDS analysis. b) corresponds to a position near the interface between the modified layer and glue (point 1), and c) delimits the layer area between the glue and the substrate (rectangle 2). Higher amounts of Al appear in zone 2, as the Al species ablated react with Si components in the glass to form an amorphous phase.

Extended EDS line scan analysis was obtained on a representative Al LAB derived sample, as shown in Figure 3.69, where a micrograph of the sample appears with the elemental linescans adequately indicated (a) with colour codes. The corresponding spectra are given in the same Figure (b), where three of the colour codes may well be emphasized and commented ahead. The white code corresponds to Si, the red one to O and the yellow one to Al. Figure 3.69 (b) is quite explicit indicating an increase in Si, Mg and Al during the first ca. 34 nm, from the outer surface of the affected substrate. After a plateau of approximately constant composition within the following ca. 17-34 nm, while that of Al decreases to a minimum. The Al particles are geometrically distributed in the direction coincident with the movement of the laser during the LAB. EDS demonstrates the existence of a maximum in Al concentration within this ca. 60 nm wide line. Thus, laser ablation backwriting of Al targets provides inner waveguides at the substrate; these types of photonic structures are known as 'burried waveguides' in the literature (Fig. 3.70) [10, 155].

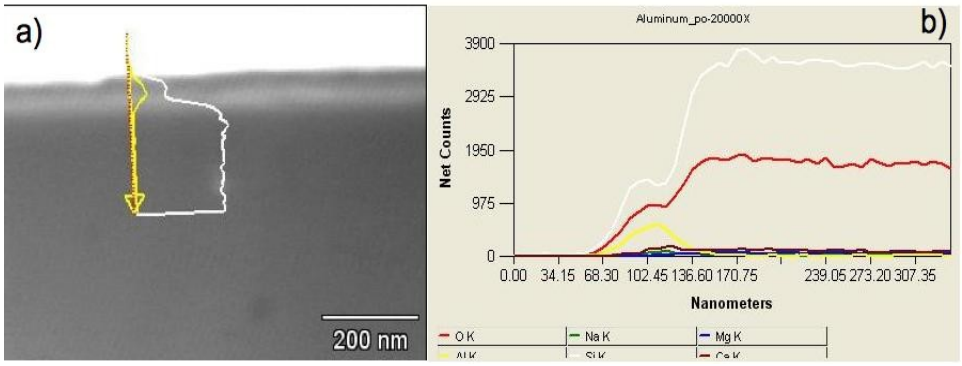

Figure 3.69: TEM (CM30) micrograph of an Al modified layer and the corresponding EDS linescan analysis. The white and red spectra correspond to the signals of Si and O, respectively; while the signal of the Al is drawn in yellow. The spectra of other species such as Na, Mg and Ca, contained in the commercial glass composition, were also registered (green, blue and violet lines, respectively), however, their signals are much less intense.

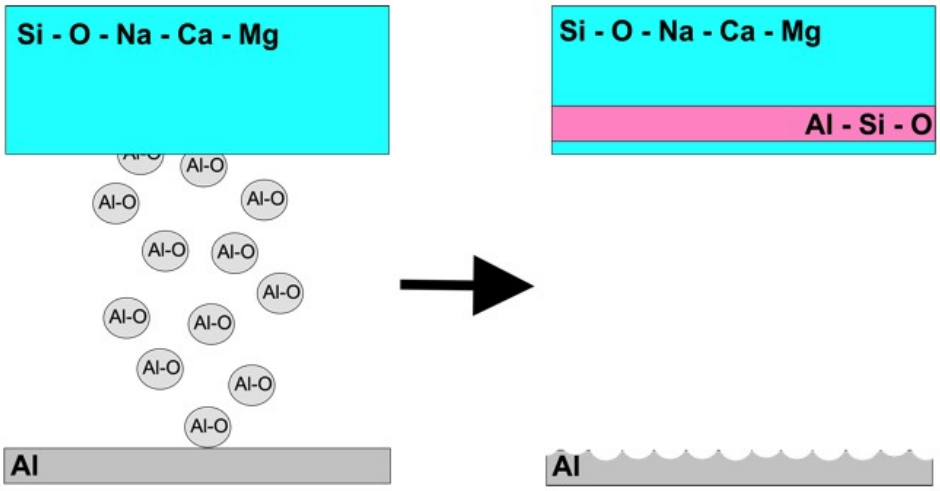

Figure 3.70: Scheme of the Laser Ablation Backwriting (LAB) process over Al targets. The beam of the laser is focused on the metal plate, inducing formation of a plasma plume containing excited species. The high reactivity of the Al promotes the formation of "Al-O" excited species, which are incorporated into the glass substrate. Through a diffusive process, an inner Al-enriched zone is formed within the glass substrate, coincident with the movement of the laser beam. This zone or band, formed by aluminosilicates with a different refractive index than the substrate glass, induces the in-situ formation of a "burried waveguide" inside the substrate and away from its outer surface.

FE-SEM studies of LAB coatings allowed determining their thickness. In addition, they were useful to ascertain the effects produced by the use of different atmospheres during LAB. Particularly, air and high vacuum environments were explored. As deposited and acid etched samples were evaluated and are discussed ahead.

Starting with Al LAB experiments in both, air and high vacuum conditions, considerable differences were observed. A layer of aluminosilicates is formed on the substrate with a thickness ca. 600 nm when LAB is performed in air. This is in agreement with the TEM results discussed previously. Moreover, at the Figure 3.71 exhibits a coating with a tilted, strongly directional cone-type morphology. Such surface microstructure derives from the directional ablation process suffered by the metal target, which induces deposition on the glass substrate following the parallel line beam scanning paths described by the laser. The

periodicity is related to the pulse/scan rate relation and thus to pulse overlap during the LAB process. Moreover, based on previous works [29-30, 89-90, 114], this tilting angle is apparently directly affected by the ablation process conditions and consistent with the above explanation.

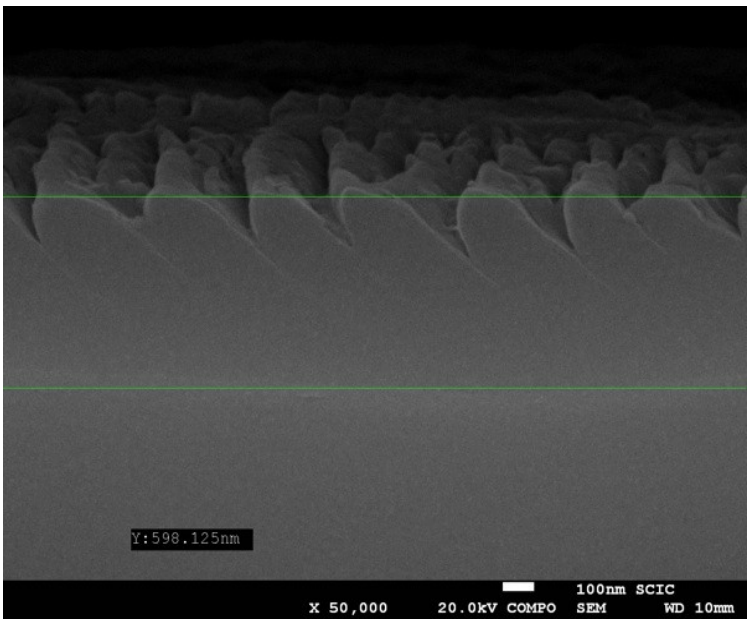

Figure 3.71: SEM micrograph of an Al waveguide fabricated in air. The guide area is denoted by green lines and its thickness is ca. 600 nm. Laser irradiation generates intense laser ablation plume, accompanied by intense shock waves. These cause the ablation plume to generate deposits in the form of the observed cone pattern, tilted in one direction because of the linear scan of the laser beam.

A closer examination of Figures 3.71 and 3.72, allows to identify a darker zone at the top of the glass substrate, corresponding to the presence of Al, as was confirmed by compositional EDS analysis and giving in Table XXVIII. Within this area, the presence of Al twice that found within the commercial glass substrate.

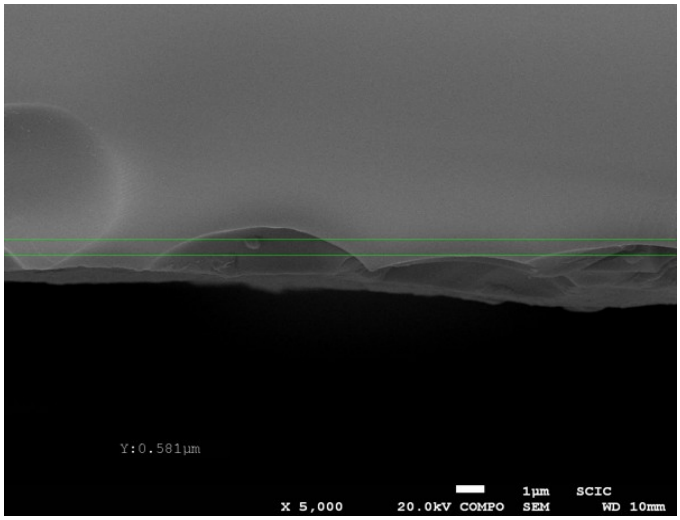

Figure 3.72: SEM image of an Al coated substrate fabricated under high vacuum conditions using LAB. The affected volume is enclosed by the darker area denoted by green lines and its thickness is ca. 600 nm.

Table XXVIII: Atomic percentages of K line compositional analysis performed at the substrate, far away from the surface, and in the darker areas near the surface after Al LAB and corresponding to the sample shown in Figure 3.71.

Atom %	***O k***	***Na k***	***Mg k***	***Al k***	***Si k***	***Ca k***
Substrate area	73.5	7.65	1.69	0.38	15.4	1.35
Coated area	75.2	7.14	1.70	0.69	14.0	1.17

At this point, air and vacuum environment, as obtained LAB samples (without acid cleaning) were observed. Both type of samples present a thick layer of particles deposited from the metal target. Those metal particles ablated in air are supposed to suffer oxidation during the process (Fig. 3.73). This fact is corroborated by the EDX analysis of the areas denoted by numbers at the figure 3.73. The results of the quantification of materials are summarized at Table XXIX.

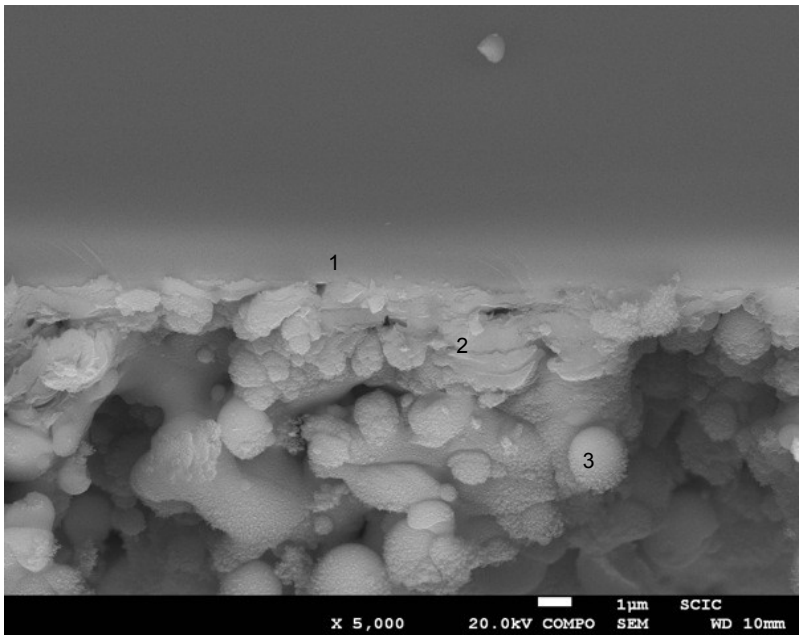

Figure 3.73: SEM micrograph of a polished and thinned Al derived deposit prepared in air. Point 1 marks the Al zone on the top of the substrate (lighter contrast due to its low atomic weight), while point 2 denotes the metal particle coating and 3 corresponds to a spherical Al-containing particle.

Table XXIX: Compositional analysis of Al derived coating shown in Fig. 3.73.

% Atomic	***O k***	***Na k***	***Al k***	***Si k***
1 - Guide	53.25	7.20	14.71	19.84
2 – Coating	27.16	1.00	50.78	2.69
3 – Spherical particle	40.96	0.92	56.66	1.47

Figure 3.74 shows a micrograph of the Al containing spherical particle, which presents a surface covered by smaller, submicrometric particle debris originating in the LAB process. The appearance of this spherical particle adhered on the coating is consistent with the expected mechanism of ns regime laser ablation, where molten Al-O species (indicated in Fig. 3.70) are formed in-situ above the metal and in contact with air, and transported through the plume

into the susbtrate above. The spherical geometry is typical for substances which undergo melting and their shape is conroled by surface tension forces. Their presence confirms melt drop formation and shock wave driven expulsion from the surface of the metal target during LAB [88, 93]. When the laser backwritting process is performed under high vacuum conditions (Fig. 3.75), the resultant coating morphology is considerably different from the one obtained in air (Figs. 3.73 and 3.74), but EDS analysis was unable to distinguish between the Al meatl and its corresponding oxide on the surface of the coated substrates, oxidation processes are apparently avoided during LAB, since it was observed that the outmost surface of the coating had an Al-like metallic appearance. The Al metal particles which enter the volume of the glass substrate, however, are expected to form aluminosilicate products, as proposed in Figure 3.70. In any case, measurements are presently underway using alternative characterisation methods to improve the understanding of this process.

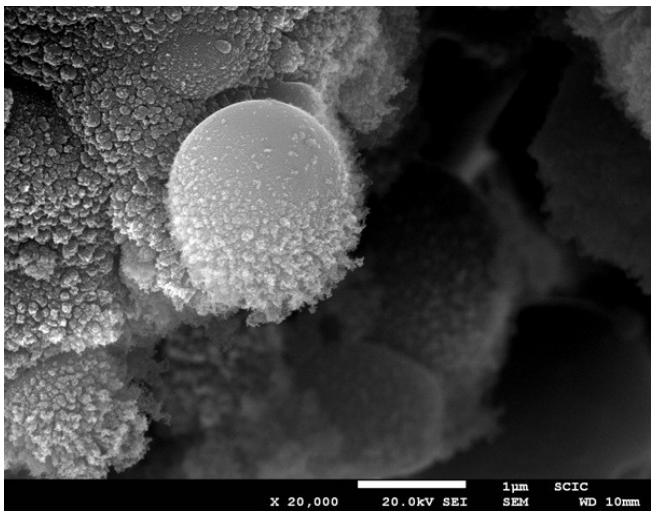

Figure 3.74: SEM micrograph of the Al-O balloon particle coated by oxidized aluminium submicron particles at surface.

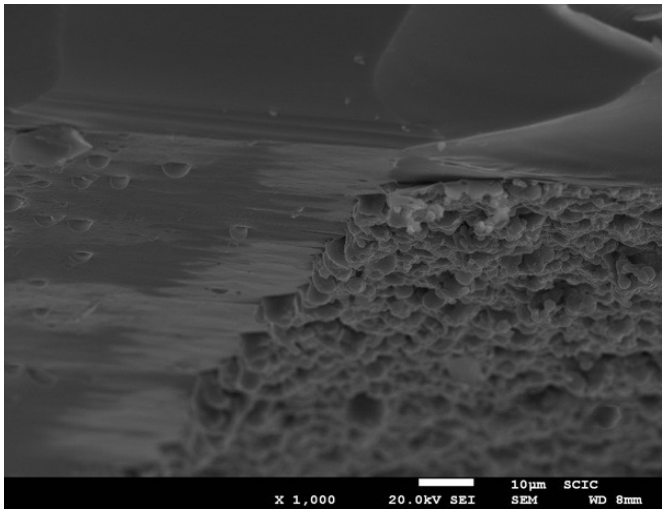

Figure 3.75: SEM micrograph of Al-like metallic coating (right side) deposited by LAB under high vacuum conditions on top of a commercial glass substrate.

The surface morphology observed for the vacuum LAB of Al targets (Fig. 3.76) appears considerably different from that observed for the similar experiments carried out on Al targets in air (Fig. 3.71). The morphology attained under vacuum conditions apparently exhibits much lower surface roughness and seems to be composed of molten plates which adhered to the glass substrate, as observed in Fig. 3.76. This would be an indication that a relatively lower viscosity liquid or melt has been present during ablation and deposition, suggesting the presence of molten Al metal (m.p. 660 ºC), as opossed to molten Al_2O_3 droplets, whose melting point is ca. 2050 ºC.

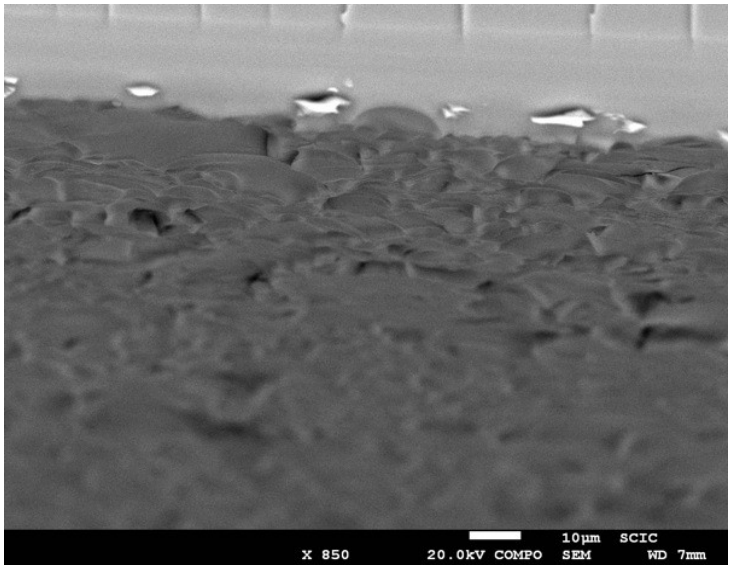

Figure 3.76: SEM micrograph of a LAB Al target modified microscope slide glass substrate after acid cleaning. The process was performed under high vacuum conditions.

The second class of LAB samples studied by SEM were based on the use of 63Cu37Zn brass targets. In this case, SEM allows observing particles included into the glass substrate, in agreement with previous TEM studies. After the sample was cleanned with acid, SEM studies confirm the appearance of holes within the upper part of the coated substrate, suspected to arise from the previous presence of incrusted particles removed by acid etching (Fig. 3.77).

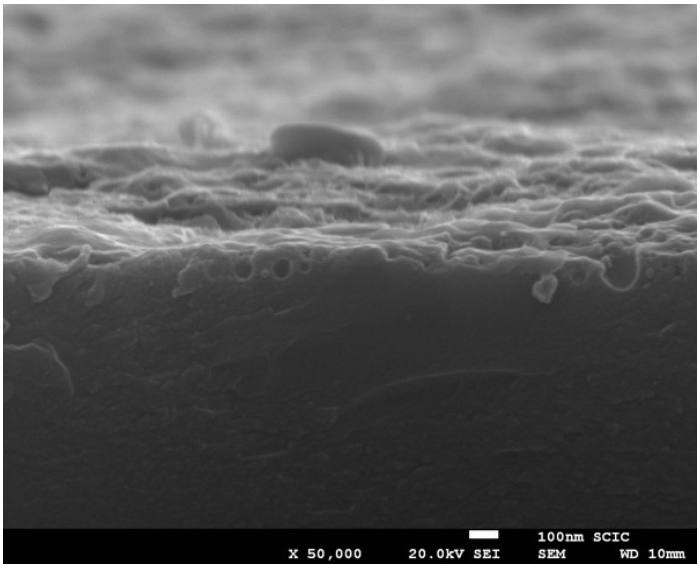

Figure 3.77: SEM micrograph of the surface of a brass waveguide sample after cleaning with acid. Holes are observed within the upper zone of the glass substrate.

Through the EDS analysis of the brass derived LAB could help improve understanding of the coating process. The normal percentage of elements in commercial brass Cu:Zn is 63:37, corresponding to a Cu/Zn ratio of 1.70. Compositional analysis of metal incrusted particles is useful to determine how the amount of Zn changes as a function of coating depth, without the influence of etching. A detailed FE-SEM study was thus carried out on unetched LAB brass samples. Fig. 3.78 shows a micrograph of a back-written coating on a glass substrate, obtained from ablation of a brass target. The points indicated on the micrograph were analysed by EDS and are collected in Table XXX (EDS). The Cu/Zn ratio, as well as their elemental content, change as function of depth into the glass substrate. The Cu/Zn ratio increases as function of depth. In fact, Cu remins deeper into the substrate, even when the Zn is not detected. On the one hand, this fact confirms the elimination of the Zn with the ionic etching applied during TEM samples preparation. On the other hand, Cu appears included deeper into the substrate, possibly because it is much less reactive or chemically compatible, with the glass matrix than Zn. The latter is knwon to easily incorporate into glass sompositions and it is even used widely in the ceramic

glaze industry as an opacifier [60]. Similar results are observed in samples made under high vacuum conditions.

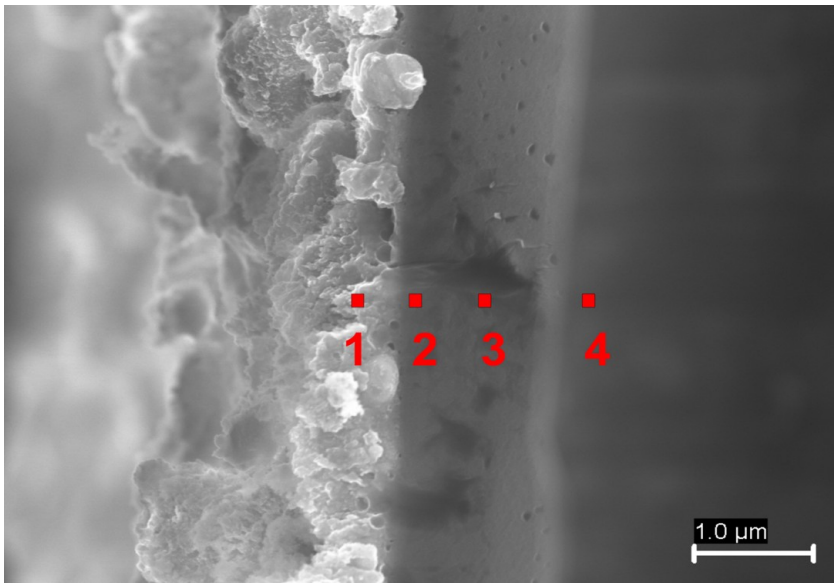

Figure 3.78: FE-SEM micrograph of a 63Cu37Zn sample, obtained by LAB under air conditions on a microscope slide, where selected areas for compositonal analysis are marked and numbered in red.

Table XXX: EDS analysis of areas marked on Figure 3.78.

Area	% Si	%Cu	%Zn	Ratio Cu/Zn
1 (coating)	16.33	1.25	0.36	3.47
2	18.07	0.50	0.12	4.17
3	21.93	0.09	0.00	-
4 (glass)	24.30	0.00	0.00	-

Figure 3.79 represents a 63Cu37Zn sample made in air without further processing. Three different zones are clearly observed on the sample, in parallel with the Al samples studied (Fig. 3.73). Fig. 3.79 shows a metal particle deposit (ca. 400 nm) adhered to the coating (ca. 350 nm), which in turn is well integrated into the glass susbtrate. These are respectively located in the upper,

middle and lower part of the micrograph. The LAB generated coating section appears uniform and integrated into the substrate through a sharp interface.

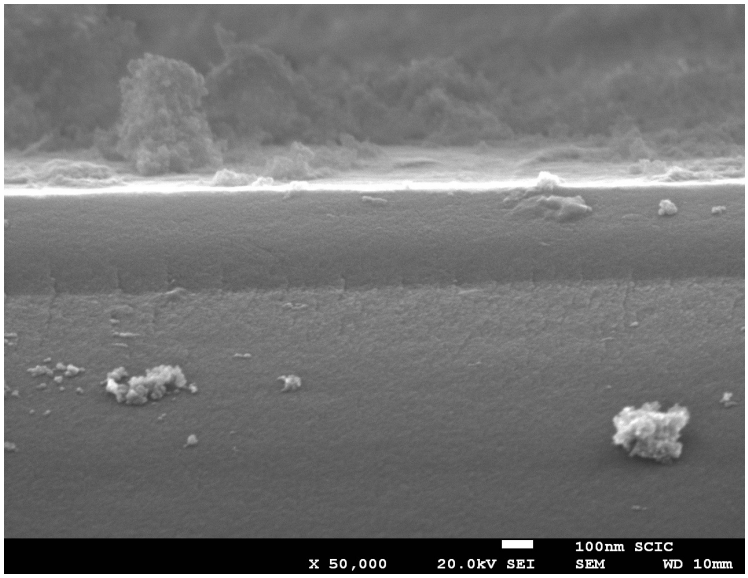

Figure 3.79: SEM micrograph of a 63Cu37Zn sample obtained by LAB. We distinguish a metal particle deposit (upper), a coating zone (darker zone at top of the substrate) and the susbtrate (clear). Some dust particles are present on the surface viewed.

The brass derived metal particle coating obtained under high vacuum conditions appears to be made of compacted particles and with different morphology than the one obtained in air, as judged from the micrograph shown in Fig. 3.80. In any case, the same three zones are present in both types of samples, and the coating-substrate interface is similarly coupled. The aspect of both, the metal deposit and the coating layer, is clearly different when the LAB process is carried out in air than when it takes place in vacuum. Additional surface roughness evaluation by confocal microscopy has been performed, nevertheless in order to better characterise these samples and their differences.

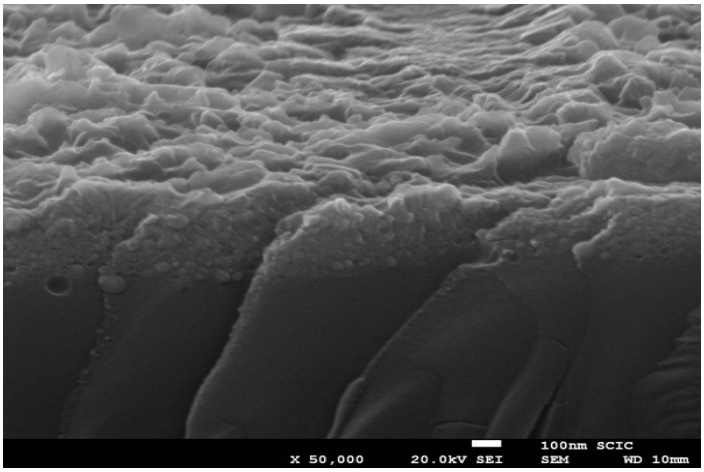

Figure 3.80: SEM micrograph of a sample obtained by LAB of 63Cu37Zn brass alloy target. A metal particle deposit can be distinguish on top of the substrate. The heavier atomic weight of Cu and Zn results in the lighter contrast that enables distinction of the coating and substrate.

Finally, the Ag target derived coatings obtained via LAB on glass substrates in air and under high vacuum conditions were also studied by SEM. Initial studies were centered in acid etched samples. Not all the Ag particles present at substrate's surface could be removed by acid etching as Figure 3.81 demonstrates. A wide size distribution of silver particles are easily observed on the surface of the substrate (white contrast).

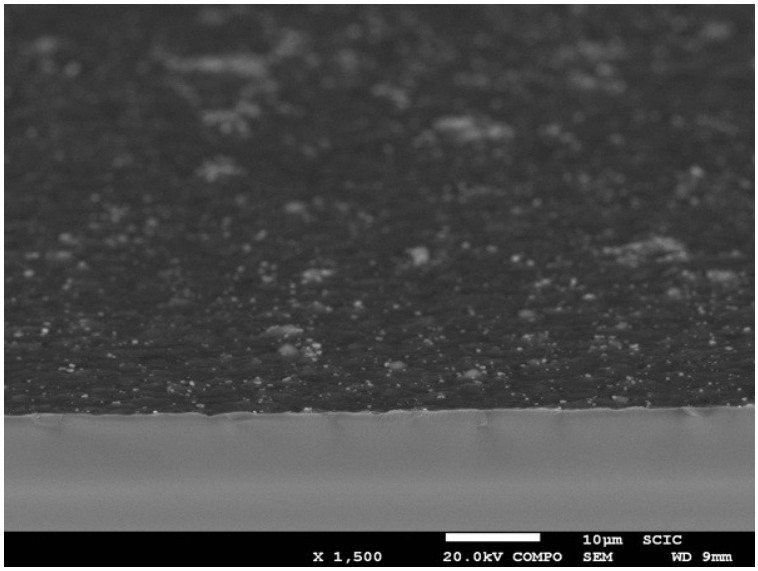

Figure 3.81: SEM micrograph of a Ag derived acid etched coating obtained by LAB in air. Ag particles (white contrast) are observed over the dark contrast surface of the substrate.

The fact that Ag is a good mirror for the nIR output wavelength of the Nd laser used, as is the case with Cu and Al, causes poor coupling of the laser radiation and lowers the ablation efficiency significantly. The result is the 1 µm thick LAB Ag coating observed in Fig. 3.82 as a lighter contrast. In addition, it appears as a different, smoother finish appearance than the equivalent Al and brass derived coatings.

Elemental analysis of these samples by EDX reveals the presence of a small amount of Cu, even within the spherical Ag particle shown in Fig. 3.83 and analysed in Figure 3.84. This is consistent with the fact that the original Ag target is not pure, but rather a commercial Ag-Cu alloy.

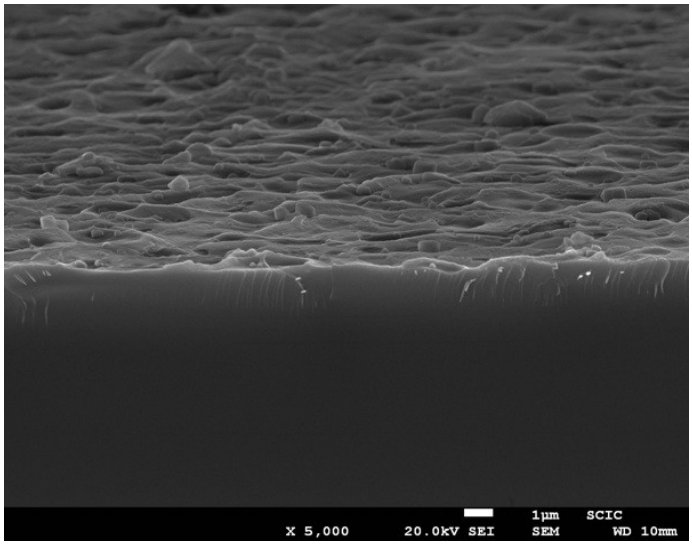

Fig. 3.82: SEM micrograph of a Ag waveguide on microscope slide obtained by LAB in air conditions. A bright zone around ca. 1 µm contens Ag. The surface of the sample is observed upper this zone.

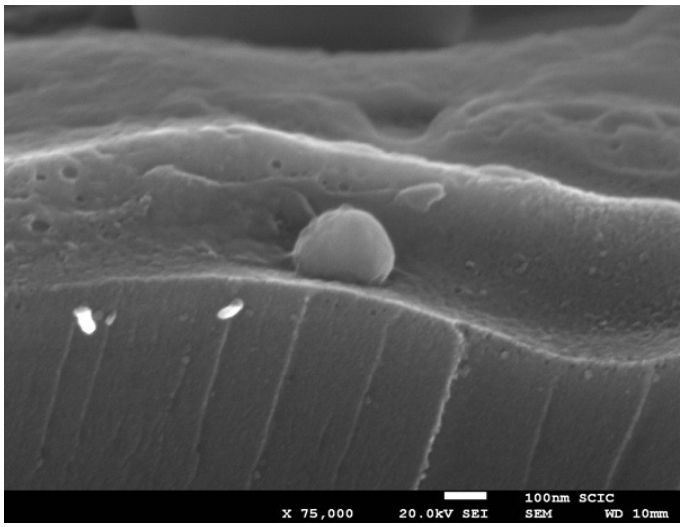

Figure 3.83: SEM micrograph of a spherical Ag particle found on the surface of an Ag derived LAB sample.

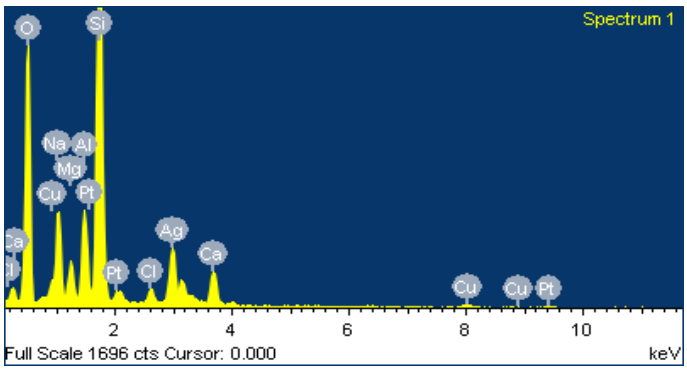

Figure 3.84: EDS spectrum obtained on the Ag particle shown in Fig. 3.83.

Ag samples without submitted to acid etching were finally observed by FE-SEM. A thick deposit of metal particles were again observed on the substrate's surface shown in Figure 3.85. These Ag particles appear more uniform when the ablation process is carried out under high vacuum atmosphere. The thickness of the granular coating obtained is ca. 1 μm, as observed on the middle part of the Figure, just below the dense glass substrate and above the granular substrate.

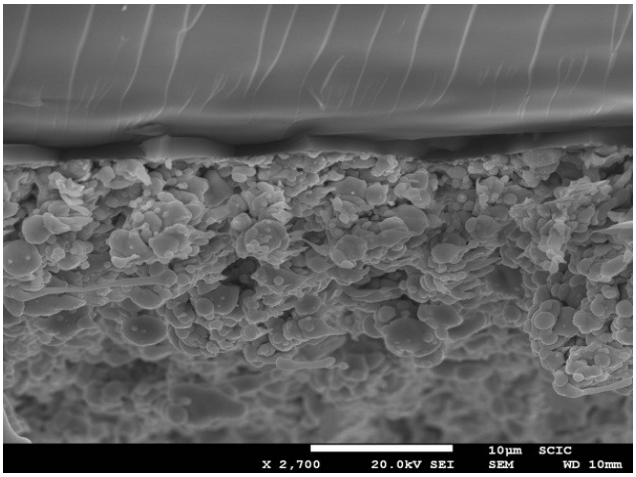

Figure 3.85: SEM micrograph of Ag derived coating obtained by LAB on a microscope slide substrate under high vacuum atmosphere. A dense coating obtained is ca. 1 μm, as observed on the middle part of the Figure, just below the dense glass substrate and above the granular deposit.

The study of the surface roughness of the LAB coatings and deposits described earlier was performed using confocal microscopy. A wide range of average surface roughness values were measured depending on the metal employed and the processing atmosphere. Lower surface roughness values are obtained for samples prepared under atmospheric conditions than those prepared in high vacuum. These values change considerably as a function of the metal target and laser power employed (Table XXXI).

Table XXXI: Average surface roughness values obtained on LAB coatings and deposits.

Sample (coating)	**Roughness (nm)**	**Sample (deposit)**	**Roughness (nm)**
Brass - air	74	***Brass - air***	323
Brass - vacuum	123	***Brass - vacuum***	659
Silver - air	47	***Silver - air***	539
Silver - vacuum	269	***Silver - vacuum***	1004

A comparison of the grating-like topographies obtained on a microscope slide substrate obtained by LAB of a brass target in air and in vacuum are shown, respectively, in Figures 3.86 and 3.87. We can relate this effect to the existence of a 'vacuum gap' between the metal target and the glass substrate in high vacuum conditions. In fact, the ablation plasma plume in vaccum is characterised by a much aspect ratio and becomes highly directional in the direction perpendicular to the target [177]. The ablated species find limited resistance to movement and can thus collide with the substrate more efficiently and with higher impact energy. Under normal atmosphere conditions, the presence of gases and particles impose significant constraints on the ablation plume, causing to be smaller in height and opposing large resistance to the free movement of excited species in the plasma.

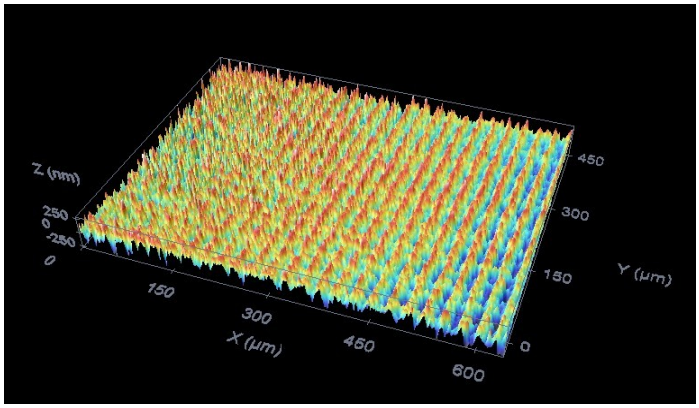

Figure 3.86: Topography obtained by Confocal Scanning Microscopy on a grating-like morphology prepared by LAB of a 63Cu37Zn alloy target in air.

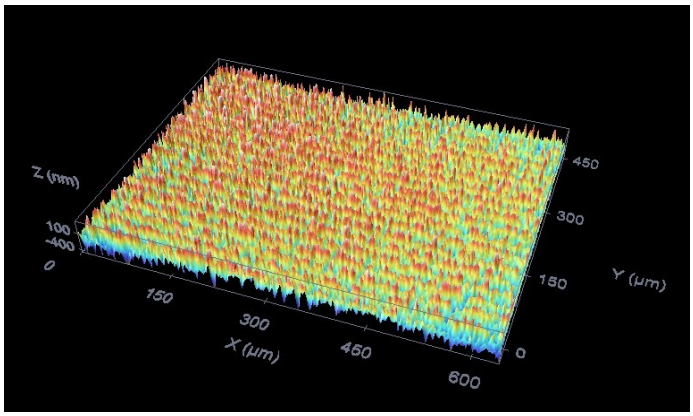

Figure: 3.87: Topography obtained by Confocal Scanning Microscopy on a grating-like morphology prepared by LAB of a 63Cu37Zn alloy target under high vacuum.

UV-Vis spectroscopy studies were carried out in order to study the environment of the spectroscopically active elements present within the coatings prepared. In addition, they were used to determine the optical transmission window characteristics within th UV-Vis-nIR range. Fig. 3.88 contains the spectra for LAB coatings derived from Al, Ag and 63Cu37Zn brass targets and prepared on microscope slide substrates.

The UV-Vis spectrum that corresponds to the Ag coating in Figure 3.88 is the black line. It exhibits the typical absorption peak identified for Ag around 430 nm. The minimum around 430 nm corresponds with the absorption peak associated to SPR (Surface Plasmon Resonance) of silver nanoparticles [125-128]. The peak appearing at ca. 500-600 nm corresponds to the SPR band of Cu (spectrum drawn in blue), consistent with the literature reporting the spectra observed for Cu nanoparticles suspended in SiO_2 glass and similar materials [128, 178]. In the case of Zn, displayed in the same blue line, a similar behavior to that reported in the literature is also found here [179-181], most likely buried within the hump near the UV region of the spectrum. Electron diffraction patterns, obtained on glass samples produced by laser backwriting brass alloy as target exhibit only the presence of Cu metal (see previous discussion, Fig. 3.66). Neither Zn, nor ZnO peaks appear on the diffraction patterns obtained, although it has been demonstrated that laser ablation of brass yields initially nanoparticles of the Cu/Zn alloy irradiated [179]. These alloy nanoparticles apparently decompose into their constituent metals, yielding separate Cu and Zn nanoparticles. Heating causes Zn to oxidise and migrate towards the surface of the glass substrate [180], consistently with the EDS measurements reported and discussed earlier in the text (Fig. 3.78 and Table XXX).

The materials subjected to study show high values of light transmission at the He-Ne wavelength (633nm). These measured values range from 78.1%T for Al derived coatings to 83.7%T for Ag derived coatings. Brass derived coatings (63Cu37Zn alloy), on the other hand, exhibit a transmission percentage of 79.2% at a wavelength of 633 nm.

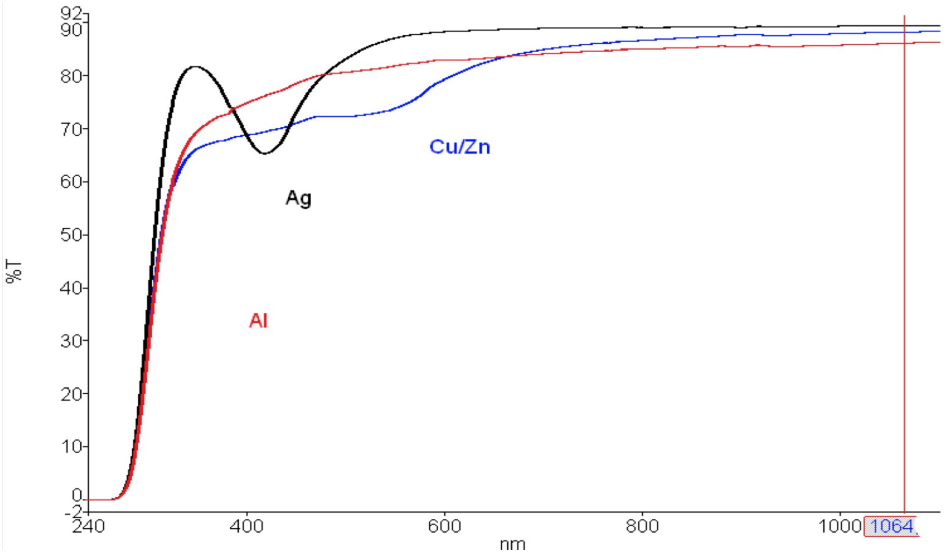

Figure 3.88: UV-Vis transmission spectra of the samples obtained by Laser Backwriting of metal targets. The black spectrum corresponds to the Ag sample, where its typical Surface plasmon Resonance band is clearly observed at around 430 nm. The red and blue spectra correspond to the Al and the brass derived bacwritten glass samples, respectively. The Cu SPR band is located between 500 and 600 nm, consistent with other published work [128, 178]. A vertical red line represents the 1064 nm output wavelenght of the laser used.

Electrical resistivity studies provide a convenient tool to complement the microstructural characterisation of the LAB coatings. A continuous metal coating without cracks, such as the one shown in Figure 3.89 should exhibit low electrical resistance values. In contrast, the presence of cracks within the coating, as in Figure 3.90, would disrupt such electrical continuity and cause high resistance values to appear. Multiple microscope observations under transmitted light indicate that each succesive laser written line provokes the formation of cracks on the previous one. As the LAB process requires a collection of parallel or succesive lines to fill any desired space or area, the formation of cracks is difficult to avoid, and clever scanning sequences must be found in order to achieve crack-free coatings by this method. According to Table XXXII, the Ag target derived coatings exhibited the lowest electrical resistance, in line with their smoother microstructure, discussed earlier.

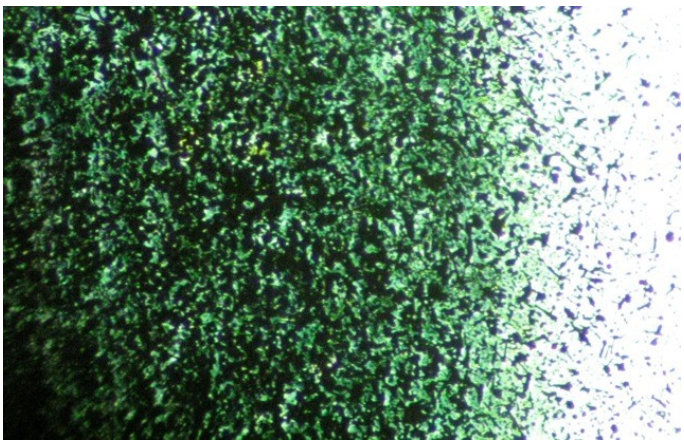

Figure 3.89: Image of a 63Cu37Zn coating deposited onto a microscope slide substrate by LAB. No-cracks are observed on the coating (darker area).

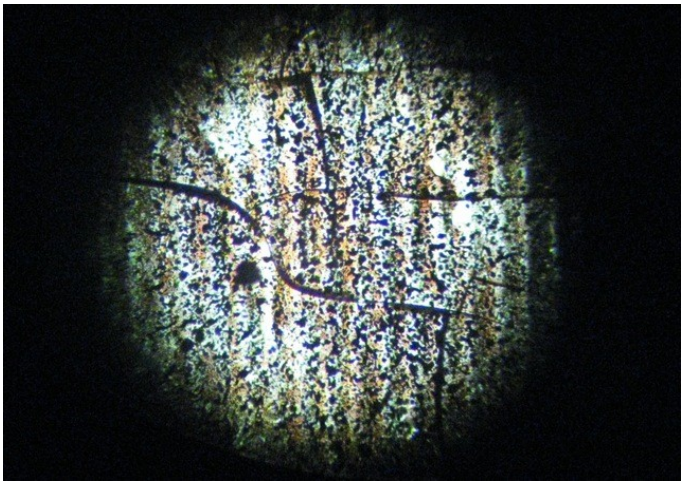

Figure 3.90: Image of a 63Cu37Zn coating deposited onto a microscope slide substrate by LAB. Several cracks are clearly observed perpendicular to the laser beam scanning direction.

Table XXXII: Laser parameters employed for Ag derived LAB samples under high vaccum conditions and their corresponding resistivity (*R*) values.

Condition	Power average (W)	Speed (mm/s)	Width line (µm)	Irradiance (W/cm2)	P_o (mbar)	$P_{máx}$ (mbar)	*R* (Ω/cm)
1	3.98	50	60	$5.03x10^{9}$	$8.4x10^{-7}$	$1.0x10^{-6}$	0.84
2	3.98	50	50	$5.03x10^{9}$	$8.4x10^{-7}$	$1.0x10^{-6}$	1.24
3	3.98	50	30	$5.03x10^{9}$	$8.4x10^{-7}$	$9.9x10^{-7}$	0.88
4	4.67	50	60	$6.88x10^{9}$	$8.4x10^{-7}$	$1.0x10^{-6}$	1.22
5	4.67	50	30	$6.88x10^{9}$	$8.4x10^{-7}$	$9.9x10^{-7}$	0.43
6	4.67	50	100	$6.88x10^{9}$	$8.4x10^{-7}$	$9.5x10^{-7}$	0.17
7	5.46	50	100	$8.78x10^{9}$	$8.4x10^{-7}$	$9.7x10^{-7}$	0.31
8	5.46	100	100	$8.78x10^{9}$	$8.5x10^{-7}$	$1.0x10^{-6}$	0.09
9	4.67	100	30	$6.88x10^{9}$	$8.5x10^{-7}$	$1.2x10^{-6}$	23000
10	3.98	100	30	$5.03x10^{9}$	$8.5x10^{-7}$	$1.4x10^{-6}$	5.20

Finally, the optical characterisation of coatings with dimensions 50x4 mm^2 were carried out at the USC and at the *Istituto di Fisica Applicata 'Nello Carrara'* (IFAC-CNR, Firenze, Italy) produced the following results. The direct butt-coupling method was applied to these kind of coatings. The metal-derived samples were previously polished to obtain the best optical quality for efficient coupling of light sources. Ag, brass and Al derived LAB samples were tested. By coupling the light into the substrate we could observe some modulation at the output (Fig. 3.91) which may be related to the structure of the coatings. Nevertheless, no efficient waveguiding effect similar to the preceeding waveguides described in this thesis was detected. Thus, observing the aspect of the waveguide when a laser beam is coupled. These coatings must be classified as diffusive guides (Fig. 3.92).

Figure 3.92 shows how light from a He-Ne laser (λ=632.8 nm, 1 mW) is guided through a layer made onto a commercial laboratory microscope glass slide by the Laser Ablation Backwritting (LAB) of a 63Cu37Zn target. The laser is directly coupled with a microscope objective (20x, NA 0.4) into the polished end of the modified glass substrate. Light from the He-Ne laser is observed to concentrate initially within the channel, although significant scattering is

observed after a certain point. Reflections appearing at the edges of the glass are due to transmission of light from the waveguide. Poor alignment/coupling of the red laser beam into the glass is evident, since no index adjustment media have been employed on this demonstrative experiment.

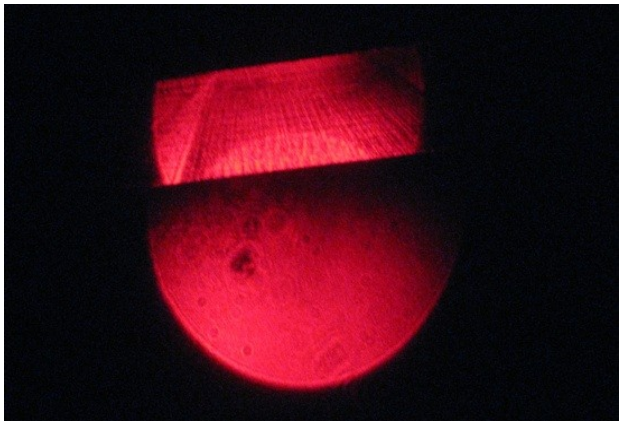

Figure 3.91: Projected image of a waveguide output showing some modulation of the light passing through a 63Cu37Zn brass derived LAB sample.

Figure 3.92: Demonstrative photograph showing how light from a He-Ne laser (λ=632.8 nm, 1 mW) is guided through a 63Cu37Zn brass derived LAB diffusive waveguide.

3.4 Comparative analysis for techniques

Planar waveguides with different characteristics have been fabricated by different methods in this thesis work. This chapter resumes these results to compare the techniques and samples obtained in each case.

Chemical processes exert a considerable influence over Sol-Gel and LZM preparative methods. In the Sol-Gel case, diffusion processes where alkaline and alkaline-earth ions migrate from the commercial glass substrate to the coating have been identified. This migration of ions induces a silicon-rich zone at the substrate region close to the interface with the coating. Considering LZM technique, chemical coupling is provided by an interdiffusion process in which ions coming from the coating (including Pb), difuse into the commercial glass substrate. At the same time, alkaline and alkaline-earth ions like Ca difuse in the opposite direction, from the glass to the coating. This different diffusion process are responsible for the different thicknesses observed for the interfaces areas. These are practically inexistent in the Sol-Gel coatings and are between 2-5 μm, for the waveguides obtained by LZM. For this reason, step-index waveguides are clearly obtained in the Sol-Gel method.

The study of the samples obtained by LAB reveals two different process which can be involved in the synthesis of planar waveguides. On the one hand, a physical process, where metal nanoparticles are ablated from the metal target and embeded into the glass substrate via acceleration through a plasma plume. On the other hand, a chemical process where highly reactive molten metal particles droplets are projected into the glass substrate, forming metal glass phases which integrate naturally into the glass matrix. The coatings obtained from brass and Ag targets fall under the first process described, while those obtained from Al fall under the second one.

The thickness of the coating obtained is an important factor to consider for waveguide fabrication, as explained in the Sol-Gel synthesis section, because of the minimum thickness needed for guiding light. This restriction depends of the wavelenght on the wavelength of the light employed. While the coatings obtained from Sol-Gel and LAB are in the same order of thickness, around 1

μm, the lowest thickness obtained by LZM was 10 μm. In the case of Sol-Gel samples, multilayer structures or hybrid sols must be employed to satisfy the thickness condition in order to achieve efficient waveguide coupling. Table XXXIII reports characteristic data of samples obtained by each of the methods employed in this work.

Table XXXIII: Comparision of thicknesses obtained for different samples through the corresponding fabrication method.

Method	Sample	Thickness (μm)
Sol-Gel	***SiTi (70:30)***	0.36
	SiTi-M (70:30)	1.05
	SiCe	2.33
	ZrCe (70:30)	0.20
	ZrCe-M (70:30)	0.50
Laser Zone Melting	***Lead borosilicate***	10.00
	Yb-doped lead borosilicate	10.00
Laser Ablation	***Al***	0.60
	63Cu37Zn	1.00
	Ag	1.00

The waveguides obtained by LZM are multimode. In contrast, the thickness obtained by Sol-Gel and LAB is typical of monomode waveguides [155]. Moreover, the LAB method enables the fabrication of 'burried' waveguides, while by the other two methods only facilitate the fabrication of waveguides on the surface of the substrate.

Another important factor for the guiding of the light studied is the surface roughness, which clearly differs depending on the metthod employed in the fabrication of planar waveguides. Table XXXIV summarizes the optimum results obtained for each method. The lowest surface roughness is provided by the Sol-Gel method.

Table XXXIV: Surface roughness for different samples prepared by the different methods used in this work.

Sample	Roughness average (nm)
SiO_2:TiO_2 (70:30) monolayer	< 20
ZrO_2:CeO_2 (70:30) monolayer	< 20
Lead borosilicate – CO_2 laser	230
63Cu37Zn (air)	74
Ag (air)	47

Important parameters that must be consider when talking about light guiding include the refractive index and the guiding efficiency. Following the preceeding studies, the results obtained vary depending on the compostion of the guiding layer. Table XXXV summarizes refractive indices and propagation coefficients of the most typical sample obtained by Sol-Gel and by LZM.

Table XXXV: Comparative of optical parameters of characteristical samples obtained by Sol-Gel and laser zone melting.

Method	Sample	Refractive index (n, λ=633nm)	Efficiency (dB/cm)
Sol-Gel	***SiTi-M (anneal)***	1.66	1.32
	ZrCe-M	2.07	0.86
	SiCe	1.47	1.50
Laser Zone Melting	***Lead borosilicate***	1.58	4.15

The samples obtained by laser ablation exhibit losses at least above 20 dB/cm. The change in the refractive index was measured by Rangel-Rojo et al. [29] and is in the range of $1{,}8x10^{-2}$ with respect to the refractive index of the substrate employed.

Finally, consideration should be given to the mechanism of light guiding. For the samples obtained by Sol-Gel and LZM, the mechanism is clear, a coating with a different refractive index has been incorporated onto the substrate. For this motive, the light is confined into the guiding layer. However, samples obtained by LAB exhibit modified zones within the substrates, away from their

outer surface. This buried doped area causes changes in the refractive index of the substrate within such zones. Furthermore, these are strongly directional because of the directionality intrinsic to laser beam scanning during LAB. Furthermore, the UV-Vis spectra change considerably with respect to the substrate and is affected by the presence of plasmons resonance bands associated to the metal nanoparticles (Cu, Ag) dispersed in the medium. Thus, in this kind of samples, the presence of plasmons promotes a change in the local electromagnetic field, and an increase in the refractive index value within the modified zone of the substrate.

CONCLUSIONS

This work reports the study of three different techniques to prepare planar coatings on inexpensive, commercial soda-lime glass substrates, which may be adapted for the fabrication of waveguides at and industrial scale. One of these, Laser Zone Melting, is a novel fabrication method that has never been explored before. The selection of each preparatory method is related with the type of waveguide structure desired, although the three methods converge on a most important common ground: the use of window glass substrates. This aspect is essential if the technical objectives of this work are fulfilled, since it would be enable the transition to viable industrial processes and products.

The conclusions, derived from the work presented in the previous chapters of this dissertation, are arranged by the type of preparatory method used and are summarised in the following paragraphs.

Sol-Gel method

Slab waveguides have been fabricated by the Sol-Gel method by applying the dip-coating technique over commercial soda lime glass substrates. In particular:

- Slab waveguides of different compositions, such as SiO_2:TiO_2, SiO_2:CeO_2, SiO_2:ZrO_2 and ZrO_2:CeO_2 have been obtained following Sol-Gel synthesis. Er has been succesfully incorporated as a dopant.

- The application of the Sol-Gel method for the fabrication of step-index waveguides allowed obtaining a wide range of coatings with a variety of refractive index values (between 1.47 and 2.07) and thicknesses (100 nm to tens of microns), by conveniently adjusting of the synthesis parameters (selecting the adequate precursors) to the final requirements of the desired coatings.

- The coatings thus obtained exhibit well-defined interfaces, are homogeneous and continuous throughout extension of the substrate's surface.

- Thick layers (up to 1.2 μm) were obtained by a subsequently stacking of several (up to 6) thin Sol-Gel layers. No cracks, nor macroscopic defects habe

been observed between successive layers in the multilayer Sol-Gel structures. This would enable further development of step-index waveguides for many foreseen applications.

- The combination of layers with different composition, and thus with a different refractive index was also demonstrated using SiTi and ZrCe sols.

- Coupling between commercial glass substrates and Sol-Gel coatings is dominated by a chemical diffusion processes. Alkali and alkaline-earth ions migrate from the substrate to the coating, while, at the same time, a Si rich zone is originated at the area of the substrate adjacent to the interface.

- Sol-Gel method provides samples with low surface roughness (< 20 nm), thereby enabling a potential decrease of propagation losses by reducing scattering at the coating surface.

- No crystalline phases were observed within the coatings obtained by this method. However, it allows the introducing nanoparticles that may induce multiple phenomena useful for the fabrication of waveguiding and sensoring elements.

- Waveguide losses evaluated using a method based on scattering light. In the cases of ZrO_2:CeO_2 (70:30) and multilayer SiO_2:TiO_2 (70:30), they were determined, respectively, as ca. 0.9 dB/cm (TE polarization) and ca. 1.3 dB/cm.

- The ZrO_2:CeO_2 coating was found to be birefringent, in consecuence with the fact that it contained tetragonal ZrO_2 crystals, as determined by X-ray diffraction.

Laser Zone Melting

Planar waveguides were obtained by laser zone melting (LZM) of commercial glass substrates deposited frits. Most relevant results obtained with this novel method include the following:

- Planar waveguides based on powder mixtures of SiO_2, B_2O_3 and PbO, have been obtained via melting onto commercial glass substrates.

- The differences in refractive index values found between the LZM coating (1.58) and commercial glass substrate (1.52) is sufficient to obtain the confinement of the light and the subsequent waveguiding effect through the coating.

- This technique allows obtaining coatings approaching 10 to 30 μm in thickness, which should be useful to prepare multimode waveguide. In contrast, the coating thickness obtained by conventional furnace processing of frits is well above 30 μm.

- LZM enables the achievement of less diffuse coating interfaces, as compared to conventional furnace melting methods.

- The coating-substrate coating is largely influenced by interdiffussion processes, where alkali and alkaline-earth ions migrate from the substrate to the coating. Simultaneously, Pb ions diffuse into the substrate. Chemical coupling between coating and substrate takes place at the atomic level, as deduced from TEM observations.

- LZM produces samples with considerable surface roughness, approaching 230 nm, which would hinder efficient waveguiding. Nevertheless, since the coatings obtained are thick, they may be polished to decrease surface roughness and, therefore, the associated losses.

- The losses determined for LZM samples are slightly higher than those obtained for Sol-Gel coatings. Losses of 4.15 dB/cm were measured for a Pb

borosilicate sample prepared by LZM. However, it was found that the use of dopants such as Yb and Bi could decrease waveguide losses to 3.04 dB/cm (Yb-doped waveguides).

- The use of the CO_2 laser allows fabricating waveguides in a one step process. A disadvantage, however, for several applications, is the presence of remaining translucent surfaces in the areas not scanned.

- Another possibility to obtain waveguides, making use of ceramic frits, is based on commercial glass substrate channel engraving. These have been obtained in this thesis by mechanical and laser ablation machining methods. The channels obtained by laser ablation exhibit improved surface finish and geometry definition.

Laser Ablation Backwriting of metal targets

Coatings have also been fabricated prepared on commercial glass substrates by the Laser Ablation Backwriting (LAB) process. Metal targets of Al, brass (63Cu37Zn) and Ag were employed. The study of this method was centered on identifying how the processing parameters influence the properties of the coatings obtained via ablation backwriting both, in air and in vacuum. The following conclusions have been reached:

- Coatings prepared with Al, brass (63Cu37Zn) and Ag were obtained on commercial glass substrates by the laser ablation backwriting of metal targets.

- LAB allows us to obtain coatings with variable thickness and geometry, accordingly with the laser and scanning parameters imposed with the available commercial software. In addition, this technique allows fabricating 'burried' waveguides directly, without further processing.

- The process of formation of coatings by LAB follows a different scheme, depending on the metal target used. For brass (63Cu37Zn) and Ag, ablated particles get projected and embede into the glass, where they remain in a

metallic or elemental state. When Al is used, however, the intense ablation of highly reactive Al species induces a chemical reaction to form aluminosilicates glass phases within the affected area of the glass substrate.

- The LAB process can be carried out in air or in other atmospheres. In the present study, two types of atmosphere conditions were applied. Higher directionality is observed in ablation plasma plume in vacuum with the consequent influence on the modified substrates.

- Surface roughness values vary considerabily as a function of the metal and processing environment. Lower surface roughness values, approaching 47 nm, were obtained for Ag derived coatings. Brass derived coatings exhibited surface roughness values of ca. 74 nm. In both of the above cases, LAB was carried out in air. Coatings obtained from the same metals under high vacuum conditions exhibited surface roughness values of 269 nm and 123 nm, respectively, for Ag and brass derived coatings. In the case of Al samples, the burried waveguides obtained allow surface polishing without affecting the doped zone, so that there was need to use surface roughness measurements to evaluate its degree of uniformity.

- When considering the deposits adhered to the surface of the coating, it is clear that vacuum conditions induce formation of higher amounts of debris. This contaminant layer is removed by acid etching before optical measurements are carried out.

- Plasmonic UV-Vis spectroscopy studies indicate that Ag and brass derived LAB coatings exhibit Surface Plasmon Resonance (SPR) bands, characteristic of the presence of Ag and Cu nanoparticles. These may be responsible for the increase observed in the refractive index of the substrate glass.

BIBLIOGRAPHY

[1] S.H. Song, E.H. Lee, C.D. Carey, D.R. Selviah & J.E. Midwinter, "Planar optical implementation of crossover interconnects", *Opt. Lett.* 17 (1992) 1253-1255.
[2] L.J. Camp, R. Sharma & M.R. Feldman, "Guide-wave and free-space optical interconnects for parallel-processing systems: a comparison", *Appl. Opt.* 33 (1993) 6168-6180.
[3] M. Testorf & J. Jahns, "Paraxial theory of planar integrated systems", *J. Opt. Soc. Am. A* 14 (1997) 1569-1575.
[4] M. Testorf & J. Jahns, "Image properties of planar integrated micro-optics", *J. Opt. Soc. Am. A* 16 (1999) 1175-1183.
[5] C. Gómez-Reino, M.V. Pérez & C. Bao, "Gradient-index Optics: Fundamentals and Applications", Edit. Springer-Verlag, Berlin (2002).
[6] C. Gómez-Reino, M.V. Pérez, C. Bao & M.T. Flores-Arias, "Design of GRIN optical components for coupling and interconnects", *Laser & Photonic Rev.* 2 (2008) 203-215.
[7] S.H. Song, S. Park, C.H. Oh & P.S. Kim, "Gradient-index planar optics for optical interconnections", *Opt. Lett.* 23 (1998) 1025-1027.
[8] E. Hecht, "Óptica"; Edit. Addisson Wesley, 3ª de. Madrid (2000).
[9] M.L. Calvo Padilla; "Óptica Avanzada", Edit. Ariel Ciencia, Barcelona (2002).
[10] R.G. Hunsperger, "Integrated optics: Theory and Technology", Edit. Springer, 5ª de. (2002).
[11] E. Josse, G. Fonteneu & J. Lucas, "Low-phonon waveguides made by F-/Cl-exchange ion fluoride glasses", *Mater. Res. Bull.* 32 (1999) 1139-1146.
[12] C.C. Huang, D.W. Hewak & J.V. Badding, "Deposition and characterization of germanium sulphide glass planar waveguides", *Opt. Express* 12 (2004) 2501-2506.
[13] J.W. Lee, S.S. Kim, B.T. Lee & J.H. Moon, "Ge-doped SiO_2 glass films prepared by plasma enhanced chemical vapour deposition for planar waveguides", *App. Surf. Sci.* 228 (2004) 271-276.
[14] Q.Y. Zhang, K. Pita, S.C. Tjin, C.H. Kam, L.P. Zuo & S. Takahashi, "Laser-induced ultraviolet absorption and refractive index changes in Ge-B-SiO_2 planar waveguides by inductively coupled plasma-enhanced chemical vapour deposition", *Chem. Phys. Lett.* 379 (2003) 534-538.
[15] P.J. Morais, M.C. Gonçalves & R.M. Almeida, "Physical vapour deposition of rare-earth doped ZrF_4-based glass planar waveguides", *J. Non-Cryst. Solids* 256-257 (1999) 194-199.
[16] E. Flores-Romero, G.C. Vázquez, H. Márquez, R. Rangel-Rojo, J. Rickards & R. Trejo-Luna, "Planar waveguide lasers by proton implantation in Nd:YAG crystals", *Opt. Express* 12 (2004) 2264-2269.
[17] N.Q. Khánh, S. Berneschi, I. Bányász, M. Brenci, M. Fried, G. Nunzi-Conti, F. Pászti, S. Pelli, G.C. Righini & A. Watterich, "Fabrication of channel waveguides in Er^{3+}-doped tellurite glass via N^+ ion implantation", *Nucl. Instr. And Meth. In Phys. Res. B.* 267 (2009) 2327-2330.

[18] H. Yamada, T. Sano, T. Nakayama & I. Miyamoto, "Optimization of laser-induced forward transfer process of metal thin films", *Appli. Surf. Sci.* 197-198 (2002) 411-415.

[19] A. Favre, E. Lee, V. Apostolopoulos, C.B.E. Gawith, C.Y. Tai, E. Taylor, Y. Kondo & F. Koizumi, "Fabrication and characterization of UV-written channel waveguides in Bi_2O_3-based glass", *Opt. Mater.* 27 (2004) 7-13.

[20] A.K. Mairaj, C. Riziotis, A.M. Chardon, P.G.R. Smith, D.P. Sheperd & D.W. Hewak, " Development of channel waveguide lasers in Nd^{3+} -doped chalcogenide (Ga:La:S) glass through photoinduced material modification" , *Appl. Phys. Lett.* 81 (2002) 3708-3710.

[21] K.K.B. Hon, L. Li & I.M. Hutchings, "Direct writing technology-Advances and developments", *CIRP Ann-Manuf. Technol.* 57 (2008) 601-620.

[22] J. Bohandy, B.F. Kim & F.J. Adrian, "Metal deposition from a supported metal film using an excimer laser", *J. Appl. Phys.* 60 (1986) 1538-1539.

[23] K. Kordás, K. Bali, S. Leppävuori, A. Uusimäki & L. Nánai, "Laser direct writing of copper on polyimide surfaces from solution", *Appl. Surf. Sci.* 154-155 (2000) 399-404.

[24] A.C. Tien, Z.S. Sacks & F.J. Mayer, "Precision laser metallization", *Microelectron. Eng.* 56 (2001) 273-279.

[25] H. Ebbendorf-Heidepriem, "Laser writing of waveguides ion photosensitive glasses", *Opt. Mater.* 25 (2004) 109-115.

[26] K.M. Davies, K. Miura, N. Sugimoto & K. Hirao, "Writing waveguides in glass with a femtosecond laser", *Opt. Lett.* 21 (1996) 1729-1231.

[27] S. Nolte, M. Will, J. Burghoff & A. Tuennermann, "Femtosecond waveguide writing: a new avenue to three-dimensional integrated optics", *Appl. Phys. A* 77 (2003) 108-111.

[28] C. Contardi, E.R. Taylor & A. Fu, "Study of UV-written channels in lead silicate glasses", *J. Non-Cryst. Solids* 291 (2001) 113-120.

[29] R. Rangel-Rojo, A. Castelo, M.T. Flores-Arias C. Gómez-Reino, C. López-Gascón & G.F. de la Fuente, "Refractive index modification in glass by laser backwriting ablation of metals", *Opt. Express* 14 (2006) 8765-8771.

[30] A. Castelo, D. Nieto, C.Bao, M.T. Flores-Arias, M.V. Pérez, C. Gómez-Reino, C. López-Gascón and G.F. De La Fuente, "Laser backwriting process in glass via ablation of metal targets", *Opt. Commun.* 273 (2006) 193-199.

[31] T. Yao & K. Takashima, "Amperometric biosensor with a composite membrane of sol-gel derived enzyme film and electrochemically generated poly(1,2-diaminobenzene) film", *Biosens. Bioelectron.* 13 (1998) 67-73.

[32] H. Li, D. Jin, Q. Yu & H. Tu, "Optical humidity sensing, proton-conducting sol-gel glass monolith", *J. Power Sources* 196 (2011) 3836-3840.

[33] A. Zalga, J. Reklaitis, E. Norkus, A. Beganskiene & A. Kareiva, "A comparative study of $YBa_2Cu_4O_8$(Y-124) superconductors prepared by a sol-gel method", *Chem. Phys.* 327 (2006) 220-228.

[34] S. Tao, Q. Wu, Z. Zhan & G. Meng, "Preparation of $LiMO_2$ (M=Co, Ni) cathode materials for intermediate tamperature fuel cells by sol-gel processes", *Solid State Ionics* 124 (1999) 53-59.

[35] T. Olding, M. Sayer & D. Barrow, "Ceramic sol-gel composite coatings for electrical insulation", *Thin Solid Films* 398-399 (2001) 581-586.

[36] L. Yang, S.S. Saavedra, N.R. Armstrong & J. Hayes, "Fabrication and characterization of low-loss sol-gel planar waveguides", *Ann. Chem.* 66 (1994) 1254-1263.

[37] L. Weisenbach & B.J.J. Zelinski, "The attenuation of sol-gel waveguides measured as a function of wavelenght and sample age", *Sol-Gel Optics III, Proc. SPIE* 2288 (1994) 630-639.

[38] G. Brusatin, M. Guglielmi, P. Innocenzi, A. Martucci, G. Battaglin, S. Pelli & G. Righini, "Microstructural and optical properties of sol-gel silica-titania waveguides", *J. Non-Cryst. Solids* 220 (1997) 202-209.

[39] M. Yoshida & P.N. Prassad, "Sol-gel processed SiO_2/TiO_2/Poly(vinylpyrrolidone) composite materials for optical waveguides", *Chem. Mater.* 8 (1996) 235-241.

[40] Y. Sorek, R. Reisfeld & R. Tenne, "The microstructure of titanium modified silica glass waveguides prepared by the sol-gel method", *Chem. Phys. Lett.* 227 (1994) 235-242.

[41] L.J.Q. Maia, V.R. Mastelaro, A.C. Hernandes, J.Fick & A. Ibanez, "Er:$YAl_3(BO_3)_4$ glassy thin films from polymeric precursor and sol-gel methods: Waveguides for integrated optics", *Thin Solid Films* 517 (2009) 6584.

[42] C. Le Luyer, L. Lou, C. Bovier, J.C. Plenet, J.G. Dumas & J. Mugnier, "A thick sol-gel layer for optical planar waveguide applications", *Opt. Mater.* 18 (2001) 211-217.

[43] S. Berneschi, S. Soria, G.C. Righini, G. Alombert-Goget, A. Chiappini, A. Chiasera, Y. Jestin, M. Ferrari, S. Guddala, E. Moser, S.N.B. Bhktha, B. Boulard, C. Duverger Arfuso & S. Turrell, "Rare-earth-activated glass-ceramics waveguides" *Opt. Mater.* 32 (2010) 1644-1647.

[44] J.L. Ferrari, K.O. Lima, L.J.Q. Maia & R.R. Gonçalves, "Sol-gel preparation of near-infrared broadband emitting Er^{3+}-doped SiO_2-Ta_2O_5 nanocomposite films", *Thin Solid Films* 519 (2010) 1319-1324.

[45] L. Levene & I.M. Thomas, "Process of converting metalorganic compounds and high purity products obtained therefrom", *US Patent No 3640093* (February 1972).

[46] J.C. Brinker & S.T. Reed, "Low temperature process for obtainning thin glass films", *US Patent No 4476156* (October 1984).

[47] L.L. Hench & J.K. West, "The Sol-Gel process", *Chem. Rev.* 90 (1990) 33-72.

[48] A.M. Buckley and M. Greenblatt, "The sol-gel preparation of silica gels", *J. Chem Educ.* 71 (1994) 599-602.

[49] J. Livage & C. Sanchez, "Sol-gel chemistry", *J. Non-Cryst. Solids* 145 (1992) 11-19.

[50] A.B. Atkarskaya, "Sol-gel coatings on float glass", *Steklo Keram.* 4 (2006) 5-6.

[51] P.C.A. Jerónimo, A.N. Araújo, M. Conceiçao & B.S.M. Montenegro, "Optical sensors and biosensors based on sol-gel films", *Talanta* 72 (2007) 13.

[52] C. Sanchez & F. Ribot, "Design of hybrid organic-inorganic material synthesized via sol-gel chemistry", *New J. Chem.* 18 (1994) 1007-1047.

[53] R.R. Gonçalves, J.J. Guimaraes, J.L. Ferrari, L.J.Q. Maia & S.J.L. Ribeiro, "Active planar waveguides based on sol-gel Er^{3+}-doped SiO_2-ZrO_2 for photonic applications: Morphological, structural and optical properties", *J. Non-Cryst. Solids* 354 (2008) 4846-4851.

[54] M. Guglielmi, P. Colombo, L. Mancinelli Degli Espositi, G.C. Righini & S. Pelli, "Planar and strip optical waveguides by sol-gel method and laser densification", *Glasses for Optoelectronics II, Proc. SPIE* 1513 (1991) 44-49.

[55] M. Guglielmi, P. Colombo, L. Mancinelli Degli Espositi, G.C. Righini, S. Pelli & V. Rigato, "Characterization of laser-densified sol-gel films for the fabrication of planar and strip optical waveguides", *J. Non-Cryst. Solids* 147-148 (1992) 641-645.

[56] P. Innocenzi, A. Martucci, M. Guglielmi, L. Armelao, S. Pelli, G.C. Righini & G.C. Battaglin, "Optical and surface properties of inorganic and hybrid organic-inorganic silica-titania sol-gel planar waveguides", *J. Non-Cryst. Solids* 259 (1999) 182-190.

[57] S.A. Pellice, R.J.J. Williams, I. Sobrados, J. Sanz, Y. Castro, M. Aparicio & A. Durán, "Solutions of hybrid silica-microgels as precursors of sol-gel coatings", *J. Mater. Chem.* 16 (2006) 3318-3325.

[58] W.F. Smith & J. Hashemi, "Fundamentos de la ciencia e ingeniería de materiales", Edit. McGraw-Hill, 4ª ed. 2006.

[59] D. Segal; "Chemical synthesis of avanced ceramic materials", Edit. Cambridge University Press, 1989.

[60] P. Escribano López, J.B. Carda Castelló & E. Cordoncillo Cordoncillo, "Esmaltes y pigmentos cerámicos", Faenza Editrice Ibérica, S.L. 2001.

[61] M. Rodríguez, H. Bentos Pereira & L. Fornaro, "Diseño de vidrios bóricos de aplicación en fibras ópticas" Ciencia e Ingeniería de los materiales, Universidade de la República, Campinas (Brasil) 2006.

[62] H.Y. Koo, S.K. Hong, S.H, Ju, I.S. Seo, Y.C. Kang, "PbO-B2O3-SiO2 glass powders with spherical shape prepared by spray pyrolysis", *J. of Non-Cryst. Solids* 352 (2006) 3270-3274.

[63] F. Detraux, F. Finocchi & X. Gonze, "First-principles study of $PbSiO_3$ alamosite", *Phys. Rev. B* 73 (2006) 165208.

[64] I. Avramov, T. Vassilev & I. Penkov, "The glass transition temperature of silicate and borate glasses", *J. Non-Cryst. Solids* 351 (2005) 472-476.

[65] M. Prudenziati, B. Morten, B. Forti, A.F. Gualtieri & G. Mihai Dilliway, "Devitrification kinetics of high lead glass for hybrid microelectronics", *Inter. J. Inorg. Mater.* 3 (2001) 667-674.

[66] F. Fayon, I. Farnan, C. Bessada, J. Coutures, D. Massiot & J.P. Coutures, "Empirical correlations between ^{207}Pb-NMR chemical sifts and structures in solids", *J. Am. Chem. Soc.* 119 (1997) 6837.

[67] Y. Cheng, H. Xiao, W. Guo & W. Guo, "Structure and crystallization kinetics of $PbO\text{-}B_2O_3$ glasses", *Ceram. Int.* 33 (2007) 1341-1347.

[68] X.C. Long & S.R.J. Brueck, "Composition dependence of the photoinduced refractive-index change in lead silicate glasses" *Opt. Lett.* 24 (1999) 16, 1136-1138.

[69] J. Bakali, E. Fortanet, G.F. De la Fuente, R. Lahoz, L.C. Estepa, G. Peris, I. Marinova, R. Pavlov, J.M. Pedra & J. Carda, "Structural and microstructural characterisation of refractory oxides synthesised by laser", *Key Eng. Mater.* 264-268 (2004) 317-321.

[70] A. Larrea, G.F. De la Fuente, R.I. Merino & V. Orera, "$ZrO_2\text{-}Al_2O_3$ eutectic plates produced by laser zone melting", *J. Eur. Ceram. Soc.* 22 (2002) 191-198.

[71] M. Mora, F. Gimeno, L.A. Angurel & G.F. De la Fuente, "Laser zone melted $Bi_2Sr_2CaCu_2O_{8+\delta}$ thick films on (100) MgO substrate", *Supercond. Sci. Technol.* 17 (2004) 1133-1138.

[72] M. Mora, J.C. Diez, C.I. López-Gascón, E. Martínez & G.F. de la Fuente, "Laser textured Bi-2212 in planar geometries", *IEEE Trans. Appl. Supercon.* 13 (2003) 3188-3191.

[73] M. Mora, C. López-Gascón, L.A. Angurel & G.F. de la Fuente, "The influence of support temperature on Bi-2212 monoliths textured by diode laser zone melting", *Supercond. Sci. Technol.* 17 (2004) 1329-1334.

[74] M. Mora, V. Lennikov, H. Amaveda, L.A. Angurel, G.F. de la Fuente, M. T. Bona, C. Mayoral, J. M. Andrés & J. Sánchez-Herencia, "Fabrication of Superconducting Coatings on Structural Ceramic Tiles", *IEEE Trans. Appl. Supercond.* 19 (2009) 3041-3044.

[75] V.V. Lennikov, J.M. Pedra, J.J. Gómez, G.F. De la Fuente & J.B. Carda, "In-situ synthesis of MTiO3-Al2O3 composite coatings via Laser Zone Melting", *Solid State Sci.* 9 (2007) 404-409.

[76] V.V. Lennikov, P.E. Kazin, Yu.D. Tretyakov & G.F. de la Fuente, "Laser zone melting and Texture Formation in MgO-doped BSCCO 2212", *Z. Anorg. Allg. Chem.* 630 (2004) 2337-2342.

[77] I. de Francisco, V.V. Lennikov, J.A. Bea, A. Vegas, J.B. Carda & G.F. de la Fuente, "In-situ laser synthesis of rare earth aluminate coatings in the system Ln-Al-O (Ln=Y,Gd)", *Solid State Sci.* 13 (2011**)** 1813-1819**.**

[78] J. Gurauskis, V. Lennikov, G.F. de la Fuente & R.I. Merino, "Laser-assisted, crack-free surface melting of large eutectic ceramic bodies", *J. Eur. Ceram. Soc.* 31 (2011) 1251-1256.

[79] F. Gutiérrez-Mora, A. Domínguez-Rodríguez, V.V. Lennikov & G.F. de la Fuente, "Influence of thermal effects produced by laser treatment on the tribological behavior of porcelain ceramic tiles", *Key Eng. Mater.* 423 (2010) 41-46.

[80] L.C. Estepa & G.F. De la Fuente, "Horno contínuo láser acoplado para el tratamiento superficial de materiales", Patente No. 200600560 (Marzo 2006).

[81] L.C. Estepa & G.F. De la Fuente, "Continuous furnace with coupled laser for the surface treatment of materials", Patent number EP2007-0730487 (19/11(2008).

[82] www.laserfiring.eu

[83] E. Tejada-Rosales, S. Ondoño-Castillo, C. Diez, G.F. de la Fuente & N. Casañ-Pastor, "Annealing of electrophoretic $YBa_2Cu_3O_7$ coatings on polycristaline substrates by zonal laser fusion", *Bol. Soc. Esp. Cerám. V*. 41 (2002) 185-189.

[84] A. Pascual, E. Fortanet, J.B. Carda, J.M. Pedra, R. Lahoz & G.F. de la Fuente, "Ceramic tile decoration by laser technology", *CFI-Ceramic Forum International* 82, E37-E42 (2005).

[85] R. Lahoz, J.P. Espinós, G.F. de la Fuente & A.R. González-Elipe, "In-situ XPS studies of laser induced surface cleaning and nitridation of Ti", *Surf. Coat. Technol.* 202 (2008) 1486-1492.

[86] L.A. Angurel, J.C. Diez, G.F. de la Fuente, "Laser Induced Cylindrical Zone Melting of $Bi_2Sr_2CaCu_2O_{8+\delta}$ Superconductors", *Z. Anorg. Allg. Chem.* 635 (2009) 1767-1772.

[87] J.R. Sánchez-Valencia, J. Toudert, A. Borrás, A. Barranco, R. Lahoz, G.F. de la Fuente, F. Frutos & A.R. González-Elipe, "Selective Dichroic Patterning by Nanosecond Laser Treatment of Ag Nanostripes", *Adv. Mater.* 23 (2011) 848-853.
[88] H.G. Rubahn, "Laser applications in surface science and technology", Edit. John Wiley, New York 1999.
[89] R. Lahoz Espinosa, Thesis: "Ablación láser de materiales inorgánicos y metálicos"; Insituto de Ciencia de Materiales de Aragón (CSIC-Universidad de Zaragoza) 2006.
[90] A. Castelo Porta, Thesis: "Diseño y fabricación de dispositivos híbridos planares para microóptica mediante irradiación y ablación láser de substratos de vidrio"; Universidade de Santiago de Compostela, 2008.
[91] M.T. Flores-Arias, A. Castelo, C. Gómez-Reino and G.F. De La Fuente, "Phase diffractive optical grating on glass substrates by laser ablation", *Opt. Commun.* 282 (2009) 1175-1178.
[92] E. Cattaruzza, M. Mardegan, E. Trave, G. Battaglin, P. Calvelli, F. Enrichi and F. Gonella, "Modifications in silver-doped silicate glasses induced by ns laser beams", *Appl. Surf. Sci.* 257 (2011) 5434.5438.
[93] D. Bäuerle, "Laser Processing and Chemistry", Edit. Springer-Verlag, Berlin (2000) 3rd Edition. ISBN 3-540-66891-8.
[94] B. Jaeggi, B. Neuenschwander, M. Schmid, M. Muralt, J. Zuercher, U. Hunziker, "Influence of the Pulse Duration in the ps-Regime on the Ablation Efficiency of Metals", *Physics Procedia* 12 (2011) 164-171.
[95] U. Chakravarty, P. A. Naik, C. Mukherjee, S. R. Kumbhare, P. D. Gupta, "Formation of metal nanoparticles of various sizes in plasma plumes produced by Ti:sapphire laser pulses", *J. Appl. Phys.* 108 (2010) 053107 pp 1-5.
[96] J. Qiu, "Femtosecond Laser-induced Microstructures in Glasses and Applications in Micro-optics", *The Chemical Record* 4 (2004) 50-58.
[97] J. Qiu, K. Miura, K. Hirao, "Femtosecond laser-induced microfeatures in glasses and their applications", *J. Non-Cryst. Solids* 354 (2008) 1100-1111.
[98] H.K. Pulker, "Coatings on glass", Edit. Elsevier, 1996.
[99] D.P. Norton, "Synthesis and properties of epitexial electronic oxide thin-film materials", *Mater. Sci. Eng. R* 43 (2004) 139-247.
[100] M. Poulain, "Advanced glasses", *Ann. Chim. Sci. Mater.* 28 (2003) 87-94.
[101] R. Stepien, R. Buczynski, D. Pysz, I. Kujawa, A. Filipowski, M. Mirkowski & R. Diduszko, "Development of thermally stable tellurite glasses designed for fabrication of microstructured optical fibers", *J. Non-Cryst. Solids* 357 (2011) 873-883.
[102] G. Monteiro, L.F. Santos, J.C.G. Pereira & R.M. Almeida, "Optical and spectroscopic properties of germanotellurite glasses", *J. Non-Cryst. Solids* 357 (2011) 2695-2701.
[103] B.I. Lee, Z. Chao, W.N. Sisk, J. Hudak, W.D. Samuels & G.J. Exarhos, "Photoresponse of Tb^{3+} doped phosposilicate thin films", *Mat. Res. Bui.* 32 (1997) 1285-1292.
[104] C. Urlacher, O. Marty, J.C. Plenet, J. Serughetti & J. Mugnier, "Structural and microstructural analysis of sol-gel lead titanate optical planar waveguides" *Thin Solid Films* 349 (1999) 61-66.

[105] D. Sparks, S. Mansoud-Ansari & N. Najafi, "Long-term evaluation of hermetically glass frit sealed silicon to Pyrex wafers with feedthroughs", *J. Micromech. Microeng.* 15 (2005) 1560-1564.
[106] J.M. Navarro, "El vidrio"; Edit. Consejo Superior de Investigaciones Científicas, 1ª ed., 2003.
[107] R.H. Doremus, "Glass science", Edit. Wiley Interscience Publication, 1973.
[108] J.E. Shelby, "Introduction to glass science and technology", Edit. Cambridge: The Royal Society of Chemistry, 2005.
[109] Y. Castro, B. Ferrari, R. Moreno & A. Durán, "Silica-Zirconia coatings produced by dipping and EPD from colloidal sol-gel suspensions", *J. Sol-Gel Sci. Technol.* 35, 1 (2005) 41.
[110] N.C. Rosero-Navarro, S.A. Pellice, A. Durán & M. Aparicio, "Effects of Ce-containning sol-gel coatings reinforced with SiO_2 nanoparticles on the protection of AA2024" *Corrosion Sci.* 50 (2008) 1283.
[111] R.R. Gonçalves, Y. Messaddeq, A. Chiasera, Y. Jestin, M. Ferrari & S.J.L. Ribeiro, "Erbium-activated silica-zirconia planar waveguides prepared by sol-gel route", *Thin Solid Films* 516 (2008) 3094-3097.
[112] R.M. Almeida & A.C. Marques, "Rare-earth photoluminiscence in sol-gel derived confined glass structures", *J. Non-Cryst. Solids* 352 (2006) 475-482.
[113] R. Sáez Puche, C. Cascales, P. Procher & P. Maestro, "Tierras raras: materiales avanzados", in *Anales de la Real Sociedad Española de Química* 2ª época (2000) 11-26.
[114] A. Orera Utrilla, "Metalizado de vidrio mediante técnicas de ablación láser", Proyecto Fin de Carrera de Ingeniería Industrial, Universidad de Zaragoza (Octubre 2002).
[115] A.J. Barbosa, L.J.Q. Maia, A.M. Nascimiento, R.R. Gonçalves, G. Poirier, Y. Messadeq & S.J.L. Ribeiro, "Er^{3+}-doped gremanate glasses for active waveguides prepared by $Ag^+/Na^+ \leftrightarrow Na^+$ ion-exchange", *J. Non-Cryst. Solids* 354 (2008) 4743-4748.
[116] F. Chen, X.L. Wang & K.M. Wang, "Development of ion-implanted optical waveguides in optical materials: A review", *Opt. Mat.* 29 (2007) 1523-1542.
[117] C.C. Lee & R.W. Chuang, "A dry electromigration process for fabricating deep optical channel waveguides on glass and their characterization", *Mat. Sci. Eng. B* 111 (2004) 40-48.
[118] C.C. Huang & D.W. Hewak, "Silver-doped germanium sulphide glass channel waveguides fabricated by chemical vapour deposition and photo-disoluton process", *Thin Solid Films* 500 (2006) 247-251.
[119] www.usc.es/gl/investigacion/riaidt/ir-raman/investigacion.html
[120] www.usc.es/gl/investigacion/riaidt/raiosx/fluorescencia/descrip_fluo.html
[121] www.uned.es/cristamine/mineral/metodos/xrfs.htm
[122] www.espectrometría.com/espectrometria_ultravioleta-visible
[123] J.N. Solanki, R. Sengupta and Z.V.P. Murthy; "Synthesis of coppersulphide and copper nanoparticles with microemulsion method", *Solid State Sci.* 12 (2010) 1560-1566.
[124] G. Suyal, "Bimetallic colloids of silver and copper in thin films: sol-gel synthesis and characterization"; *Thin Solid Films* 426 (2003) 53-61.

[125] L. Baia, M. Baia, W. Kiefer, J. Popp and S. Simon, “Structural and morphological properties of silver nanoparticles-phosphate glass composite”, *Chem. Phys.* 327 (2006) 63-69.
[126] M. Darroudi, M.B. Ahmad, R. Zamiri, A.M. Abdullah, N.A. Ibrahim, K. Shameli and M.S. Husin, “Preparation and characterization of gelatin mediated silver nanoparticles by laser ablation”, *J. Alloys Compd.* 509 (2011) 1301-1304.
[127] T. Xu, F. Chen, X. Shen, S. Dai, Q. Nie, X. Wang, "Observation of surface plasmon resonance of silver particles and enhanced third-order optical nonlinearities in AgCl doped Bi_2O_3–B_2O_3–SiO_2 ternary glasses", *Materials Research Bulletin* 45 (2010) 1501–1505.
[128] C.H. Zhao, B. P. Zhang, S. J. Wang, P. P. Shang, S. Li, L. P. Yan, "Microstructure and optical absorption property of the Cu/SiO_2 nano-films", *Materials and Design* 32 (2011) 947-950.
[129] S.A. Kalele, N.R. Tiwari, S.W. Gosavi and S.K. Kulkarni, “Plasmon-assisted photonics at the nanoscale”, *J. Nanophotonics* 1 (2007) 012501.
[130] S. Linden, J. Kuhl and H. Giessen, “Controlling the interaction between light and gold nanoparticles: Selective suppression of extinction”, *Phys. Rev. Lett.* 86 (2001) 4688-4691.
[131] J.B. Pawley (editor), “Handbook of Biological Confocal Microscopy”, Edit. Springer, Berlin, 2006.
[132] web.media.mit.edu/~minsky
[133] www.binderlab.northwestern.edu/confocal-web-site.html
[134] H. Li, Y. Su, L. Li & D.M. Strachan, “Raman spectroscopic study of gadolinium (III) in sodium-aluminoborosilicate glasses”, *J. Non-Cryst. Solids* 292 (2001) 167-176.
[135] S. Amelinckx, D. Van Dyck, J. Van Landuyt & G. Van Tendeloo, “Electron Microscopy: Principles and Fundamentals”, Edit. Willey, Weinheim (1997).
[136] D.B. Williams & C.B. Cartier, “Tarnsmission electron microscopy: A textbook for Materials Science”, Edit. Plenum Press, New York & London (1996).
[137] www.hei.org/research/aemi/emt.htm
[138] A. Strecker, U. Salzberger and J. Mayer, “Probenpräparation für die Transmissionelektronenmikroskopie”, *Prakt. Metallogr.* 30 (1993) 481-487.
[139] B. Wiedenhorst, C. Höfener, Yafeng Lu, J. Klein, M.S.R. Rao, B.H. Freitag, W. Mader, L. Alff and R. Gross, “High resolution transmission electron microscopy study on strained epitaxial manganite thin films and heterostructures”, *J. Magn. Magn. Mat.* 211 (2000) 16-21.
[140] J. Shi, W. Yu, I. Bergmann, H. Bremers, V. Šepelák, W. Mader & K.D. Becker, “Synthesis and characterization of nonstoichiometric $NiGa_2O_4$ transparent thin films”, *J. Alloys Compd.* 504 (2010) S432.
[141] C. Chanmuang, M. Naksata, T. Chairmaugsri, H. Jain & C.E. Lyman, “Microscopy and strength of borosilicate glass-to-Kovar alloy joints”, *Mat. Sci. Eng B* 474 (2008) 218-224.
[142] T. Okhubo, S. Shoji, Y. Kawamura & K. Hono, “Nanostructure analysis of friction welded Pd-Ni-P/Pd-Cu-Ni-P metallic glass interface”, *Scripta Mater.* 53 (2005) 493-497.

[143] K.K. Hong, S.B. Cho, J.S. Yan, J.W. Jeong, S.M. Bea & J.Y. Huh, "Mechanism for the formation of Ag crystallites in the Ag thick-film contacts of crystalline Si solar cells", *Sol. Energy Mater. Sol. Cells* 93 (2009) 898-904.
[144] C. Armellini, A. Chiappini, A. Chiasera, M. Ferrari, Y. Jestin, E. Moser, G. Nunzi Conti, S. Pelli, A. Quandt, G.C. Righini & C. Tosello, "Er^{3+}-activated nanocomposite photonic glasses and confined structures", *Opt. Mat.* 31 (2009) 1071-1074.
[145] L. Armelao, M. Fabrizio, S. Gialanella & F. Zordan, "Sol-Gel synthesis and characterisation of ZnO-based nanosystems", *Thin Solid Films* 394 (2001) 89-95.
[146] M. Zaharescu, V.S. Teodorescu, M. Gartner, M.G. Blanchin, A. Barau & M. Anastasescu, "Correlation between the method of preparation and the properties of the sol-gel HfO2 thin films", *J. Non-Cryst. Solids* 354 (2008) 409-415.
[147] F.A. Sigoli, R.R. Gonçalves, A.S. Camargo, L.A. Nunes, Y. Messadeq & S.J.L. Ribeiro, "Preparation and characterization of erbium and ytterbium co-doped sol-gel SiO_2:HfO_2 films for planar waveguides", *Opt. Mat.* 30 (2007) 600-607.
[148] www.ndt-ed.org/EducationResources/CommunityCollege/Materials.htm
[149] books.mcgraw-hill.com/EST10/site/articles/ElectricalConductivityOfMetals.pdf
[150] R. Göring & M. Rothhardt, "Application of the refractive near field technique to multimode planar and channel waveguides in glass", *J. Opt. Commun.* 7 (1986) 82-85.
[151] H. Fujiwara, "Spectroscopy ellipsometry: Principles and applications", Wiley & Sons, Tokyo (2007).
[152] J.A. Woollam, P.G. Snyder & M.C. Rost, "Variable angle spectroscopic ellipsometry: A non-destructive characterization technique for ultrathin and multilayer materials", *Thin Solid Films* 166 (1988) 317-323.
[153] J.A. Woollam, J.N. Hilfiker, T.E. Tiwald, C.L. Bungary, R.A. Synowicki, D.E. Meyer, C.M. Herzinger, G.L. Pfeiffer, G.T. Cooney & S.E. Green, "Varieble angle spectroscopic ellipsometry in the vacuum ultraviolet", *Proc. SPIE* 4099 (2000) 197-205.
[154] www.uta.edu/optics/research/ellipsometry/ellipsometry.htm
[155] K. Okamoto, "Fundamentals of Optical waveguides", Edit. Academic Press, New York (2000).
[156] P.K. Tien, "Light waves in thin films and integrated optics", *App. Opt.* 10 (1971) 2395-2413.
[157] R. Chassagnon, O. Marty, P. Moretti, C. Urlacher & J. Mugnier, "Modification of sol-gel TiO_2 planar waveguides by Xe^+ irradiation", *Nucl. Instr. And Meth. In Phys. Res. B.* 122 (1997) 550-552.
[158] G. Della Giustina, G. Brusatin, M. Guglielmi, M. Dispenza, A.M. Fiorello, M. Varasi, M. Casalboni, [a] Quatela, F. De Matteis, E. Giorgetti, G. Margheri, P. Innocenzi, [a] Abotto, L. Beverina and G.A. Pagani, "Electro-optics poled sol-gel materials doped with heterocycle push-pull chromophores", *Mater. Sci. Eng. C* 26 (2006) 979-982.
[159] J. Fick, B. Ménaert, J. Zaccaro & P. Moretti, "Hemisphere m-line spectroscopy an its application to birefringent $KTiOPO_4$ planar waveguides", *Opt. Commun.* 270 (2007) 229.
[160] P.K. Tien, R. Ulrich & R.J. Martin, "Modes of propagating light waves in thin deposited semiconductor films", *Appl. Phys. Lett.* 14 (1969) 291

[161] R. Ulrich, "Theory of the prism-film coupler by plane-wave analysis", *J. Opt. Soc. Am.* 60 (1970) 1337.

[162] R. Mechiakh, F. Meriche, R. Kremer, R. Bensaha, B.Boudine & A. Boudrioua, "TiO_2 thin films prepared by sol-gel method for the waveguiding applications: Correlation between the structural and optical properties", *Opt. Mat.* 30 (2007) 645.

[163] Y. Okamura, S. Yoshinaka & S. Yamamoto, "Measuring mode propagation losses of integrated optical waveguides: a simple method", *App. Opt.* 22 (1983) 3982-3984.

[164] T.A. Strasser & M.C. Gupta, "Optical loss measurement of low-loss thin-film waveguides by photographic analysis", *App. Opt.* 31 (1992) 2041-2046.

[165] A. Boudrioua & J.C. Loulergue, "New approach for loss measurements in optical planar waveguides", *Opt. Commun.* 137 (1997) 37.

[166] K. Sunder, M. Grofmeier, R. Staskunaite & H. Bracht, "Dynamics of network formers and modifiers in mixed cation silicate glasses", *Z. Physicalische Chemie-Int. J. Res. Phys. Chem & Chem. Phys*. 224 (2010) 1677-1705.

[167] E.L. Crepaldi, G.J.A.A. Soler-Illia, [a] Bouchara, D. Grosso, D. Durand & C. Sanchez, "Controlled formation of highly ordered cubic and hexagonal mesoporous nanocrystalline yttria-ceria and ceria-zirconia thin films exhibiting high thermal stability", *Angew. Chem. Int.* 42, 3 (2003) 347.

[168] M.T. Ruiz, G.F. De La Fuente, A. Badía, J. Blasco, M. Castro, A. Sotelo, A. Larrea, F. Lera, C. Rilo & R. Navarro, "Solution-based synthesis routes to $(Bi_{1-x}Pb_x)_2Sr_2Ca_2Cu_3O_{10+\delta}$", *J. Mat. Res*. 8 (1993) 1268-1276.

[169] A. Sotelo, G.F. De La Fuente, F. Lera, D. Beltrán, F. Sapiña, R. Ibáñez, A. Beltrán & M.R. Bermejo, "Novel polymer solution synthesis of the 110K superconducting phase in the bysmuth system", *Chem. Mater.* 5 (1993) 851-856.

[170] W. Liu, Y. Chen, C. Ye & P. Zhang, "Preparation and characterization of doped sol-gel zirconia films", *Ceramics International* 28, 4 (2002) 349.

[171] Y.L. Soo, P.J. Chen, S.H. Huang, T.J. Shiu, T.Y. Tsai, Y.H. Chow, Y.C. Lin, S.C. Weng, S.L. Chang, G. Wang, C.L. Cheung, R.F. Sabirianov, W.N. Mei, F. Namavar, H. Haider, K.L. Garvin, J.F. Lee, H.Y. Lee & P.P. Chu, "Local structures surrounding Zr in nanostructurally stabilized cubic zirconia: Structural origin of phase stability", *J. Appl. Phys.* 104 (2008) 113535.

[172] G.A. Turko, A.S. Ivanova, L.M. Plyasova, G.S. Litvak & V.A. Rogov, "Synthesis and Characterization of Fluorite-like Ce-Zr-Y-La-O systems", *Kinetics and Catalysis* 46 (2005) 884-890.

[173] L.N. Bihn, R.P. Netterfield and P.J. Martin, "Low-loss waveguiding in ion-assisted-deposited thin films", *Appl. Surf. Sci.* 22-23, 2 (1985) 656-662.

[174] S. Baccaro, Monika, G. Sharma, K.S. Thind, Devinder Isngh & A. Cecilia, "Analysis of structural modifications in γ-irradiated $PbO\text{-}B_2O_3\text{-}SiO_2$ glasses by FTIR spectroscopy", *Nucl. Instr. And Meth. A* 260 (2007) 613-618.

[175] L.H. Germer and A.H. White, "Electron diffraction studies of thin films: II Anomalous powder patterns produced by small crystals", *Phys. Rev.* 60 (1941) 447-455.

[176] V.F. Degtyareva, O. Degtyareva, M.K. Sakharov, N.I. Novokhatskaya, P. Dera, H.K. Mao and R.J. Hemley, "Stability of Hume-Rothery phases in Cu-Zn alloys at pressures up to 50 GPa", *J. Phys. Condens. Mater.* 17 (2005) 7955-7962.

[177] S.S. Harilal, C.V. Bindhu, M.S. Tillack, F. Najmabadi & A.C. Gaeris, “Internal structure and expansion dynamics of laser ablation plumes into ambient gases”, *J. Appl. Phys.* 93 (2003) 2380-2388.
[178] R. Kibar, A. Cetin, N. Can, "Effect of thermal treatment on linear optical properties of Cu nanoclusters", *Physica B* 404 (2009) 105-110.
[179] P.V. Kazakevich, A.V. Simakin, V.V. Voronov and G.A. Shafeev, “Laser induced synthesis of nanoparticles in liquids”, *Appl. Surf. Sci.* 252 (2006) 4373-4380.
[180] H. Amekura, O.A. Plaksin, N. Kishimoto and Ch. Buchal, “Annealing atmosphere effects on Zn nanoparticles in SiO_2 and transformation onto ZnO nanoparticles”, *Surf. Coat. Technol.* 201 (2007) 8215-8219.
[181] T. Karali, N. Can, L. Valberg, A.L. Stepanov, P.D. Townsend, Ch. Buchal, R.A. Ganeev, A.I. Ryasnyansky, H.G. Belik, M.L. Jessett and C. Ong, “Optical properties and luminiscence of metallic nanoclusters in ZnO:Cu”, *Physica B* 363 (2005) 88-95.

ACKNOWLEDGEMENTS

Como empezar? Como acabar? Quizáis houbo un principio e un final, máis foi, é e será unha etapa, unha gran etapa da miña vida.

Quizáis, máis que unha tese científica, a consecución duns resultados do seu entendemento e de … -maloserá que algo non aprendera, bastante aprendín, pero máis que queda por aprender-, esta tese, este traballo, esta etapa, supuxo un vehículo excepcional para formarme como persoa!!! Aínda que moitas veces só fronte ós elementos (ten que haber certa épica en toda historia para facela interesante); todo isto que acadei foi posible grazas a unha recua importante de xente que estivo ahí, que está eiquí e que estará onde vaia ou me encontre; que é o máis especial que pode ter unha persoa, xente que te motive a seguir de pé, a non vivir asoballado.

Toda historia ten un principio, podería empezar rememorando unha noite de sábado dun lonxano dezasete de avril do 1982, mais, a xente que consideras importante está ahí tódolos días do amencer ó solpor, e incluso de noite aínda que chegues tarde; porque a xente importante coma as cousas importantes, non necesitan dunha gran enciclopedia para ser valoradas; por iso as primeiras grazas, por estar ahí, por reñer e querer, por falar e calar, por moito e por pouco, por todo: Margha e Paco, meus pais; sobran as palabras, xa chegan os feitos. Pero, quizáis nun nivel un 'cachiño' superior está os meus avós, Estrella e Perfecto, os grandes faros da miña vida, os meus grandes exemplos, coas volta e reviravoltas da súa vida, as súas ensinanzas, sinxelas pero máis grandes e valoradas que Castelao, Einstein, Pasteur, Che Guevara e tantos outros; con traballo e con corazón, do máis sinxela sae o máis grande. A miña 'irmansiña' Estela, por acompañarnos mutuamente polo Skype, que tamén ocupou un oco grande. A Familia; o meu Edén, o meu Totem, dos primeiros e do resto tomei todos os retales que puiden para ser un todo do que se sentan orgullosos; porque todos me ensinaron, e ensinan algo tódolos días!!! A/-os pequena/-os, primas/-os, tías/-os e demáis que estades ahí!! e dos que xa non están físicamente pero sí na miña ialma …. moitas grazas a todos por ser vós!!!

Non son familia no papel pero sí no corazón que é o que vale; por ser unha vía de escape, de risas, de experiencias, de moito e máis ….. Marcos e Rosana.

Máis esta historia en concreto tivo un comezo máis cercano, ou agora xa bastante lonxano, pero, ante todo, fundamental para chegar eiquí; debo agradecer moi especialmente e porque xa son parte da miña propia familia: Xermán e familia; por apostar por min e estar ahí, e apoiarme, e guiarme, e tantas cousas, por ser ti -Abríchesme unha maravillosa porta!!! Mais moi especial é tamén o cariño á chave que permitiu abrir esa porta: Alberto Marta, grazas a ti pola aportación de lóxica, de sabedoría, de saber estar e de cordura con doses necesarias de non-cordura. Recordos as 'túas mulleres'.

E como todas as portas necesitan un marco no que asentar; ese marco nesta etapa debo agradecerllo a Carlos, a Mariví, a Maite e a Carmen, por poder formarme científicamente con eles. E … cómo non!!?? a Dani (con maiúsculas!!!), a Antonio, a Ana, Mar, Justo, e á xente da Escola de Óptica polas horas de 'traballo' compartido. Tamén un especial agradecemento ó persoal de Microscopía Electrónica e Confocal do CACTUS; a Ramiro, Raquel e Merche por prestarme gran parte do seu tempo.

Mais para formarse como persoa non basta co que tes preto, tamén hai que saír e interaccionar con outras culturas, outras formas de ver a vida, de pensar, de traballar, ….

Moitas gracias á xente do ICMA, sobre todo a Ruth; pero sin olvidarme de Vassilly, Raquel, Carlos Estepa, Carlos Díez, Isabel, Luis Alberto, Edgar e Clarisa – e respectivas/-os. Por ser tan maños e acollerme en Zaragoza.

Tamén debo agradecer á xente do ICV que me acolliu, o grupo de Alicia Durán; pero sobre todo a Jose Manuel (pisha!!!), a Juan Vargas (toda unha institución), Corina, Eva Peiteado, Fran Muñóz, Glenn e Chus polas horas de traballo e minutos de comida!!.

Für Prof. Mader: Mit meine Herz, Vielen Danke für deine Hilfe. Und auch danke Willie (für ihre vielen Stunden mit die mikroskop), Sonjia (für deine hilfe), Gisela (meine deustchland grossmutter), Karl-Heinze (die gross Technische), Dagmar, Florian, Simon, Isabelle, Sven Martin, Michael, Dominic, Wentao, Tobias, Thomas, Christine, Sebastian, Thomas, Gunnar, Heike und Sabrina. Und … a xente da Casa de Galiza de Bonn, que me acolleron como a tantos outros, como se fose da súa familia; xente con maiúsculas, coa que

compartín o grande sentimento dos galegos, a morriña; Eva, Manu, Ascen, Rebeca, Jasmine, Juan, María, Cris e moitos máis emigrantes, todo o meu cariño e moitos aloumiños!!!

També vull agrair al Prof. Juan Carda i la gent de la Universitat Jaume I, sobretot a Jose Miguel i Juan pel magnífic tracte rebut en tan pocs dies a Castelló. Moltes gracies amics!!!

Tutto il mio cuore a la gente del IFAC, en espeziale a Gualtiero (e a Matilde!!). Grazie mile al Prof. Righini, Silvia (moltes gracies noia!!!), Stefano, Franco, Massimo, Andrea, Daniele, Roberto Calzolai, Piere-Henri (merçi!!), Pogessi ('Keith Richards'), .. e tanti altro per due mesi intensi come una vita. Ma grazie mile con tutto il mio cuore a …. Simone!!! (tu sei grandissimo caro amici!!!).

E a toda a xente que fun coñecendo estes anos, de idas, voltas e reviravoltas; que me aportaron o seu gran de area a ser quen son agora: a 'nonna' Fernanda, a Laura Miranda (algún día faremos os tres unha boa viaxe, Raquel!!!), a Costa-Kramer, a Luiz, a Paloma (graçies xiqueta!), …. pero tamén, e sobretodo, os que están aquí perto: Olalla e Vanesa (por estar ahí dende a carreira -anos, vivencias, comidas, ceas, jolgorrios ….- que non acaben raparigas!!!) ou Eloy Val (qué? animamos o partido cunha patadiña?).

E as penúltimas pero non menos importantes gracias a todos os amigos que tamén puxeron gráns, e moitos; Michel, Chicho, Marquiños, Toñito, Chus, … Caión!!! meu lar!!!

Podería seguir, pero como aprendín nestes anos, a túa xente, a que de verdade che importa e lle importas, non necesita de monumentos ou reverencias, sinxelamente só aparece cando a necesitas e cando te necesita!!!

MOITAS JRACIAS a todos!!! (Outro gran éxito da Peña Royal- Manel dixit).

PD: bueno … e .. se nos deixamos de parrafadas e tomamos algho?? ou senón, Montse!, David!, se queredes levo a Daniela ó parque con Sofía!!!).

RELATION
of COMMUNICATIONS

Articles

- F. Rey-García, C. Gómez-Reino, M.T. Flores-Arias, A. Durán, Y. Castro and G.F. De La Fuente, "Sol-gel coatings: an alternative route for producing planar optical waveguides", Thin Solid Films 519, 22 (2011) 7982-7986 Doi: 10.1016/j.tsf.2011.05.054.

- F. Rey-García, C. Gómez-Reino, M. T. Flores-Arias, G. F. De La Fuente Leis, W. Mader and W. Assenmacher, "Structural and optical characterisation of planar waveguides obtained via Sol-Gel", Proc. SPIE 8001, 800116 (2011); Doi:10.1117/12.891941.

- F. Rey-García, M.T. Flores-Arias, C. Gómez-Reino, G.F. De La Fuente, W. Assenmacher and W. Mader, "TEM characterization of planar step-index waveguides obtained via Sol-Gel", *Chem. Mater., submitted.*

- F. Rey-García, C. Gómez-Reino, M.T. Flores-Arias, G.F. De La Fuente, W. Assenmacher and W. Mader, "Fabrication and TEM characterization of metal waveguides obtained via laser backwriting", *Thin Solid Films, submitted.*

- F. Rey-García, M.T. Flores-Arias, C. Gómez-Reino, V.V. Lennikov, L.C. Estepa, G.F. De La Fuente, W. Assenmacher and W. Mader, "Laser Zone Melting and microstructure of waveguide coatings obtained on soda-lime glass", *Solid State Sci., submitted.*

- F. Rey-García, C. Gómez-Reino, M.T. Flores-Arias, G.F. De La Fuente, S. Berneschi, S. Pelli, G. Nunzi-Conti and G.C. Righini, "Structural and optical characterization of ZrO_2:CeO_2 slab waveguides obtained via Sol-Gel", *J. Mater. Chem., submitted.*

Congress Communications

- NEMO's Second General Scientific Networking Meeting; "Fabrication of planar waveguides via coating of planar glass substrates with ceramic frits"; F. Rey-García, D. Nieto, C. Gómez-Reino, M.T. Flores-Arias, A. Castelo, M.V. Pérez, C. Bao, V. Lennikov & G.F. De la Fuente. (Firenze, Italia; May 17-18, 2007). Poster.

- Optoel 2007; “Fabricación de guías mediante el recubrimiento de sustratos de vidrio planos con fritas cerámicas”; F. Rey-García, D. Nieto, C. Gómez-Reino, M.T. Flores-Arias, M.V. Pérez, V. Lennikov & G.F. De la Fuente. (Bilbao; July 11-13, 2007). Poster.

- European Conference on Solid State Chemistry XI; “Preparation of planar waveguides on planar substrates”; F. Rey-García, D. Nieto, C. Gómez-Reino, M.T. Flores-Arias, M.V. Pérez, V. Lennikov & G.F. De la Fuente. (Caen, France; September 11-13 , 2007). Poster.

- XLVII Congreso Anual de la Sociedad Española de Cerámica y Vidrio; “Fabricación de guías de onda en substratos de vidrio planos” F. Rey-García, D. Nieto, C. Gómez-Reino, M.T. Flores-Arias, M.V. Pérez, C. Bao, V.V. Lennikov & G.F. De la Fuente. (Toledo, Spain; October 24-26, 2007). Oral presentation.

- V Congreso Franco-Español de Química y Física del Estado Sólido; “Fabrication and characterisation of glassing engraved waveguides” F. Rey-García, C. Gómez-Reino, M.T. Flores-Arias, D. Nieto & G.F. de la Fuente (Clermont-Ferrand, France; April 2-4 de Abril, 2008). Oral presentation.

- XLVIII Congreso Anual de la Sociedad Española de Cerámica y Vidrio; “Fabricación de guías de onda en substratos de vidrio planos mediante tecnología Sol-Gel” F. Rey-García, D. Nieto, C. Gómez-Reino, M.T. Flores-Arias, G.F. De la Fuente, A. Durán & Y. Castro. (Oviedo, Spain; October 29-31, 2008). Oral presentation.

- IX Reunión Nacional de Óptica; “Fabricación de guías de onda mediante tecnología sol-gel sobre substratos de vidrio planos”; F. Rey-García, D. Nieto, M.T. Flores-Arias, C. Gómez-Reino, A. Durán, Y. Castro & G.F. De la Fuente. (Ourense; September 14-17, de 2009). Oral presentation.

- European Conference on Solid State Chemistry XII; “Interfaces in planar waveguides obtained via Sol-Gel”; F. Rey-García, C. Gómez-Reino, M.T. Flores-Arias, G.F. De la Fuente, W. Assenmacher & W. Mader. (Münster, Deutschland; September 20-23, 2009). Poster.

- XLIX Congreso Anual de la Sociedad Española de Cerámica y Vidrio; “Fabricación de recubrimientos de substratos de vidrio plano mediante láser de CO_2”; F. Rey-García, D. Nieto, C. Gómez-Reino, M.T. Flores-Arias, G.F. De la Fuente, W. Assenmacher & W. Mader. (Linares, Spain; October 28-30, 2009). Poster.

- 4th Intensive School on Conservation Science; "Laser marking techniques applicable to Cultural Heritage materials identification"; F. Rey-García, M.T. Flores-Arias, C. Gómez-Reino, R. Lahoz & G.F. De La Fuente. (Teruel, Spain; July 19-31, 2010). Poster.

- AOP'2011 International Conference on Applications of Optics and Photonics; "Structural and optical characterisation of planar waveguides obtained via Sol-Gel"; F. Rey-García, C. Gómez-Reino, M.T. Flores-Arias, G.F. De La Fuente, W. Assenmacher & W. Mader. (Braga, Portugal; May 3-7, 2011). Oral presentation. ***Student's Award: Third Place Student Paper granted by SPIE (International Society for Optics and Optoelectronics).***

- 22nd General Congress of the International Comission for Optics (ICO-22); "Characterization of planar waveguides fabricated by multiple Sol-Gel dip-coatings"; F. Rey-García, M.T. Flores-Arias, C. Gómez-Reino, G.F. De La Fuente, S. Berneschi, S. Pelli, G. Nunzi-Conti & G.C. Righini. (Puebla, Mexico; August 15-19, 2011). Poster.

- FeAl 2011; "Laser Surface Treatment of Fe/Al alloys"; F. Rey-García, C. Bao, C. Gómez-Reino, R. Lahoz, G.F. De La Fuente, H. Santos-Barahona & F.J. Pérez-Trujillo (Lanzarote, Spain; October 5-7, 2011).

- China International Conference on High-Performance Ceramics; "Laser processing of Ceramics"; R. Lahoz, I. De Francisco, L.A. Angurel, L.C. Estepa, F. Rey-García, M.T. Flores-Arias, C. Bao, C. Gómez-Reino & G.F. De La Fuente (author). (Xiamen, Fujian Province, China; November 4-7, 2011). Invited conference.

- IV Congresso Luso-Espanhol de Cerâmica e Vidro; "Microstructure of soda-lime glass modified by Laser Ablation Backwriting"; F. Rey-García, C. Gómez-Reino, M.T. Flores-Arias, R. Lahoz, L.A. Angurel, G.F. De La Fuente, W. Assenmacher, W. Mader & J.B. Carda. (Aveiro, Portugal; November 16-18, 2011). Oral presentation.

RELATION
of Pre-DOCTORAL STAYS

Pre-Doctoral Stays:

1.- Center: Instituto de Cerámica y Vidrio de Madrid, Consejo Superior de Investigaciones Científicas (ICV-CSIC)
Place: Madrid (Spain) Duration: 2 months & 3 weeks;
from 25-02-08 to 14-05-08.

2.- Center: Instituto de Ciencia de Materiales de Aragón, Universidad de Zaragoza, Consejo Superior de Investigaciones Científicas (ICMA-CSIC)
Place: Zaragoza (Spain) Duration: 1 month;
from 19-11-08 to 19-12-08.

3.- Center: Institüt fur Anorganische Chemie, Universität Bonn
Place: Bonn (Deutschland) Duration: 6 months;
from 02-02-09 to 31-07-09.

4.- Center: Institüt fur Anorganische Chemie, Universität Bonn
Place: Bonn (Deutschland) Duration: 4 months;
from 01-02-10 to 27-05-10.

5.- Center: Istituto di Fisica Applicata "Nello Carrara", Consiglio Nazionale delle Ricerche (IFAC-CNR)
Place: Sesto Fiorentino (FI, Italy)
Duration: 2 months;
from 01-02-11 to 01-03-11.

Resume

(galego)

Resume (galego)

A tese ten como finalidade a fabricación e caracterización de estructuras fotónicas para a s súas potenciais aplicacións en campos relacionados coa óptica espacial, en particular, como guías de onda planares. A motivación do traballo foi o estudio de métodos pouco explorados e o emprego de subtratos baratos que permitan a fabricación de guías de onda a escala industrial. Estos dispositivos son de gran interés para un gran número de aplicacións en comunicacións, óptica integrada e noutros campos tecnolóxicos. Durante os últimos anos, moitos autores exploraron diversos métodos de fabricación co fin de obter estructuras fotónicas, nembargantes, en moitos casos, os productos obtidos (en especial co uso de substratos non comerciais), ou os equipos empregados resultaron excesivamente caros (o cal faría inviable a súa aplicación a escala industrial). O recubrimento de materiais para potenciar ou modificar as súas propiedades implica un amplo campo de estudo, desenrolado durante décadas. En particular, a preparación de guías de onda planares provocou sempre un gran interés por parte dos investigadores debido as súas potenciais aplicacións en fotónica. Tradicionalmente, este tipo de dispositivos foron fabricados empregando métodos tales como intercambio iónico, deposición química de vapor (CVD), e deposición física de vapor (PVD). Máis recentemente empregáronse métodos de fabricación de dispositivos ópticos integrados basados en implantación iónica, litografía ou fotolitografía, escritura láser directa ou, incluso, irradiación láser mediante pulsos ultra-cortos. Estas implican o emprego de equipamento complexo (sistemas de baleiro ou láseres caros son necesarios) ou condicións de síntese e reactivos especiais que resultan nun incremento elevado dos costes de fabricación. Todos estes métodos están basados no control do cambio de índice de refracción local dun substrato transparente. En todolos casos mencionados anteriormente, o substrato está dopado e o cambio xerado no índice de refracción dentro do substrato é consecuencia do dopado que fai capaz o guiado de luz ó seu través.

A complexidade inherente asociada aos métodos anteriormente mencionados, promoveu a búsqueda de métodos de fabricación máis baratos e sinxelos como alternativa aos tradicionais. Recubrimentos física e químicamente compatibles foron desenrolados modificando substratos de vidro comercial. Seguindo estes principios, desenroláronse unha serie de métodos ou tecnoloxías descritas celadamente nesta tese. Deste xeito, os métodos e substratos empregados nesta tese amosan alta repetibilidade, precisión, control e materiais baratos.

Primeiramente débese describir en que consiste unha guía de onda. Unha guía de onda planar permite o guiado de luz a través do seu volume sin cambios significativos das súas propiedades. Deste xeito, abren a porta a moitas aplicacións tecnolóxicas que inclúen as comunicacións, sensores, láseres e equipos ópticos, entre outros. Además, un gran número de dispositivos basados en interconnexións ópticas poderían ser desenrolados co fin de implementalos en sistemas de distribución en paralelo ou de cruce de sinais ópticos. A posibilidade de fabricación de guías de onda planares empregando tecnoloxías baratas e sinxelas abre a porta a un campo da ciencia moi interesante.

Tres técnicas diferentes para a fabricación de guías de onda planares son estudiadas neste traballo. O método Sol-Gel e dous métodos de Irradiación Láser (a Fusión Zonal, LZM, e a Ablación Inversa de placas metálicas, LAB) foron desenrolados; as correspondentes mostras obtidas son caracterizadas a través de diferentes técnicas. Cada método supón a obtención dunha mostra cunhas determinadas características; por iste motivo, dependendo do tipo de mostra, empregouse un amplo abanico de técnicas de caracterización. A caracterización do método de ablación láser consiste básicamente no estudo dos procesos responsables da formación das guías de onda. Os métodos de fabricación e as técnicas de caracterización descríbense nos Capítulos 1 e 2; os resultados obtidos disértanse no Capítulo 3.

A análise química e microstructural levouse a cabo mediante Microscopía Electrónica de Transmisión (TEM), Microscopía Electrónica de Barrido (SEM), Microscopía Confocal, Espectroscopía UV/Vis, Difracción de Raios-X (XRD) i Espectroscopía IR/Raman. A caracterización óptica das mostras desenvolveuse

empregando diferentes técnicas de medida do índice de refracción, do espesor e das perdas de guiado. Empregáronse distintas técnicas tales como a Técnica do Campo Cercano Refractado (RNF), Ellipsometría, Espectroscopía da Línea D Escura e distintos métodos de medida das perdas basadas en diferentes tipos de acoplamento entre a luz e a mostra. Ademáis, tamén se mediu a conductividade eléctrica das mostras metálicas obtidas mediante ablación láser. Todas estas técnicas de caracterización están descritas no Capítulo 2.

O método Sol-Gel está basado na obtención de capas delgadas (dende 135 nm a 2,15 μm, medidos por Elipsometría) partindo dunha solución de alcóxidos metálicos como precursores. A síntese Sol-Gel consiste, maioritariamente, na hidrólise e polimerización dos precursores orgánicos e inorgánicos, co fin de obter redes espaciais covalentemente unidas. Unha vez rematado o proceso sintético, a solución obtida (sol) e depositase mediante a técnica de "dip-coating" en substratos de vidro comercial. A adhesión dos materiais conséguese tralo procesado térmico dos mesmos. Este método permite un elevado control da composición, espesor e índice de refracción das capas obtidas. Desenroláronse e testaron diferentes sistemas basados en mesturas de SiO_2, TiO_2, ZrO_2 e CeO_2; obtendo un rango de índices de refracción dende 1.45 a 2.04 (valores obtidos por Elipsometría). Esta clase de mostras amosan perdas moderadas de guiado; obténdose valores sitos entre 0.85 a 1.5 dB/cm para o coeficiente de atenuación para mostras de SiO_2:TiO_2 e ZrO_2:CeO_2.

A Fusión Zonal mediante Láser (LZM) aplicouse a mesturas de óxidos inorgánicos depositados sobor substratos de vidro comercial, obtendo capas guía con espesores mínimos de 10 μm. Realizáronse mesturas de pós óxidos inorgánicos e suspendidas en solucións alcoholicas que se depositaron sobor substratos de vidro comercial mediante unha técnica de serigrafía denominada "Dr. Blade". O proceso de sinterizado levouse a cabo mediante o emprego dun láser de CO_2 de 100W de potencia (Easy Mark100, Easy Laser) acoplado a un forno provisto dun tren de rolos (Nanetti); tamén se realizou o tratamento térmico dunha serie de mostras nun forno convencional, co fin de comparar os resultados dos procesos e dilucidar as ventaxas proporcionadas polo método LZM respecto ó método de fusión tradicional. Os recubrimentos obtidos están basados en borosilicatos de chumbo. A composición básica destes borosilicatos

de chumbo amosa un índice de refracción de 1.58 (obtido a través da Técnica do Campo Cercano Refractado, λ=633 nm). As perdas medidas resultaron máis altas que as obtidas polo método Sol-Gel, resultando nun valor de perdas de 3.04 dB/cm para as mostras de porosilicato de chumbo dopadas con yterbio. O emprego desta tecnoloxía supón un método novedoso para a fabricación de guías de onda planares.

O estudo das mostras obtidas mediante ablación láser inversa de placas metálicas (LAB) supón a continuación do traballo desenrolado previamente por outros investigadores do grupo. O obxectivo da presente tese é o estudo dos procesos inmersos na formación de canais guía metálicos sobor substratos de vidro comercial mediante escritura láser inversa. Mostras de aluminio (Al), prata (Ag) e latón comercial (63Cu37Zn) foron obtidas e caracterizadas. Este método consiste na ablación dun branco metálico co fin de provocar trocos no índice de refracción do substrato de vidro situado encima da placa metálica. Neste proceso, prodúcese o paso de partículas metálicas, que son arrincadas formando unha pluma de ablación, dende a lámina metálica ao substrato, provocando un troco no índice de refracción da zona irradiada. Para a realización deste método empregouse un láser Powerline E (Rofin) de Nd:YVO4 de 20W de potencia bombeado por diodos e que produce pulsos de nanosegundos á lonxitude de onda fundamental (1064 nm). Os resultados finais permiten observar como esta clase de materiais fotónicos se comportan como elementos difusivos, cando nos referimos a guiado de luz.

A etapa final deste traballo supón a comparación dos resultados e a exposición das conclusións deducción dos mesmos (Capítulo 4).

A relación das conclusións derivadas do traballo presentado están agrupadas segundo o tipo de método empregado na fabricación de guías de onda planares sobor substratos de vidro comercial e enuméranse a continuación:

Método Sol-Gel:

Mediante o método Sol-Gel fabricáronse guías de onda planares, aplicando a técnica de deposición denominada dip-coating, sobor substratos de vidro comercial. En particular:

– Guías de onda de diferentes composicións, tales como $SiiO_2$:TiO_2, SiO_2:CeO_2, SiO_2:ZrO_2 e ZrO_2:CeO_2 foron obtidas seguindo o proceso Sol-Gel. Ademáis, resultou un éxito a obtención de guías dopadas con erbio (Er); incorporado como dopante nos soles en forma de Ce(NO3)3·5H2O.

– A aplicación do método Sol-Gel para a fabricación de guías de onda de salto de índice permitiu a obtención dun amplo rango de recubrimentos cunha gran variedade de índices de refracción (entre 1.47 e 2.07; medidos mediante Espectroscopía da Línea D Escura) e espesores (dende 100 nm a decenas de micrómetros). A obtención destas parámetro obtense gracias ó axuste dos parámetros de síntese (selección axeitada de precursores, control de tempo de reacción, grado de hidrólise, pH, concentración do sol, temperatura de sinterizado, …) aos requerimentos desexados para as capas finais.

– Os recubrimentos obtidos exhiben interfases ben definidas e son homoxéneos e continuos ó longo da extensión superficial do substrato tratado.

– Grazas ó apilamento sucesivo de capas delgadas (ata 6) de Sol-Gel foi posible a obtención de capas grosas (ata 1.2 μm). Non se observaron roturas nin defectos macroscópicos entre as sucesivas capas das estructuras multicapa Sol-Gel depositadas sobor substratos de vidro comercial. Este feito permite o desenrolo de guías de onda de salto de índice para moitas aplicacións previstas, tanto no campo das comunicacións como dos dispositivos optoeléctronicos.

– A combinación de capas con diferente composición, e, consecuentemente, de distinto índice de refracción, foi demostrada empregando os soles SiTi e ZrCe.

– O acoplamento entre os substratos de vidro comercial e as capas Sol-Gel está dominado por un proceso químico difusivo. Os ións alcalinos e os ións alcalino-térreos migran dende o substrato ó recubrimento, namentres que ao mesmo tempo, na area do substrato adxacente ó recubrimento créase unha zona rica en Si.

– O método Sol-Gel proporciona mostras con baixa rugosidade superficial (<20 nm), facendo posible un potencial decrecemento das perdas de propagación mediante a reducción da dispersión de luz na superficie do recubrimento.

– Non se observaron fases cristalinas dentro dos recubrimentos obtidos por este método. Nembargantes, o método Sol-Gel tamén permite a introducción de nanopartículas que poderían inducir múltiples fenómenos fundamentais para a fabricación de elementos guiantes ou sensores.

– As perdas de guiado de luz avaliáronse empregando un método dasado na dispersión da luz. No caso das guías de onda de ZrCe 70:30 e as multicapas SiTi 70:30, determináronse, respectivamente, perdas aproximadas de 0.9 dB/cm e 1.3 dB/cm.

– As guías de onda de ZrCe amosaron un comportamento birefrinxente como consecuencia da presencia de cristais tetragonais de ZrO_2, como foi determinado mediante difracción de raios-X

Fusión Zonal mediante Láser (LZM)

Guías de onda planas sobor substratos de vidro comercial foron obtidas mediante a fusión por zonas (LZM) dun recubrimento de fritas co emprego dun láser de CO_2. Os resultados mais relevantes obtidos mediante este novedoso método enuméranse a continuación:

– Guías de onda planares basadas en mesturas de polvos comerciais de SiO_2, B_2O_3 e PbO, foron obtidas a través da súa fusión sobor substratos de vidro comercial.

– A diferencia no valor do índice de refracción atopadas entre o recubrimento LZM (1.58) e o substrato de vidro comercial (1.52) é suficiente para acadalo confinamento da luz e o subsecuente efecto de guiado a través do recubrimento.

– O método LZM permite a obtención de capas con espesores dende 10 μm ata 30 μm, os cales son moi útiles para a preparación de guías de onda multimodais. En contraste, os recubrimentos obtidos mediante fusión tradicional de fritas, esto é, en forno, amosan espesores superiores ós 30 μm.

– O método LZM permite a obtención de interfases menos difusas respecto ás mostras tratadas mediante fusión convencional.

– A interfase recubrimento-substrato está ampliamente influenciada pr procesos interdifusivos, onde ións alcalinos e ións alcalino-térreos migran dende o substrato ó recubrimento. Ao mesmo tempo, ións de chumbo (Pb) difúndense dentro do substrato. O acoplamento químico entre recubrimento e substrato ten lugar a nivel atómico, como se deduxo das observacións realizadas mediante microscopía electrónica de transmisión (TEM).

– O método LZM produce mostras cunha considerable rugosidade superficial, cercana ós 230 nm, o cal podería afectar negativamente ó guiado de luz. Nembargantes, como o espesor obtido é tan elevado, estas mostras poderían ser pulidas superficialmente reducindo, polo tanto, as perdas asociadas á rugosidade.

– As perdas de guiado das mostras obtidas mediante fusión zonal (LZM) son lixeiramente superiores ás obtidas a través do metodo Sol-Gel. Medíronse perdas de 4.15 dB/cm para unha mostra de borosilicato de chumbo preparada por LZM. Nembargantes, atopouse que o emprego de dopantes tales como yterbio (Yb) e bismuto (Bi) podería promover o decrecemento das perdas ata 3.04 dB/cm (caso das mostras de borosilicato de chumbo dopadas con Yb).

– O emprego do láser de CO_2 permite a fabricación de guías de onda planares sobor substratos de vidro comercial nunha soa etapa. Nembargantes, para moitas aplicacións, a presenza de zonas translucidas remanentes na superficie das mostras en areas non escaneadas pode supoñer unha seria desvantaxa.

– Outra posibilidade na obtención de guías de onda, facendo emprego de fritas cerámicas, esta basada na gravación de canais no substrato de vidro comercial. Estes canais obtivéronse mediante tratamentos mecánicos e de ablación láser. Os canais obtidos mediante a alción láser exhiben un acabado superfical máis fino e homoxéneo e una xeometría máis definida respecto ós canais obtidos mediante tratamentos mecánicos.

Ablación Láser Inversa de placas metálicas (LAB)

Fabricáronse recubrimentos metálicos sobor substratos de vidro comercial mediante a ablación laser inversa de placas metálicas (LAB). Empregáronse láminas metálicas de aluminio (Al), prata (Ag) e latón comercial (63Cu37Zn). O estudo deste método estivo centrado na identificación dos parámetros do proceso que inflúen nas propiedades dos recubrimentos obtidos via ablación inversa, tanto en aire como ao baleiro. As conclusións deducidas enuméranse a continuación:

– Recubrimentos preparados con Al, Ag e 63Cu37Zn foron obtidos sobor substratos de vidro comercial mediante a ablación laser inversa de placas metálicas (LAB).

– O método de ablación laser inversa de placas metálicas permite obter recubrimentos con espesor e xeometría variables, de acordo cos parámetros láser e de varrido do mesmo controlados mediante un software comercial. Ademáis, esta técnica permite a fabricación de guías de onda soterradas (“burried waveguides”) directamente, sen necesidade de procesos secundarios ou varias etapas.

– O proceso de formación dos recubrimentos mediante ablación laser inversa de placas metálicas segue un esquema diferente, dependendo da lámina metálica empregada. No caso do latón comercial (63Cu37Zn) e da Ag, as partículas ablacionadas son proxectadas e incrústanse no vidro comercial, onde permanecen en estado metálico ou elemental. Cando se emprega o Al, nembargantes, a intensa ablación das altamente reactivas especies de Al induce unha reacción química para a formación de aluminosilicatos en fase vítrea dentro da área afectada do substrato de vidro comercial.

– O proceso LAB pode ser levado a cabo encondicións atmosféricas normais ou baixo condicións de alto baleiro. No presente estudio empregáronse as dúas condicións atmosféricas. No caso do proceso realizado a alto baleiro, obsérvase unha alta direccionalidade da pluma de plasma orixinada pola ablación, coa consecuente influencia na modificación do substrato.

– Os valores de rugosidade superficial medidos varían considerablemente en función do metal e das condicións de proceso empregados. Os menores valores de rugosidade superficial obtivéronse para os recubrimentos de Ag, en torno a 47 nm. As mostras derivadas do proceso LAB realizado en placas de latón amosaron valores de rugosidade superficial en torno a 74 nm. En ambos casos, o proceso de ablación laser inversa de placas metálicas foi levado a cabo en aire. Os recubrimentos obtidos cos mesmos metais pero en condicións de alto baleiro exhibiron valores de rugosidade superficial de 269 nm e 123 nm respectivamente, para as mostras derivadas de Ag e 63Cu37Zn. No caso das mostras derivadas da ablación laser inversa de placas metálicas de Al, as guías soterradas obtidas permiten un pulido superficial das mostras sen afectar a zona dopada. Deste xeito, non foi necesario a medida do valor da rugosidade superficial para evaluar o seu grado de uniformidade.

– Cando consideramos os depositos adheridos a superficie do recubrimento, está claro que en condicións de alto baleiro, indúcese a formación de altas cantidades de detritos. Esta capa contaminante elimínase mediante un baño ácido antes das medidas ópticas que cumpra levar a cabo.

- Os estudios de Epsectroscopía UV/Vis indican que tanto as mostras derivadas de Ag como as mostras derivadas do latón exhiben bandas de resonancia plasmónicas (SPR), características da presenza de nanopartículas de Ag e Cu. Estas nanopartículas poderían ser responsables do incremento no índice de refracción do substrato de vidro comercial.

A conclusión principal relata a posibilidade de obter guías de onda planares mediante alternativas máis baratas e sinxelas que os métodos típicos presentes na literatura; os cales, xeralmente, requiren do emprego de reactivos e instrumental especial ou de condicións de baleiro. Ademáis, comprobouse con éxito a posibilidade de obter elementos guiantes sobor substratos de vidro comercial. Estes feitos supoñen unha vantaxe para a aplicación destes métodos a procesos de escala industrial.

Como anexos a este traballo de investigación inclúense unha serie de publicaións publicadas e difundidas tanto en xornais científicos como en congresos de índole nacional e internacional (Francia, Portugal, Italia, Alemaña, México e China). En ambas enumeracións obsérvase a importancia, amplitude e multidisciplinaridade do traballo de tese realizado; a divulgación dos resultados realizouse tanto en publicacións de marcado carácter óptico e/ou físico (*Proceedings of SPIE*) como en publicacións centradas noutros campos de ciencia tales como a química (*Chemistry of Materials* e *Solid State Sciences*), ou a ciencia de materiais (*Journal of Materials Chemistry* e *Thin Solis Films*).

Finalmente tamén cabe destacar a colaboración levada a cabo con distintos grupos e centros nacionais (ICMA-CSIC e ICV-CSIC) e internacionais (IAC-Bonn e IFAC-CNR) para o desenrolo tanto de métodos de fabricación das guías de onda como dos métodos de caracterización das mostras obtidas. Como froito destacado da transferencia de coñecementos acadouse unha mención especial (terceiro posto) no concurso de xovenes investigadores promovido por unha entidade internacional de óptica (International Society for Optics and Optoelectronics, SPIE) no congreso "AOP2011 International Conference on Applications of Optics and Photonics" (Braga, Portugal; Maio 2011).